Bernhard Ruff

Ultracold Gases in Strong Light Fields of Femtosecond Laser Pulses

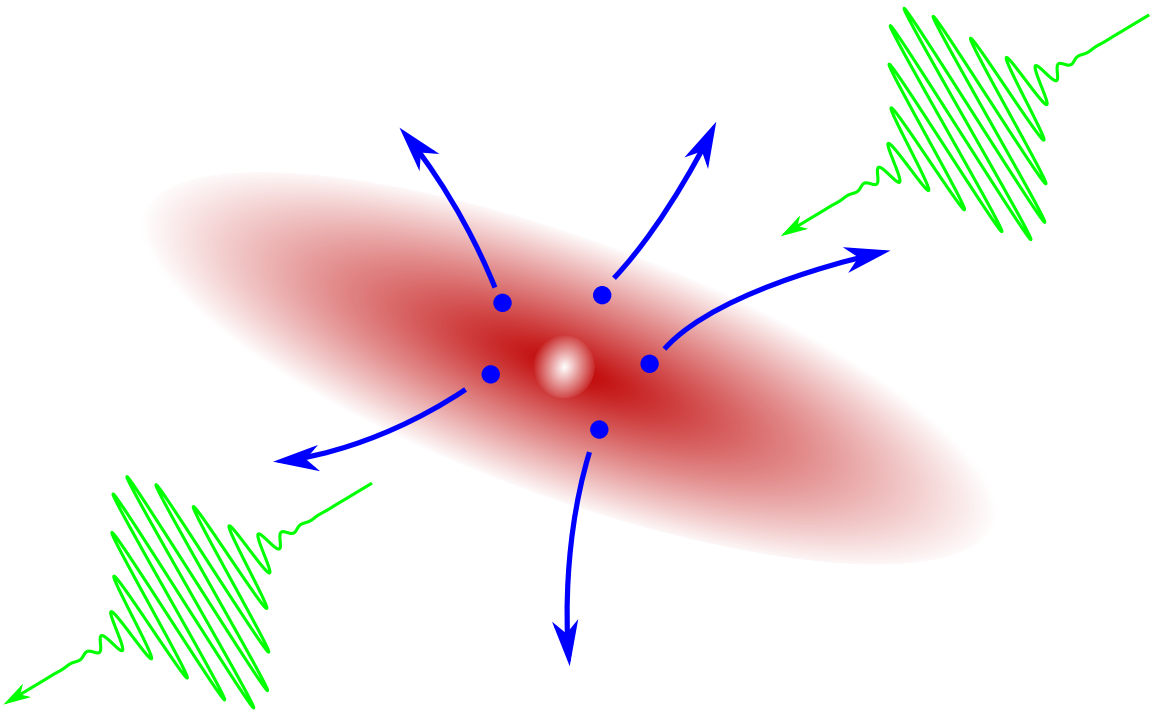

Dissertation zur Erlangung des Doktorgrades
an der Fakultät für Mathematik, Informatik und Naturwissenschaften
Fachbereich Physik der Universität Hamburg

Ultracold Gases in Strong Light Fields of Femtosecond Laser Pulses

---

Ultrakalte Gase in starken Lichtfeldern von Femtosekunden-Laserpulsen

vorgelegt von:

Bernhard Ruff

aus Tübingen

Hamburg, 2017

Fachbereich Physik

Univeristät Hamburg

CUI THE HAMBURG CENTRE FOR ULTRAFAST IMAGING

Gutachter der Dissertation:	Prof. Dr. Markus Drescher Prof. Dr. Klaus Sengstock
Zusammensetzung der Prüfungskommission:	Prof. Dr. Markus Drescher Prof. Dr. Henning Moritz Prof. Dr. Peter Schmelcher Prof. Dr. Roman Schnabel Prof. Dr. Klaus Sengstock
Vorsitzender der Prüfungskommission:	Prof. Dr. Peter Schmelcher
Datum der Disputation:	04.05.2017
Vorsitzender des Fach-Promotionsausschusses Physik:	Prof. Dr. Wolfgang Hansen
Leiter des Fachbereichs Physik:	Prof. Dr. Michael Potthoff
Dekan der Fakultät für Mathematik, Informatik und Naturwissenschaften:	Prof. Dr. Heinrich Graener

Abstract

Fundamental questions in quantum physics can be addressed by local ionization of quantum gases. In the strong field of ultrashort light pulses an ultracold atomic cloud can be ionized granting access to the physics of open quantum systems and hybrid atom-ion systems. Analyzing the ionization fragments allows investigating the transfer of coherence from a macroscopic quantum mechanical state to its microscopic constituents.

In this work ultracold ^{87}Rb atoms are locally ionized using femtosecond laser pulses of 220 fs pulse duration. The atom loss after a laser pulse is connected to the ionization probability which is quantified using absorption imaging. The experimental results are in good agreement with our theoretical model that combines two-photon and over-the-barrier ionization. In addition, the measurements suggest that the ions interact with the ultracold environment forming a hybrid system. The transient optical dipole force that femtosecond laser pulses exert on the atoms has been characterized.

Accessing the transfer of coherence from a Bose-Einstein condensate (BEC) to photoelectrons requires a new experimental setup: Electrons being created by femtosecond laser pulses in two distinct locations of the condensate are detected using position sensitive detectors with single particle sensitivity. Such an experiment is technically challenging as the requirements with respect to background pressure in the vacuum system, detection efficiency for charged particles and control of stray electric and magnetic fields are very strict. An ultrahigh vacuum system accommodating the ultracold atomic cloud as well as the detectors has been built. The atoms can be transfered from the newly built hybrid trap to the interaction region by means of optical transport that has been developed in the course of this work. In addition, the optics to create two adjacent and diffraction-limited foci is characterized. Ionization fragments are sensitive to stray magnetic fields, therefore, an active compensation system is has also been constructed.

Zusammenfassung

Fundamentale Fragestellungen der Quantenphysik können mittels lokaler Ionisation von Quantengasen adressiert werden. In starken Feldern ultrakurzer Lichtpulse werden ultrakalte, atomare Wolken ionisiert und ermöglichen so den Zugang zur Physik der offenen Quantensysteme und der hybriden Atom-Ion Systeme. Die Analyse der Ionisationsfragmente erlaubt die Untersuchung des Kohärenztransfers von einem makroskopischen, quantenmechanischen Zustand auf seine mikroskopischen Bestandteile.

In dieser Arbeit werden ultrakalte ^{87}Rb Atome mit Hilfe von Femtosekunden-Laserpulsen mit einer Pulsdauer von 220 Femtosekunden lokal ionisiert. Der Verlust von Atomen nach einem Laserpuls hängt eng mit der Ionisationswahrscheinlichkeit zusammen, die hier quantitativ mit Hilfe von Absorptionsabbildungen vermessen wurde. Die experimentellen Ergebnisse stimmen gut mit unserem theoretischen Model überein, das Zwei-Photonen- und ‚over-the-barrier'- Ionisation berücksichtigt. Zusätzlich, deuten die Messungen darauf hin, dass die Ionen mit ihrer ultrakalten Umgebung wechselwirken und ein Hybridsystem bilden. Die transiente optische Dipolkraft, die ein Femtosekunden-Laserpuls auf die Atome ausübt wurde ebenfalls charakterisiert.

Zugänglich wird der Kohärenztransfer von einem Bose-Einstein Kondensat (BEC) auf Photoelektronen durch einen neuen experimentellen Aufbau: Einzelne Elektronen, die von femtosekunden Laserpulsen an zwei getrennten Orten des Kondensats erzeugt werden, lassen sich mit hocheffizienten, ortsauflösenden Detektoren nachweisen. Ein solches Experiment birgt viele technische Herausforderungen, da die Anforderungen in Hinblick auf den Hintergrunddruck des Vakuumsystems, die Nachweiseffizienz für geladene Teilchen und die Kontrolle elektrischer sowie magnetischer Streufelder sehr hoch sind. Zunächst wurde ein Ultrahochvakuum-System aufgebaut, dass die ultrakalte atomare Wolke sowie die Detektoren beherbergt. Die Atome können durch einen optischen Transport, der im Rahmen dieser Arbeit entwickelt wurde, von der neu gebauten Hybridfalle zur Wechselwirkungszone bewegt werden. Zusätzlich wurde die Optik zur Erzeugung von zwei benachbarten und beugungsbegrenzten Fokussen charakterisiert. Da Ionisationsfragmente empfindlich auf magnetische Streufelder reagieren, wurde außerdem ein System zur aktiven Kompensation realisiert.

Contents

CHAPTER 1

Introduction

Modern physics has radically changed our perception of nature as quantum mechanics has established the fundamentally new concept of wave-particle dualism. The wave character of massive particles has been first demonstrated in electron scattering experiments [1]. Quantum theory also includes the superposition principle for matter waves leading to quantum coherence. Spatial coherence, the fixed phase relation between local emitters of matter waves, leads to interference that can be observed in Young's double slit experiments [2, 3].

As a further consequence of the wave character of matter and the related uncertainty principle it was predicted that all bosons of an ensemble may occupy a single energetic ground state, forming a new state of matter [4, 5]. This so-called Bose-Einstein condensate (BEC) cannot be found in nature and it took more than 50 years of research to produce such a many-body quantum state. Finally, it has been realized in dilute gases of alkali metals [6–8] based on the understanding of cooling and trapping of neutral atoms by means of laser light [9–13], and the development of magnetic traps in combination with rf-forced evaporative cooling [14–17]. The first realizations sparked vivid research activities investigating the fundamental properties. Spatial coherence was one of the first properties investigated in such a gas [18]. Furthermore, collective excitations such as propagation of sound and shape oscillations have been studied [19–22] and the early studies have been nicely summarized [23, 24].

Apart from coherence another fascinating consequence of the macroscopic quantum mechanical wavefunction is superfluidity. In superfluids an obstacle can move through the medium without experiencing any friction as long as the velocity remains below a critical value [25–27]. Recent studies transposed the concept of stirring the BEC with a repulsive laser beam to 2D gases and were able to reduce the size of this obstacle to the intrinsic length scale of the system

[28–30]. The breakdown of superfluidity at the critical velocity applies not only to macroscopic objects such as the stirring laser that has been used in many studies but also to impurity atoms immersed in a BEC [31].

Impurity atoms in a BEC can be created by exciting one atom from the ensemble optically [32, 33]. Studies with Rydberg atoms immersed in ultracold gases have attracted a lot of attention as the size of such an atom can be precisely controlled via the excitation of different principal quantum numbers. As a Rydberg atom can be larger than the inter-particle distance, a new type of interaction with the BEC emerges allowing for long-range interactions and the formation of exotic molecules [34–36].

Ionic impurities give rise to pronounced long-range interactions introducing a new length and energy scale, hence such systems are often referred to as hybrid quantum systems [37, 38]. To this end cold collisions, controlled chemical reactions and sympathetic cooling of ions in the environment of ultracold atoms have been studied intensively [39–42]. The common experimental approach is to superimpose an atom trap with a trapped ion [43, 44]. However, the micro-motion of the trapped ion fundamentally limits the achievable temperatures, which is a major experimental obstacle. Optical dipole traps for ions are promising candidates to overcome current limitations and reach the ultracold regime [45]. Alternatively, hybrid atom-ion quantum systems may be achieved by creating a single ion out of the ensemble of quantum degenerate atoms using local photoionization. For high densities this can also lead to the formation of ultracold plasma [46, 47].

In this work local ionization on ultrafast time scales is investigated quantitatively, following-up cross section measurements for ultracold ^{87}Rb [48–50]. In contrast to these studies, here the peak intensity of the laser gives access to strong field ionization [51]. In addition to ionization the remaining atoms also experience a momentum kick induced by the transient optical dipole force which has been analyzed in time of flight measurements. Furthermore, the measurements suggest the presence of atom-ion interactions within the quantum gas, although the excess energy of photoelectrons is relatively large in this study. Inspired by the results discussed here, future experiments promise an investigation of more pronounced interactions by tuning the photon energy of the femtosecond laser close to the ionization threshold and thus reducing the kinetic energies of the fragments.

As mentioned in the beginning of this introduction coherence is a key concept in quantum physics, that already has been studied thoroughly for ultracold atomic ensembles. However, the transfer of coherence from quantum degenerate gases to its constituents remains to be explored. Therefore a new experimental setup has been designed that combines local ionization of a ^{87}Rb BEC via femtosecond laser pulses with coincident detection of photoionization fragments. In the new setup photoelectrons shall be created at two distinct locations in the condensate and their interference pattern shall be observed using position-sensitive electron detectors probing

the spatial coherence. Since the ionizing laser beam is pulsed, also the temporal coherence is accessible by introducing a time delay between the two laser spots [52].

Local dissipation induced by the femtosecond laser allows realizing an open quantum system. Its time evolution can be suppressed by continuous measurements, which is known as the quantum Zeno effect [53, 54]. The new setup could extend recent studies on continuous dissipation to the regime of pulsed loss processes [55, 56].

The study of local ionization and subsequent development of a new experimental setup paves the way for novel investigations of spatial and temporal coherence in ultracold matter and offers exciting connections to the fields of open quantum system and hybrid atom-ion systems.

Structure of this Thesis

The thesis is structured in four chapters with sections focusing on individual topics. After the general introduction the experimental setup for studying the interaction of ultracold gases and ultrashort laser pulses is presented. The findings of these studies are given in chapter 3 and discussed in detail. The thesis concludes with the presentation of the new experimental setup allowing the investigation of coherence transfer to photoelectrons emerging from a BEC.

Chapter 2 – Experimental Setup for Photoionization Experiments with ^{87}Rb

This chapter describes the experimental setup used for the measurements presented in chapter 3. It covers cooling and trapping techniques used to prepare ultracold atomic gases. Additionally the generation of ultrashort laser pulses is presented together with the femtosecond laser system.

Chapter 3 – Ultracold Atoms and Ultrafast Lasers

Different aspects of the interaction between femtosecond laser pulses and ultracold atoms have been investigated experimentally. Besides the photoionization in strong light fields the transient optical dipole force has been observed. Furthermore the in-situ dynamics of the atoms has been studied. The chapter presents the experimental results and concludes discussing aspects of atom-ion interaction.

Chapter 4 – Imaging Photoelectrons emerging from a Bose-Einstein Condensate

Studying the coherence transfer to photoelectrons emerging from a degenerate quantum gas is technically challenging and requires a new experimental setup. After compiling the general layout of the experiment, the necessary components have been designed and built in this work. Most of them have been already characterized, so the new setup can be assembled in the near future.

CHAPTER 2

Experimental Setup for Photoionization Experiments with ^{87}Rb

This chapter describes the experimental setup used for the measurements presented in chapter 3. It covers cooling and trapping techniques used to prepare ultracold atomic gases. Additionally the generation of ultrashort laser pulses is presented together with the femtosecond laser system.

Photoionization of ultracold atoms is rarely performed with femtosecond lasers, although the instantaneous creation of ions and photoelectrons provides an interesting approach to a research field ranging from hybrid atom-ion quantum systems to ultracold plasma [37, 47]. Such experiments clearly require a setup to prepare ultracold atoms as well as an ultrafast laser system. This chapter presents the techniques applied in this work to create ultracold atoms and BEC in optical traps and, in a second section, details the femtosecond laser system that generates the ionizing pulses.

Parts of this chapter concerning the setup of the vacuum and the cooling laser system are also presented in the Diploma theses of Alexander Grote [57] and Malene Fricke [58] as well as in the Master's thesis of Tobias Kroker [59]. For the optical dipole trap Markus Pfau [60] and Harald Blazy [61] contributed to the setup and optimization of the system with their Master's theses. The hybrid trap has been presented in the Master's thesis of Harry Krüger [62]. The data analysis framework has been originally developed by Sören Dörscher and adapted for this experiment by Philipp Wessels and the author.

2.1. Preparation of Ultracold Gases

To achieve Bose-Einstein condensation (BEC) in a dilute gas, the critical phase space density $n \times \lambda_{dB} \geq 2.612$ given by the atomic density n and the de Broglie wavelength $\lambda_{dB} = 2\pi\hbar/p$ must be exceeded. Since the temperature T of an ideal gas is related to the mean kinetic energy of the atoms $\langle p_{Rb}^2 \rangle/(2m) = 3/2 k_B T$, the phase space density can be increased by cooling the gas. At the critical temperature the required phase space density is achieved and the atomic gas undergoes the phase transition to the BEC.

Technically different cooling techniques are required as the atoms have to be cooled by 9 orders of magnitude. The experimental sequence illustrated in figure 2.1 begins with three phases of laser cooling followed by two steps of forced evaporative cooling in the hybrid and the optical dipole trap. The creation of an ultracold atomic cloud takes about 30 s. Eventually the cloud is probed using absorption imaging as described in section 2.1.6.

Figure 2.1.: Experimental sequence for creating ultracold atomic clouds.

The first sections of the chapter give physical details of the cooling and trapping mechanisms as well as their technical implementation. It concludes with a description of the femtosecond laser system.

2.1.1. Laser Cooling

Laser light can be used for cooling atoms as it couples to the external degree of freedom via the photon recoil [9]. When a photon is absorbed the atom will experience a momentum transfer $\vec{p} = \hbar\vec{k}_C$ in the propagation direction of the beam. Subsequent spontaneous emission occurs in random direction. So the emission recoil averages out over many absorption-emission cycles and the net momentum transfer can be written as an effective force, the so-called spontaneous force $\vec{F}_{scat} = \hbar\vec{k}_C\Gamma_{scat}$. The scattering rate Γ_{scat} is derived from the optical Bloch equations for a two-level system [63]:

$$\Gamma_{scat} = \Gamma/2 \times I/I_{sat} \times \sigma/\sigma_0$$

It is determined by the natural line width of the transition Γ, the laser intensity I, the saturation intensity I_{sat} and the scattering cross section:

$$\sigma = \sigma_0 \times \frac{1}{1 + \delta^2 + I/I_{sat}} \tag{2.1}$$

For the D2 line in ^{87}Rb $\left(|5S_{1/2}\rangle \rightarrow |5P_{3/2}\rangle\right)$ the natural line width $\Gamma_{D2} = 2\pi \times 6.065\,\mathrm{MHz}$ [64]. The resonant absorption cross section $\sigma_0 = 3\lambda^2/(2\pi)$ for a two-level system is also derived from the optical Bloch equations [65]. The detuning $\delta = 2(\omega_C - \omega_0)/\Gamma$ accounts for an mismatch between the atomic resonance ω_0 and the laser frequency ω_C in units of natural line widths Γ. At the saturation intensity I_{sat} given by:

$$I_{sat} = \frac{\hbar}{12\pi c^2} \times \Gamma \times \omega_C^3 = 16.675\,\mathrm{W\,m^{-2}} \tag{2.2}$$

half of the population is in the excited state and the transition is saturated. The scattering rate reduces with increasing population in the excited state due to the lack of absorbers. In spectroscopy this effect is known as power broadening. The value for I_{sat} given here refers also to the D2-line of ^{87}Rb.

The mechanism based on repeated absoption and re-emission allows cooling by illuminating the atoms with red-detuned laser beams. The angular frequency of the laser ω_L is below the resonance such that only atoms moving with velocity v towards the laser become resonant due to the Doppler shift:

$$\delta = 2(\omega_C - \omega_0 + \vec{k}_C\vec{v})/\Gamma$$

In a setup of three pairs of perpendicular laser beams an atom experience the spontaneous force from each direction. The term *optical molasses* has been coined for this setup since the atomic motion is hindered like in a viscous medium [12]. The lower temperature limit for laser cooling in this picture is given by the isotropic emission of photons and the probabilistic nature of their absorption that cause a random walk in momentum space. The so-called Doppler cooling limit is given by $T_D = \hbar\Gamma/(2k_B) = 141.5\,\mu\mathrm{K}$.

Trapping of neutral atoms is achieved with a restoring force that drives the atoms always back to the center of the trap. This can be implemented using the spontaneous force in combination with the Zeemann effect in a magnetic quadrupole field. The scattering rate Γ_{scat} gets position-dependent and atoms become resonant with one of the red-detuned lasers as they move out of the center. Such a setup is called *magneto-optical trap* (MOT) [11].

Alkali atoms like ^{87}Rb are best suited for laser cooling as their level structure offers closed transitions that allow repeated absorption-emission cycles. The cooling transition in the hyperfine structure of the D2 line is illustrated in figure 2.2. The electronically excited state $|5^2S_{3/2}, F' = 3\rangle$ decays almost completely back to the ground state $|5^2S_{1/2}, F = 2\rangle$. Only a small fraction of atoms decays to $|5^2S_{1/2}, F = 1\rangle$ escaping the cooling cycle which are re-pumped by a second laser.

In the experiment two separate MOT setups are used. A 2-dimensional setup consisting of a magnetic gradient field and two retro-reflected beams is used to capture hot ^{87}Rb atoms released

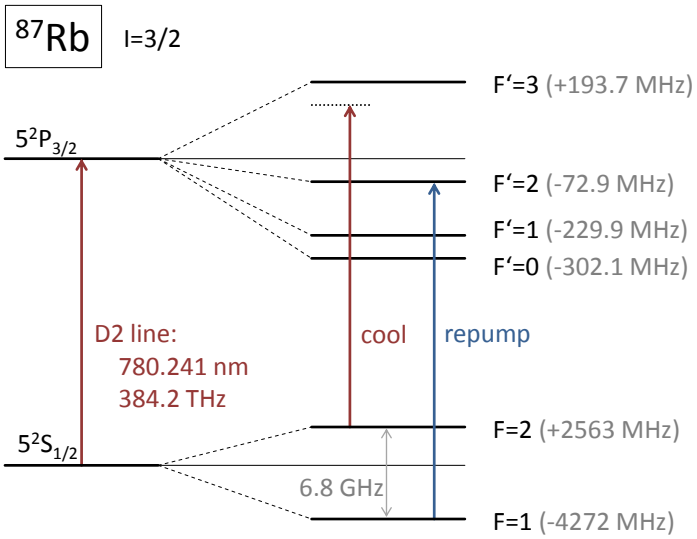

Figure 2.2.: Hyperfine structure of ^{87}Rb. The cooling transition on the D2 lines couples the hyperfine level F=2 to F'=3 in the excited state. A re-pumping beam returns atoms that decay to the ground state F=1 to the cooling cycle.

from the dispensers[1]. It serves as a high flux source of cold atoms for loading a 3D MOT [66]. A pushing beam transfers the atoms from the 2D setup to the 3D MOT. An overview of the complete experimental setup is presented in section 2.1.5.

Cooling Laser System

The laser system is based on two diode lasers[2] and has been setup on a separate optical table. The beams for cooling and re-pumping are transmitted to the experiment via optical fibers. Originally, the system was set up by Malene Fricke [58]. Recently Tobias Kroker has rebuilt it in order to improve the stability and to increase the intensity in the detection beam [59].

Figure 2.3 shows the schematic of the current setup. One of the diode lasers provides the light for the cooling transition, the other one is the re-pumping laser. Both devices offer 40 mW output power and lasers are stabilized in frequency with a saturation spectroscopy setup [58]. The cooling and detection beams each pass a tapered amplifier (TA) which increases the power to 1.5 W [61]. After passing an acousto-optic modulator to adjust the detuning before they are coupled into the optical fibers. The cooling branch is additionally equipped with an electro-optical modulator (EOM) that allows precise intensity control during the optical molasses which allows for temperatures below the Doppler limit [13]. Light for cooling and re-pumping in the 2D MOT is coupled into the same optical fiber whereas for the 3D MOT they are superimposed in a fiber port cluster. The detection beam illuminates the atomic cloud during absorption imaging that is discussed in detail in section 2.1.6.

[1] SAES Getters, Alkali Metal Dispensers
[2] Toptica, DLPro 100

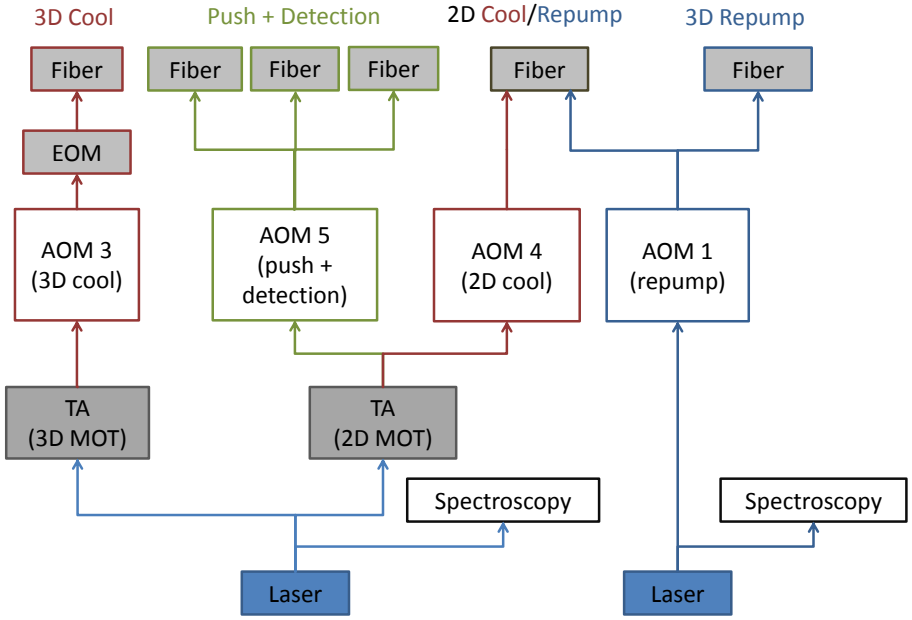

Figure 2.3.: Cooling laser system for ^{87}Rb. Light for cooling and re-pumping is emitted from two diode lasers, both locked to the transition by saturation spectroscopy. The cooling laser seeds two tapered amplifiers to have sufficient power in the cooling and detection branches. The re-pumping laser can be directly coupled into the fibers that guide the beams to the experiment. AOMs in the beam paths adjust the detuning of the beams and are used for switching.

2.1.2. Magnetic Trap and rf Forced Evaporative Cooling

After the atoms have undergone laser cooling they can be confined in magnetic gradient fields. The field couples to the magnetic dipole moment μ of the atom and the potential energy can be written as:

$$U_{mt} = \mu \times B(\vec{r}) \tag{2.3}$$

The dipole moment can be derived from the angular momentum quantum numbers. For ^{87}Rb the total angular momentum $\vec{F} = \vec{L} + \vec{S} + \vec{I}$ of the ground state $|5^2S_{1/2}\rangle$ is given by the electron spin $\vec{S} = 1/2$ and the nuclear spin $\vec{I} = 3/2$. The atoms are prepared in the $F = 2$ state as this is the ground state for laser cooling. The magnetic dipole moment :

$$\mu = \mu_B g_F m_F / \hbar$$

is given by the Bohr magneton $\mu_B = e\hbar/(2m_e)$, the Landé g-factor[3] $g_F = 1/2$ and the z-component $m_F = [0, \pm 1, \pm 2]$ of the total angular momentum. Figure 2.4 illustrates the shape of the trapping potential for a quadrupole field that can be produced by the MOT coils. States with positive quantum number m_F are low field seeking and can be confined in the potential. The

[3]The g_F is calculated according to [67] p. 42.

states with negative m_F are high field seekers and expelled from the trap.

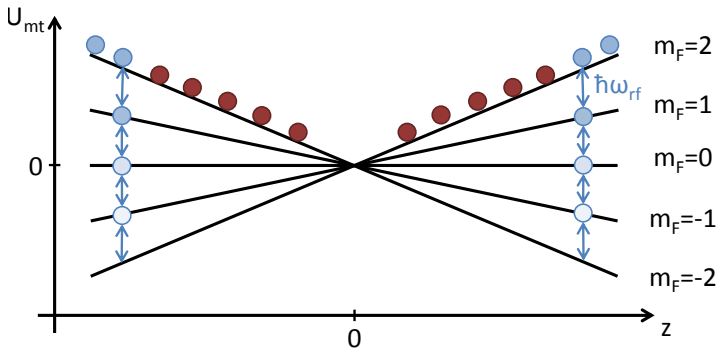

Figure 2.4.: Trapping potential in the magnetic trap. The Zeeman splitting of $|5^2S_{1/2}, F = 2\rangle$ leads to confinement for positive m_F quantum numbers in the gradient field of anti-Helmholtz coils. Radio frequency radiation with energy $\hbar\omega_{rf}$ couples the m_F states and leads to forced evaporative cooling by sweeping the frequency to lower values.

Magnetic traps are conservative, therefore the atoms are cooled by *rf forced evaporation* [15]. As the atoms with high kinetic energy can reach far out in the potential they also experience the large Zeemann splitting in the field. A radio frequency sweep from 16 MHz to 1 MHz couples $m_F = 2$ to lower states and removes all atoms having a large kinetic energy. The sweep has to be slow enough to allow for continuous re-thermalization of the remaining atoms.

Since the quadrupole field vanishes in the center of the trap the quantization axis is undefined. Thus spin changes into anti-trapped states can occur at $B = 0$, so-called Majorana spin flips [68]. The colder the atoms become due to evaporation the higher is their probability to be found at the trap center, hence Majorana losses become more and more severe for cold samples. The losses must be avoided by either adding an offset magnetic field as it is done in time-orbiting potential traps and the Ioffe-Pritchard traps [8, 14] or by adding an optical potential that keeps the atoms away from $B = 0$ [6, 69].

Our Ioffe-Pritchard type magnetic trap has been set up by Philipp Christoph and Malene Fricke and features trap frequencies of $\omega_{mt,\rho} = 2\pi \times 98.8\,\text{Hz}$ and $\omega_{mt,z} = 2\pi \times 27.3\,\text{Hz}$ [70, 58]. During the master's work of Harry Krueger a hybrid trap was implemented that combines a magnetic quadrupole field with a gradient of $1.32\,\text{T}\,\text{m}^{-1}$ and a red-detuned optical dipole trap [62, 69].

2.1.3. Optical Dipole Trap

The light field $\vec{\mathcal{E}}_{dip}$ of a laser beam induces an electric dipole moment $\vec{p} = \alpha \times \vec{\mathcal{E}}_{dip}$ for an atom having the polarizability α. As the beam profile of a focused laser is inhomogeneous the field exerts a classical force $\vec{F}_{dip} = 1/2 \times \nabla\langle\vec{p} \cdot \vec{\mathcal{E}}_{dip}\rangle$ on the atom. A more accurate description can be formulated in the quantum mechanical dressed atom picture. A red-detuned laser beam lowers the potential energy of the atomic ground state [71], thus the beam profile of a Gaussian laser

beam creates an attractive potential for the atom. The confinement in transverse direction is strong compared to the longitudinal direction as the intensity gradient is larger. The potential for the ^{87}Rb ground state can be written as [72]:

$$U_{dt} = -\frac{\pi c^2}{2} \times \left[\frac{\Gamma_{D1}}{\omega_{D1}^3} \left(\frac{1}{\omega_{D1} - \omega_{dip}} + \frac{1}{\omega_{D1} + \omega_{dip}} \right) + \frac{2\Gamma_{D2}}{\omega_2^3} \left(\frac{1}{\omega_{D2} - \omega_{dip}} + \frac{1}{\omega_{D2} + \omega_{dip}} \right) \right] \times I(x, y, z) \tag{2.4}$$

The relevant transitions are the D1 and D2 lines with the natural linewidths

$$\Gamma_{D1} = 2\pi \times 5.746\,\text{MHz}$$
$$\Gamma_{D2} = 2\pi \times 6.065\,\text{MHz}$$

and the angular transition frequencies [64]

$$\omega_{D1} = 2\pi \times 377.107\,463\,5\,\text{THz}$$
$$\omega_{D2} = 2\pi \times 384.230\,484\,468\,5\,\text{THz}.$$

The timescale for dynamics in the trap is determined by the trap frequency. It is derived from the harmonic approximation to the potential at the center of the trap:

$$\omega_{dt} = \sqrt{\frac{1}{m_{Rb}} \frac{\partial^2 U_{dt}}{\partial r^2}} \Bigg|_{min(U_{dt})} \tag{2.5}$$

In optical dipole traps forced evaporative cooling can be performed by slowly lowering the laser intensities. So the trapping potential is lowered and atoms with high kinetic energy will leave the ensemble. As the confinement along the beam axis is rather weak crossed dipole traps are implemented using two perpendicular trapping beams. In this way Bose-Einstein condensation can be achieved [73].

Trapping Laser System

The optical dipole trap is based on a commercial laser system[4] that combines a master oscillator running at $\lambda_{dip} = 1064\,\text{nm}$ with a fiber amplifier. The setup depicted in figure 2.5 has been built in the Diploma's project of Markus Pfau [60]. The optical output power of 18 W is distributed across two beam paths one for each axis of the crossed dipole trap. Waveplates allow to adjust the power ratio of both branches. The beams pass AOMs that are used for switching the beams and stabilizing their intensity. The feedback for the stabilization is generated from photodiode at the end of the beam path. Their signal is fed into PID loops that control the rf-intensity in

[4] Innolight, Mephisto MOPA 15 NE

the AOM. Additional shutters in front of the fiber couplers prevent leakage from the AOMs. On

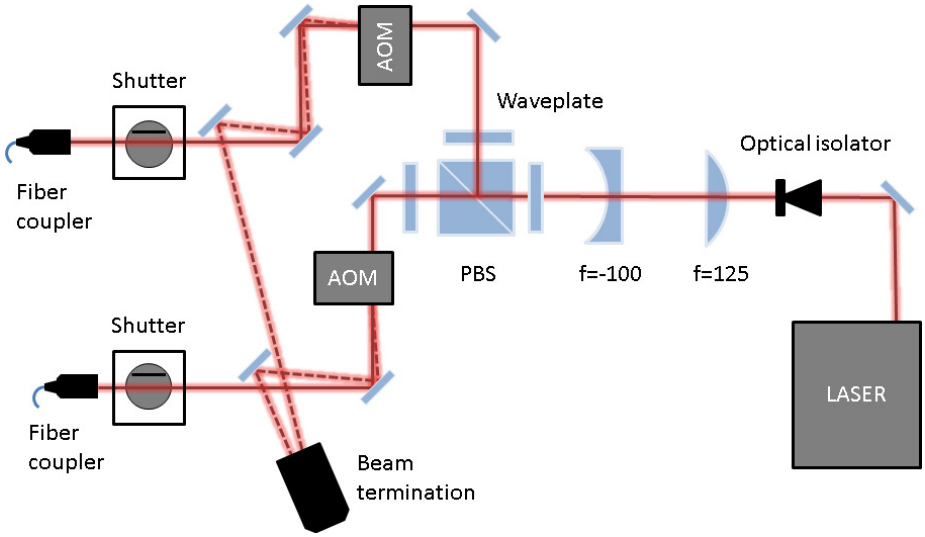

Figure 2.5.: Laser system for the optical dipole trap. The beam is split up into two branches using a polarizing beam splitter (PBS). The power ratio can be adjusted with waveplates. Both beams of the crossed dipole trap are intensity stabilized using AOMs.

the experiment side the fibers are connected directly to the focusing fiber telescopes. The beam along the MT coils axis exhibits a waist of $w_{strong} = 44\,\mu m$. Its smaller waist leads to a stronger confinement as compared the perpendicular beam with $w_{weak} = 84.6\,\mu m$ [61].

2.1.4. Hybrid Trap

As mentioned above hybrid trap consisting of linear magnetic potential and a superimposed optical trap does not suffer from Majorana losses when the laser beams are aligned slightly below the center of the Helmholtz coils. The trapping potential is simply given by the sum of the trapping potentials:

$$U_{ht} = U_{mt} + U_{dt} + m_{Rb} \times g_0 \times z.$$

Note, the gravitational potential is taken into account, since it becomes relevant at small laser intensities in the optical dipole trap. The tilt in the potential induced by gravity determines the trap depth for the dipole trap. The trapping potentials for the hybrid trap before forced evaporation and the optical dipole trap at the final laser intensities are plotted in figure 2.6.

2.1.5. Experimental Setup

The experimental setup is illustrated in figure 2.7. It consists of two glass cells that are interconnected by a small channel in order to maintain a pressure difference between both cells. The intermediate part is made from stainless steel and provides flanges for connecting the

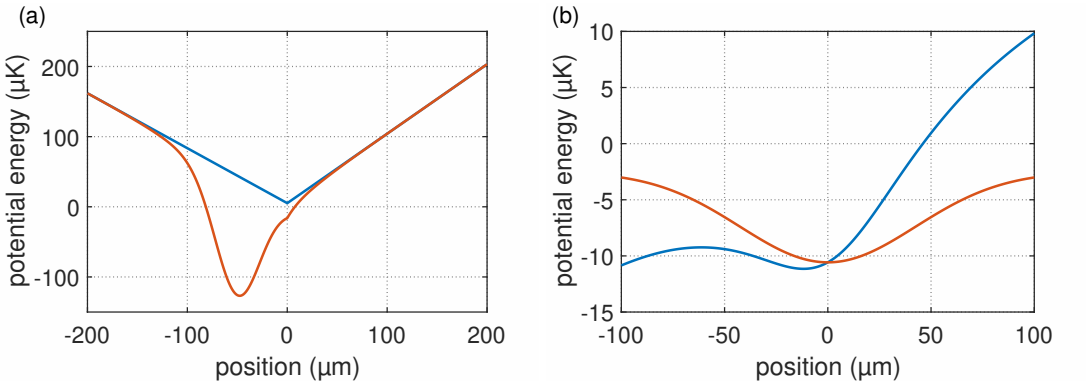

Figure 2.6.: Optical trapping potentials. (a) Potential of the hybrid trap (red) along the vertical axis. The magnetic potential (blue) is superimposed with the trapping beams ($P = 3\,\mathrm{W}$) that is aligned 50 µm below the B-field minimum. (b) Potential of the crossed optical dipole trap in horizontal direction (red) and vertical direction (blue) after evaporation. BEC can be achieved at low laser intensities ($P_{strong} = 0.05\,\mathrm{W}$, $P_{weak} = 0.6\,\mathrm{W}$) where gravity significantly tilts the vertical potential. The gravitational sag shifts the minimum by circa 10 µm

.

vacuum pumps [74, 57]. In the upper cell where the Rubidium atoms are emitted from so-called dispensers the operation pressure is on the order of 5×10^{-8} mbar. The atoms are pre-cooled in a 2D MOT before they are transfered through the channel into the lower glass cell using a pushing beam. Here the pressure ($<1 \times 10^{-11}$ mbar) is significantly lower in order to allow for long trapping times. The atom number in the 3D MOT saturates after 5 s to 10 s and the sample is transferred into the hybrid trap after an intermediate optical molasses phase. In the hybrid trap the sample is cooled further by rf-evaporation until only the volume of the trapping beam is occupied. The magnetic field is turned off and by lowering the intensity in the trapping beams the BEC transition is achieved. Finally measurements of the density profile can be performed in the trap (*in-situ*) or after time of flight by means of absorption imaging.

The life time in the optical dipole trap has been measured in figure 2.8. The exponential decay over $t_{1/2} = 11.4\,\mathrm{s}$ is determined by collisions with the background gas. The trap frequencies can be measured by exciting center of mass motion in the trap. This can be done by temporary modification of the intensity of one trapping beam. After variable hold time and fixed time of flight the position of the atoms nicely shows an oscillation with the trap frequency that is plotted in figure 2.9. The shot-to-shot fluctuations of atom number can be optimized by careful alignment of the trapping beams. In this work it typically is on the order of 10 %.

The experimental sequence sketched in figure 2.1 is controlled by a real time computer[5] [75]. The program is split into time slots of variable length that define the different states of the experiment (e.g. 3D MOT). The real time program can be altered using a LabView interface running on a standard laboratory computer which allows for automatic parameter scans. Each

[5] Jäger Computergesteuerte Messtechnick GmbH, ADwin-Pro II

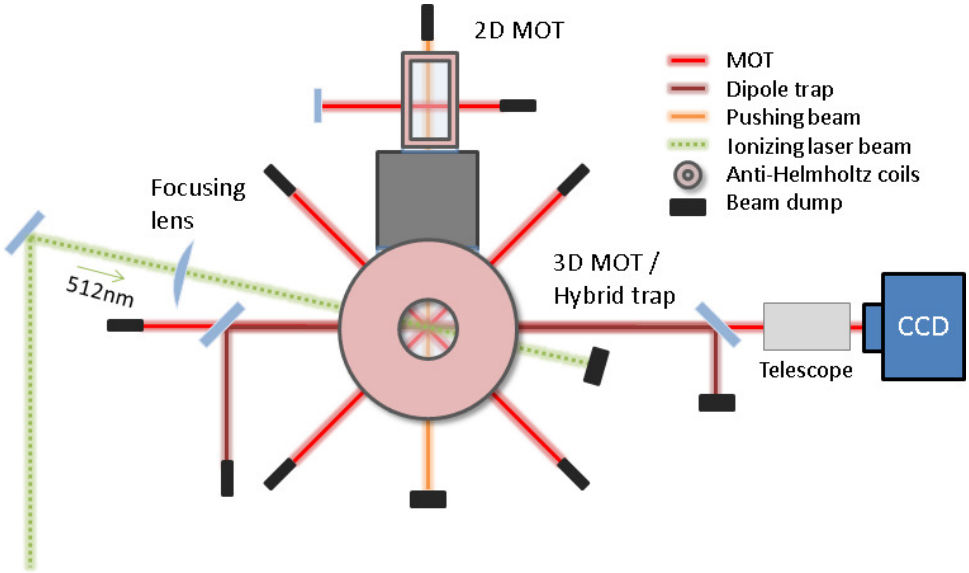

Figure 2.7.: Setup for photoionization of ultracold atoms. The ^{87}Rb atoms emerge from dispensers in the upper glass cell. After pre-cooling in a 2D MOT setup they are pushed down to the 3D MOT cell (hidden behind the round coils). Here the sample can be cooled until they form a Bose-Einstein condensate. After interaction with the femtosecond beam (inclined by about 13°) the remaining atoms are imaged along the horizontal axis.

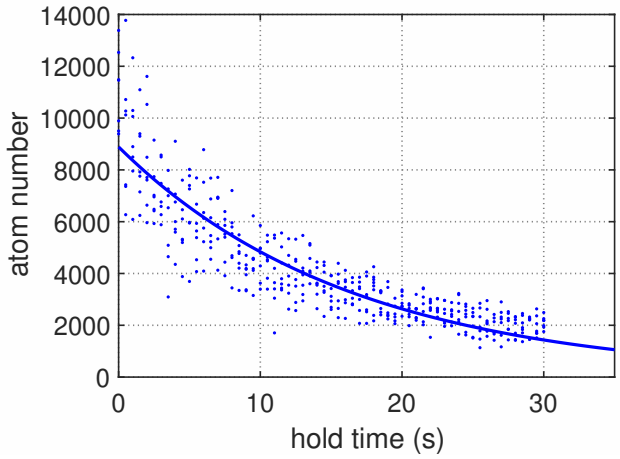

Figure 2.8.: Lifetime in the optical dipole trap. The number of atoms decays due to collisions with residual background gas with time constant $t_{1/2} = (11.4 \pm 0.6)$ s.

run of the experimental sequence is saved in a protocol file.

2.1.6. Data Acquisition and Analysis

The final step of each experimental cycle is the imaging process as illustrated schematically in figure 2.10. A collimated laser beam that is co-linear with the weak axis of the dipole trap and resonant with the D2-line of ^{87}Rb illuminates the atomic cloud. The atoms efficiently scatter

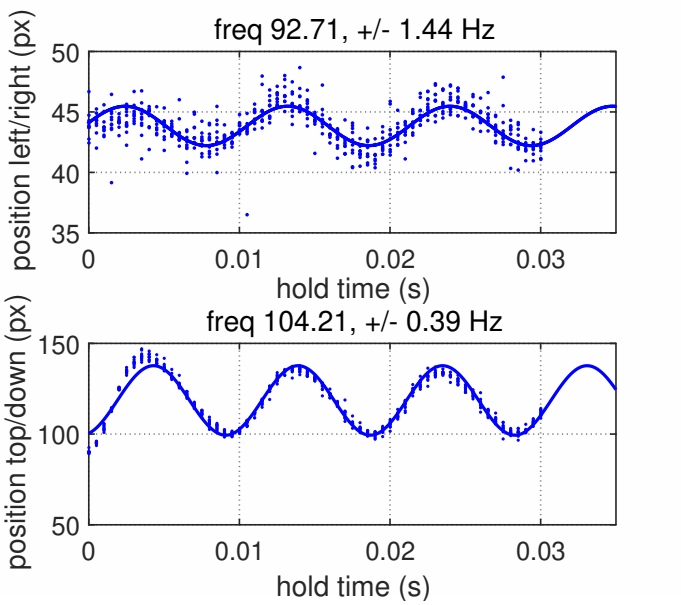

Figure 2.9.: Trap frequencies in the optical dipole trap. After variables hold times in the trap the frequencies $f_{xy} = (92.7 \pm 1.4)$ Hz in the horizontal plane (upper plot) and $f_z = (104.2 \pm 0.4)$ Hz in the vertical direction (lower plot) are determined from the center of mass positions after time of flight.

photons out of the beam casting a shadow onto a CCD camera[6]. The imaging system has a resolution of 3 µm. During the illumination the atoms acquire significant photon recoil which makes the absorption imaging a destructive detection method.

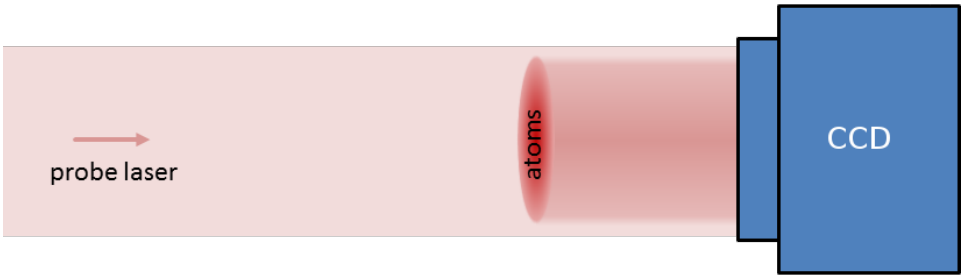

Figure 2.10.: Principle of absorption imaging. Atoms are illuminated with a laser resonant with the D2 lines for 50 µs. The CCD thus measures the transmittance of the sample.

Absorption images provide access to the column density $\tilde{n} = \int n(x, y, z)\, dy$. The expression to actually calculate it can be derived using the Beer-Lambert's law:

$$dI = n(y)\sigma I dy \tag{2.6}$$

It states that the absorption of light in a medium of density $n(y)$ and thickness dy is proportional

[6]PCO AG, pco.pixelfly usb

to the incoming intensity I and the absorption cross section σ. Integration leads to the commonly known form of the absorption law $I = I_0 \times e^{-\sigma n y}$. Inserting equation (2.6) into the definition of the column density $\tilde{n} = \int n\, dy$ gives:

$$\tilde{n} = \int_{-\infty}^{\infty} n(x, y, z)\, dy = \int \frac{1}{\sigma}\frac{1}{I}\frac{dI}{dy} dy = \int \frac{1}{\sigma}\frac{1}{I} dI \tag{2.7}$$

The integration can be carried out using the scattering cross section $\sigma(I)$ defined in equation (2.1) while changing the integration variable from y to I the boundaries $y = \pm\infty$ change to $I(y = \pm\infty) = I_{ref/abs}$, where I_{ref} and I_{abs} are the probe light intensities in front and behind the atoms. Now the column density can be written as:

$$\tilde{n}\sigma_0 = -(1 + \delta^2) \times ln\left(\frac{I_{ref}}{I_{abs}}\right) + \frac{(I_{ref} - I_{abs})}{I_{sat}} \tag{2.8}$$

The expression $\tilde{n}\sigma$ is often called optical density (OD). In order to measure the column density two images are required: One with atoms and one empty bright field image.

Image Processing

The calculation of column densities from the raw images requires two corrections that were not mentioned so far because of their technical nature. Firstly, in the experiment there is always some stray light left. Therefore dark field images are subtracted pixel-wise from the absorption and reference image before they are saved.

$$\mathcal{I}_{abs}(x, y) = \mathcal{I}_{abs,0}(x, y) - \mathcal{I}_{dark}(x, y)$$
$$\mathcal{I}_{ref}(x, y) = \mathcal{I}_{ref,0}(x, y) - \mathcal{I}_{dark}(x, y)$$

In addition, timing jitter of electronic and mechanical components and intensity fluctuations of the probe beam lead illumination variations in the stored images. To compensate this the reference image is normalized to a region of interest (ROI) that contains no atoms. This is called exposure correction.

$$\mathcal{I}_{ref,e}(x, y) = \mathcal{I}_{ref}(x, y) \times \frac{\sum_{ROI} \mathcal{I}_{abs}(x, y)}{\sum_{ROI} \mathcal{I}_{ref}(x, y)}$$

In order to calculate the OD from the pixel values in the camera images they have to be converted to absolute intensities $I(x, y) = c_I \times \mathcal{I}(x, y)$, where:

$$c_I = \frac{G \times \hbar\omega_{det}}{q_{eff}(\lambda_{det}) \times T(\lambda_{det}) \times \tau}\left(\frac{M}{s_{px}}\right)^2 = 0.0368\,\mathrm{W\,m^{-2}}. \tag{2.9}$$

This conversion factor takes into account the gain of the camera G, its quantum efficiency q_{eff},

its pixel size s_{px}, the angular frequency ω_{det} of the probe beam, the magnification M and the transmittance T of the imaging system as well as the exposure time $\tau = 50\,\mu s$. The quantum efficiency and the transmittance of course depend on the detection wavelength λ_{det}. Finally the optical density from equation (2.8) reads:

$$OD(x,y) = -\underbrace{(1+\delta^2)}_{\text{det. corr.}} \times \ln\left(\frac{\mathcal{I}_{ref,e}}{\mathcal{I}_{abs}}\right) + c_I \times \underbrace{\frac{\left(\mathcal{I}_{ref,e} - \mathcal{I}_{abs}\right)}{I_{sat}}}_{\text{saturation corr.}} \tag{2.10}$$

The total number of atoms in an absorption images can be obtained by integrating the optical density:

$$N_{atoms} = \left(\frac{s_{px}}{M}\right)^2 \times \frac{1}{\sigma_0} \times \sum_{x,y} OD(x,y). \tag{2.11}$$

Maximum Optical Density

The optical density can only be measured as long as some light passes the sample. From (2.8) it is clear that the optical density diverges for high absorption signal because the transmitted intensity I_{abs} is written to the denominator. The maximum OD that can be measured in the experiment is determined by the dynamic range of the CCD camera and the shot noise of the light pulse.

A signal can only be detected if the number of counts in the absorption image $\mathcal{I}_{abs}$ is significantly larger than the noise level of the camera. The readout noise of the camera $s_R = 6$ adds to the shot noise $\sqrt{\mathcal{I}}$ in the bright field image as well as in the dark field image [76]. The common rules for propagation of uncertainty apply and give to a total error of

$$s_{abs} = \sqrt{\left(\sqrt{\mathcal{I}_{abs,0}} + s_R\right)^2 + \left(\sqrt{\mathcal{I}_{dark}} + s_R\right)^2} \tag{2.12}$$

A significant absorption signal shall meet the condition $\mathcal{I}_{abs} - 3 \times s_{abs} \geq s_R$ meaning that valid measurements require a distance of 3 standard deviations from the noise level of the camera. Solving this inequation for dark images having an average count number of approximately $\mathcal{I}_{dark} = 20$ yields the minimum count number for a significant value in an absorption image $\mathcal{I}_{abs,min} = 77$.

For reliable measurements it is necessary to avoid saturation of the CCD chip. A pixel filling of 75 % is typical in the data. The 12 bit camera can take $\mathcal{I}_{ref} = 0.75 \times 2^{12} = 3072$ counts for a bright pixel. Calculating the maximum optical density without saturation correction for this case gives:

$$OD_{max} = \ln\left(\frac{\mathcal{I}_{ref}}{\mathcal{I}_{abs,min}}\right) = \ln\left(\frac{3072}{77}\right) = 3.7 \tag{2.13}$$

With saturation correction included the maximum OD evaluates to 10.3.

To complete this consideration the peak intensity of the probe beam can be calculated from the maximum counts on the CCD chip:

$$I_{probe} = c_I \times \mathcal{I}_{ref} = 6.8 \times I_{sat}.$$

The intensity of the probe beam is 6.8 times larger than I_{sat}. This violates the assumption of weak illumination made for Beer-Lambert's law (2.6). The accuracy of the measurements can be improved with a careful calibration of the imaging system [77]. By varying the intensity of the probe beam it is possible to determine a calibration factor that can be inserted in front of the logarithm in equation (2.10). A second factor is needed for short exposure times as the temporal shape of the illuminating pulse becomes important [78].

Post Processing

Besides absorption images also protocol files are stored for each run. They contain all computer controlled parameters characterizing each experimental run. During post processing all images from a measurement are collected and combined with the relevant experimental parameters.

Additionally the images are analyzed in detail. Figure 2.11 shows an image of atoms in the optical dipole trap after analysis with a 2D fit function. In this example the cloud was illuminated with the femtosecond laser that induced a void in the center. The top left corner shows the recorded optical density. The image in the bottom right corner shows the result recontruction by the fit. The other two plots show column and line profiles (sums) respectively. Here the fit function is composed of two 2D Gaussians. One with positive amplitude to model the cloud, one with negative amplitude to model the density reduction in the center.

Although this model has 13 free parameters it often turned out to work reliably, especially when the central density variation is low. But in some cases it was more stable to apply 1D fit functions to the column or rows sums.

2.1.7. Summary

To prepare a ultracold atomic cloud a sequence of trapping and cooling methods is applied. The ^{87}Rb atoms emitted from a dispenser undergo laser cooling and are transfered to a hybrid trap were rf forced evaporative cooling is applied. Finally they are trapped in an optical dipole trap and the transition to BEC can be achieved in a last step of forced evaporation.

The last step of each experimental cycle is absorption imaging. The atomic cloud is illuminated with resonant light and imaged onto a CCD camera. The resolution of the imaging system is 3 µm. The section concludes with remarks on the maximum optical density that can be measured as this is crucial for the analysis of the density profiles extracted from the camera data.

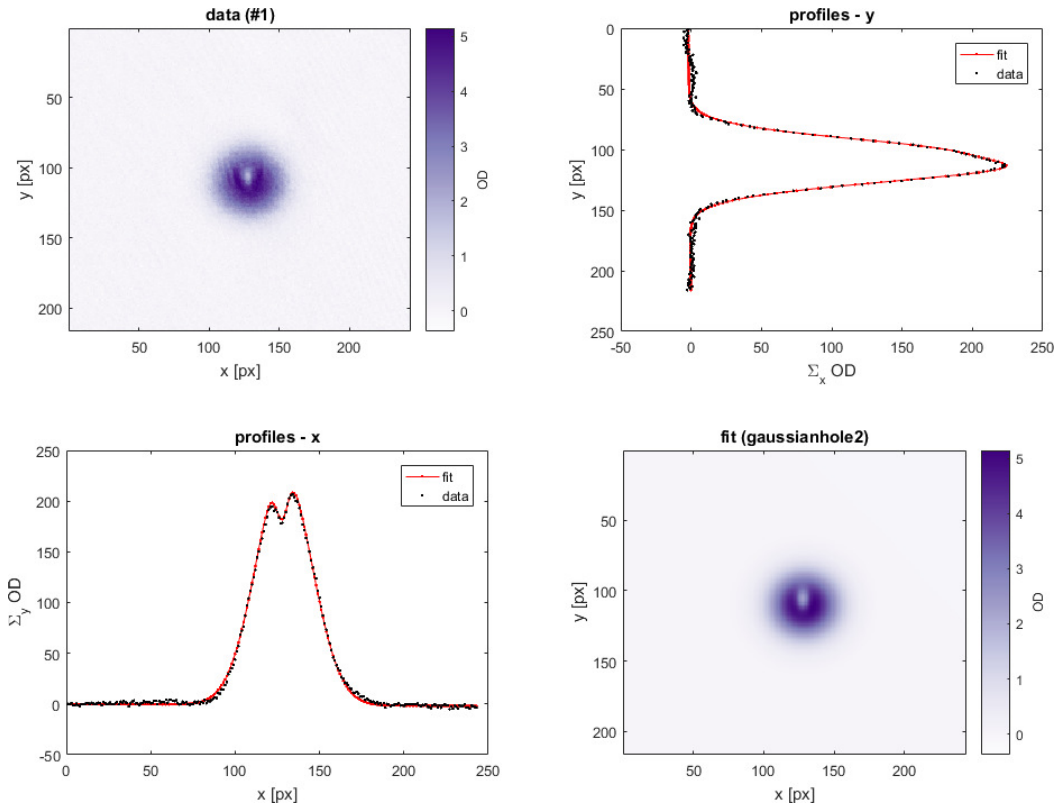

Figure 2.11.: Analysis of an absorption image. The top right panel shows the recorded optical density profile. The panel in the lower right corner shows the corresponding fit result. The other two plots show the row and column sums respectively.

2.2. Femtosecond Laser Pulses

The generation of ultrashort laser pulses relies on purely optical techniques as mechanical or electronic switching are not fast enough. This section gives a brief overview on the generation, amplification and frequency conversion of ultrashort pulses, before the components of the femtosecond laser system used in this work are presented.

2.2.1. Ultrashort Laser Pulses

The pulse duration of ultrashort laser pulses is in the picosecond regime and below. A technique called *mode locking* is commonly used to generate such pulses [79]. The idea is to establish a fixed phase relation between many longitudinal modes of the laser resonator by modulating its quality factor. The superposition of these modes (see figure 2.12) results in a wave packages moving back and forth in the laser cavity. From the Fourier transform it is obvious that shorter pulses can be obtained by superimposing more and more longitudinal modes, thus increasing the bandwidth of the pulse. The laser system[7] used here relies on a passive technique called Kerr lens mode locking. It exploits the non-linearity of the refractive index that leads to additional focusing of the beam for high intensities as illustrated in figure 2.13. The laser oscillator is designed in a way that the Kerr medium in the resonator reduces the losses for high intensities as it induces additional focusing. Hence pulsed operation is favored because ultrashort pulses exhibit high peak intensities. The oscillator of the laser is based on a Yb:$KGd(WO_4)_2$ solid state

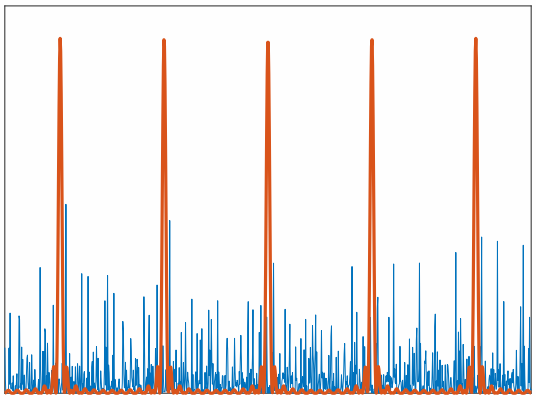

Figure 2.12.: Mode locking. Establishing a fixed phase relation between many modes in a laser cavity creates a train of ultrashort pulses (red). Random phase relations lead to the typical intensity noise. The plot illustrates the superposition of 11 sinusoidal modes.

gain medium and generates pulses with $\tau_{FWHM} = 277\,\text{fs}$ duration at $\lambda_F = 1024\,\text{nm}$ wavelength with $f_{osc} = 83\,\text{MHz}$ repetition rate [80].

[7] Light Conversion, Pharos PH1-06

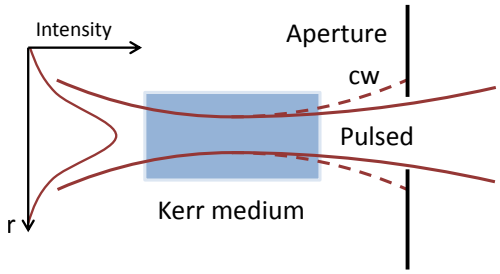

Figure 2.13.: Kerr lensing. Due to its non-linear refractive index the Kerr medium focuses light at high intensities. In a laser resonator with a Kerr lens mode-locked operation is favored over continuous wave (cw) as pulses exhibit high peak intensities and thus experience lower loss at the aperture.

The mode-locked pulses emitted from the resonator are amplified using *chirped pulse amplification* [81]. Before amplification the pulses are temporally stretched by inducing a positive chirp with a set of gratings in order to avoid damage to the optical elements. Subsequent insertion into the cavity of a *regenerative amplifier* leads to amplification of the pulse in a pumped gain medium during multiple cavity round trips. Finally, the pulses are compressed again by a second set of gratings that compensates the induced chirp. The amplifier provides a maximum output power of 6 W of infrared radiation. The pulse repetition rate is set to $f_{rep} = 100\,\mathrm{kHz}$. In addition the laser is equipped with an internal pulse picker allowing for arbitrary patterns in the pulse train.

Non-linear optical mediums allow also for frequency conversion of intense lasers. Second harmonic generation or frequency doubling (see figure 2.14 (a)) can be achieved by focusing the beam into a material that exhibits a second order susceptibility $\chi^{(2)}$. In the classical picture the response of dielectric material is given by the polarization density $\vec{P} = \chi\epsilon_0\vec{\mathcal{E}}$ that linearly depends on the susceptibility χ. An incident beam drives the elementary oscillators of the medium as it travels through. At high intensities the harmonic approximation for theses oscillators is not valid anymore. Then it becomes necessary to take higher orders of the electric field $\mathcal{E}$ into account and the polarization density is $\vec{P} = \chi\epsilon_0\vec{\mathcal{E}} + \chi^{(2)}\epsilon_0\vec{\mathcal{E}}^2 + \dots$. In this non-linear regime second (or higher) order radiation can be emitted. For efficient conversion it is necessary that the waves at fundamental and doubled frequency travel at the same speed inside the medium. As non-linear crystals are birefringent, this phase matching condition can be satisfied by adjusting the orientation of the crystal axes with respect to the incoming beam.

Closely related to second harmonic generation is *optical parametric amplification* (see figure 2.14 (b)). Here a pump photon with angular frequency ω_2 is converted into a signal photon with ω_1 while a third photon, the idler, conserves energy and momentum [79]. The process does not necessarily require an incident signal photon as the phase matching condition already defines the outgoing frequency, but the process is much more efficient when the signal light is present. A weak signal beam for seeding the OPA is usually obtained by selecting the desired wavelength

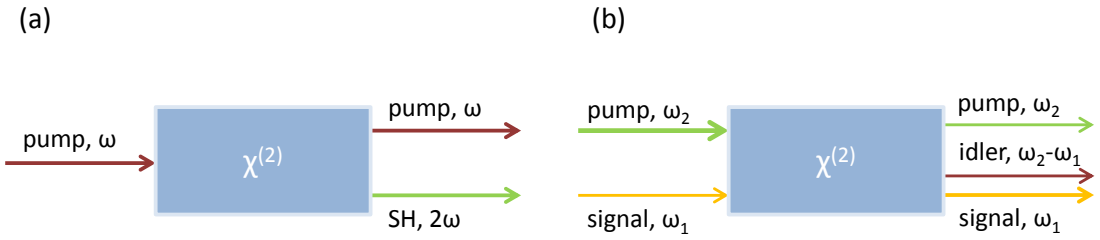

Figure 2.14.: Non-linear optical processes. (a) In second harmonic generation the frequency of the incident pump beam is doubled by converting 2 pump photons into 1 SH photon. (b) Optical parametric amplification splits the pump photons into 1 signal and 1 idler photon, thus the signal beam is amplified. The conversion efficiency is below unity and there are residual pump photons exiting the non-linear medium.

from a white light continuum [82].

2.2.2. Femtosecond Laser System

The mobile femtosecond laser system has been set up for time-resolved measurements at the PETRA III synchrotron in Hamburg [83, 84]. But it is also available for laboratory use when it is not at the beamline [85]. For the broadest possible application it is a modular system that consists of the laser itself, the harmonics module and an optical parametric amplifier (OPA) which allow for frequency conversion of the fundamental wavelength. As illustrated in figure 2.15 mirrors on magnetic index mounts allow a quick change between the different modules. Silver mirrors are used to propagate the beam efficiently at all wavelengths.

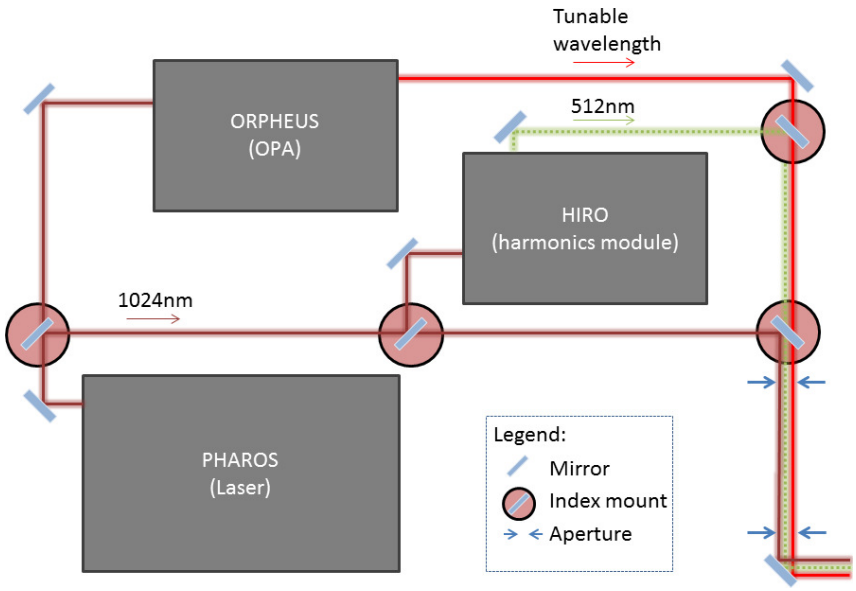

Figure 2.15.: Femtosecond laser system. The PHAROS laser seeds either the harmonics module HIRO or the OPA with IR radiation. By adding and removing the mirrors on index mounts it is easy to switch between PHAROS, ORPHEUS and HIRO.

The harmonics module[8] is used to generate the second harmonic. The actual wavelength $\lambda_{SH} = 511.4\,\text{nm}$ with bandwidth of 1.7 nm at full width half maximum has been measured using a spectrometer[9]. The module can also generate the third and forth at 323 nm and 257 nm, respectively, but this feature has not been used in this work. It is able to produce about $P_{avg} = 3\,\text{W}$ average power, however, only a few milliwatts are necessary to achieve the intensities required for the photoionization experiments presented in chapter 3. The focus size has been measured directly with a CMOS camera. Figure 2.16 shows three false color images near the beam waist which were taken with an axial distance of 20 µm to each other. The average size $w_0 = (12.5 \pm 0.8)\,\mu\text{m}$ is calculated from a number of cuts through the central image. The strong astigmatism is induced by slight misalignment of collimation telescopes in the harmonics module.

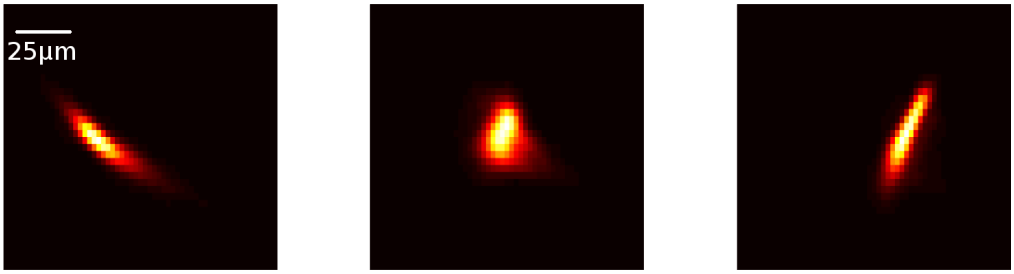

Figure 2.16.: False Color images of the beam profiles for $\lambda_{SH} = 511.4\,\text{nm}$ wavelength. A strong astigmatism is observed with a separation between the line foci of 40 µm. In the experiments the round focus is used. Its waist is $w_0 = (12.5 \pm 0.8)\,\mu\text{m}$.

The OPA[10] offers a lot of flexibility regarding the wavelength on cost of output power. The tuning range almost spans from 200 nm to 3000 nm. The parametric amplification stages are pumped with the second harmonic allowing the generation of laser pulses from 600 nm to 3000 nm. By subsequent frequency doubling it is possible to scan across the two-photon ionization resonance of ^{87}Rb. Although first wavelength dependent experiment have been performed in the course of this work it focuses on the measurements with the second harmonic. Photon energies close to the two-photon ionization threshold will be key for subsequent experiments using a new setup that is presented in chapter 4.

[8] Light Conversion, HIRO Customizable Harmonic Generator for PHAROS
[9] PhotonControl, SPM-002-E
[10] Light Conversion, ORPHEUS Collinear Optical Parametric Amplifier

2.3. Conclusion

A setup for preparing ultracold clouds in the optical dipole trap was presented. After initial laser cooling the atoms are transfered into a hybrid trap were rf forced evaporative cooling is applied until they can be confined in the optical potential of two crossed IR laserbeams with. By reducing their intensity the atomic cloud can reaches the critical temperature. The trap is nearly spherical and the trap frequencies are close to 100 Hz. The lifetime $t_{1/2} = 11.4$ s is limited by backround collisions. The density profile of the atomic cloud can be measured with a spatial resolution of 3 µm by means of absorption imaging.

The femtosecond laser system, presented in the second part of this chapter, generates pulses with $\tau_{FWHM} = 277$ fs at $\lambda_F = 1022$ nm wavelength. For the experiment the fundamental frequency is doubled in a harmonics module. The second harmonic beam exhibits $\lambda_{SH} = 511.4$ nm wavelength and a 12.5 µm focus.

CHAPTER 3

Ultracold Atoms and Ultrafast Lasers

Different aspects of the interaction between femtosecond laser pulses and ultracold atoms have been investigated experimentally. Besides the photoionization in strong light fields the transient optical dipole force has been observed. Furthermore the in-situ dynamics of the atoms has been studied. The chapter presents the experimental results and concludes discussing aspects of atom-ion interaction.

Femtosecond laser pulses are widely used to probe ultrafast dynamics in atomic and molecular systems but are rarely used in the context of ultracold atoms [49]. Such laser pulses feature high peak intensities allowing for non-linear processes like strong field ionization in the atomic cloud. Probing Bose-Einstein condensates by local ionization offers a novel tool to measure the atomic density in situ and to investigate exciting phenomena like the quantum Zeno dynamics [55, 56]. It also can be an interesting technique for the emerging field of ultracold hybrid atom-ion systems [37].

This chapter presents detailed investigations of the strong field ionization of ultracold ^{87}Rb using femtosecond laser pules. The nature of the ionization process is studied by analyzing the number of atoms lost from the trap after applying ultrashort pulses (section 3.1). The pulses also trigger dynamics in the atomic cloud due to the transient optical dipole force (section 3.2). In-situ dynamics of thermal atoms after a number of pulses have been observed in section 3.3. The chapter concludes with the observation of atom-ion interaction effects that indicate the creation of hybrid atom-ion systems (section 3.4).

Experimental data presented in this chapter have been obtained within the team of Juliette Simonet, Philipp Wessels, Bernhard Ruff, Alexander Grote, Jasper Krauser, Tobias Kroker, Harry Krüger and Harald Blazy. Analysis of the experimental data presented in this chapter has

been performed by the author. Preliminary results are presented in the Master's thesis of Tobias Kroker [59].

3.1. Photoionization in Strong Light Fields

The alkali metal Rubidium has a relatively low ionization potential of 4.177 eV and can be ionized by simultaneous absorption of two photons from the visible spectral range [86]. Compared to single-photon transition two-photon absorption offers additional control over the ionization process, especially when two different colors are used. A number of studies on two-photon ionization of ultracold ^{87}Rb can be found in the literature [49, 50, 87, 88]. In some of those

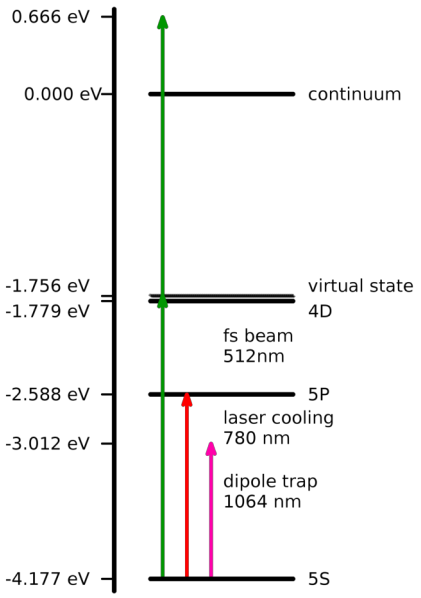

Figure 3.1.: Energy levels of ^{87}Rb. The cooling transition (D2-line) is indicated in red. The trapping laser (magenta) is far red detuned with respect to the $5S_{1/2} \rightarrow 5P_{3/2}$ transition. Photoionization can be achieved with two green photons via a virtual intermediate state close to the 4D state.

experiments real intermediate states were used in order to ionize atoms in a very controlled manner. The mechanism used in this work is one-color, two-photon ionization. The situation is depicted in a simplified level schema in figure 3.1. It shows the relevant atomic levels between the $5S_{1/2}$ ground state and the ionization threshold together with the photon energies of the lasers in the experiment. Ionization takes place via a virtual state using the second harmonic of the femtosecond laser at $\lambda_{SH} = 511.4\,\text{nm}$. The close-by $4D$ state is resonant at 517 nm [50]. Hence it is outside the laser bandwidth of 1.7 nm and will not contribute to the ionization. However resonance enhancement by this state increases the ionization rate by several orders of magnitude. The photoelectrons created by the pulsed laser get a kinetic energy of $E_{kin} = 0.666\,\text{eV}$.

3.1.1. Ionization Regimes

The notion of simultaneous absorption of multiple photons is however a perturbative picture. It assumes that the electrical field of the light pulse is weak compared to the Coulomb field of the

ionic core and that the quantum numbers of the free atom remain valid during the interaction. However ultrashort laser pulses can exhibit large electrical field components that violate this assumption. When the field of the light pulse becomes comparable to the field of the nucleus it alters the electronic state significantly and new ionization processes become possible.

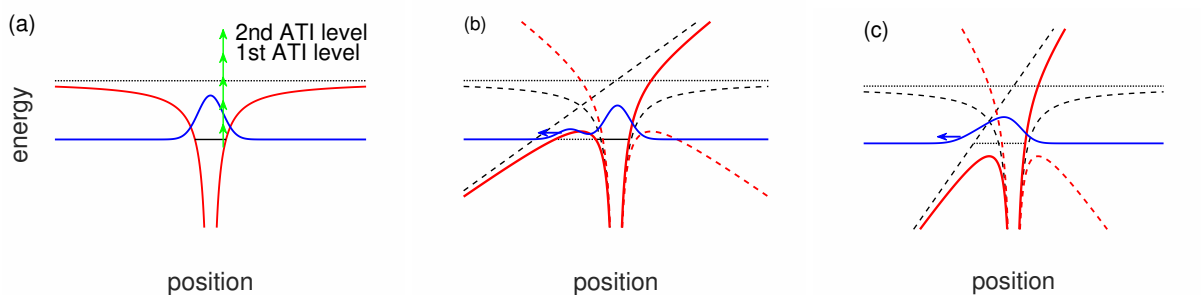

Figure 3.2.: Possible ionization processes. Multiphoton ionization (a), tunneling ionization (b), barrier suppression ionization (c). The Coulomb potential of the nucleus (red) that confines the valence electron (blue) is distorted by the electrical field of the laser. The laser intensity increases from left to right. After half an optical period the laser field changed sign and the potential is mirrored (red dashed line).

Figure 3.2 shows how the Coulomb potential is distorted in the presence of a strong (oscillating) field. The field adds a linear contribution to the potential that becomes more and more relevant with increasing intensity. During half an oscillation of the light field the slope of this contribution changes its sign. In figure 3.2 (a) the intensity is low and the perturbative *multiphoton ionization* (MPI) model holds. The bound electron state is confined in the potential of the atom core and can only escape by absorbing multiple photons simultaneously. The electron can even absorb more light quanta than the minimum needed for the transition into the continuum. This case is called *above threshold ionization* (ATI) and the photoelectrons acquire additional kinetic energy of $N\hbar\vec{k}$, with N denoting the number of additionally absorbed photons.

At higher intensities the distortion of the potential due to the laser becomes comparable to the ionization energy (see figure 3.2 (b)). The wave function of the valence electron couples to a free state through the remaining potential barrier. This process is called *tunneling ionization*. Eventually the barrier can be pushed below the energy level of the bound state (see figure 3.2 (c)) rendering the electron a free particle, so-called *over-the-barrier ionization* (OBI). Tunneling ionization as well as OBI cannot be described using perturbative approaches.

The critical intensity for the onset of over-the-barrier ionization I_{OBI} can be calculated by equating the binding energy of the electron in the unperturbed atom with the potential maximum that is introduced by the laser [51]:

$$I_{OBI} = \frac{\pi^2 c \epsilon_0^3 U_i^4}{2Z^2 e^6} = 1.218 \times 10^{12}\,\mathrm{W\,cm^{-2}} \tag{3.1}$$

In this expression U_i denotes the ionization potential of the atom under investigation with a charge $Z \times e$. The constants c, ϵ_0 and e are the speed of light, the vacuum permittivity and the elementary charge. In figure 3.2 the critical intensity is exceeded between (b) and (c). Above I_{OBI} the electron is no longer bound and the ionization probability is close to unity.

Ionization probabilities can be calculated for all of the mentioned intensity regimes. A detailed description of the models follows in the course of this section. At first it is necessary to decide which of those models is appropriate for a given laser intensity. This can be done by calculating the *adiabaticity parameter* or *Keldysh parameter*.

3.1.2. Adiabaticity Parameter

The oscillating electric field of a laser drives the valence electrons in an atom. They perform a quiver motion with the frequency of the field. The kinetic energy is given by the ponderomotive potential [51]:

$$U_p = \frac{e^2 \mathcal{E}_{SH}^2}{4 m_e \omega_{SH}^2} = \frac{e^2 I_L}{2 m_e c \epsilon_0 \omega_{SH}^2} \tag{3.2}$$

where m_e is the mass of the electron, $\mathcal{E}_{SH}$ is the field strength and ω_{SH} is the angular frequency of the laser. The Keldysh parameter γ compares the ponderomotive potential U_p to the ionization potential U_i and gives a good estimate on the validity of the perturbative description. It is defined as [89]:

$$\gamma^2 = \frac{m_e}{e^2} \times \frac{2\omega_{SH}^2 U_i}{\mathcal{E}_{SH}^2} = \frac{U_i}{2U_p} \tag{3.3}$$

Here I_L is the intensity of the light field. For $\gamma > 1$ the ionization process can be treated with MPI theory (see section 3.1.3). In situations where $\gamma < 1$ a tunneling ionization description (see section 3.1.4) will lead to more realistic results up to the point where the field is strong enough to free bound electron state by suppression of the tunneling barrier.

In atomic physics noble gases are widely used model systems. Due to their closed electron shells they have the highest ionization potentials and their adiabaticity parameter γ approaches unity for intensities on the order of $1 \times 10^{14}\,\mathrm{W\,cm^{-2}}$. On the contrary alkali atoms with their single valence electron, have relatively low ionization potentials and thus considerably less intensity is needed to reach $\gamma = 1$.

Figure 3.3 compares the Keldysh parameters for Rubidium and Krypton ($U_i = 14\,\mathrm{eV}$), which is the noble gas closest to Rubidium. The crossover from MPI to tunneling ionization is indicated by the intersection of the Keldysh parameter with the horizontal line $\gamma = 1$. The intensity at this intersection is about $3.5 \times 10^{13}\,\mathrm{W\,cm^{-2}}$ for Rubidium and $1.2 \times 10^{14}\,\mathrm{W\,cm^{-2}}$ for Krypton. More importantly the over-the-barrier ionization threshold, indicated by the vertical line, is shifted two orders of magnitude for Rubidium. So alkali atoms are much more susceptible to strong field ionization mechanisms than rare gas atoms. Because the OBI threshold occurs where $\gamma > 1$ one

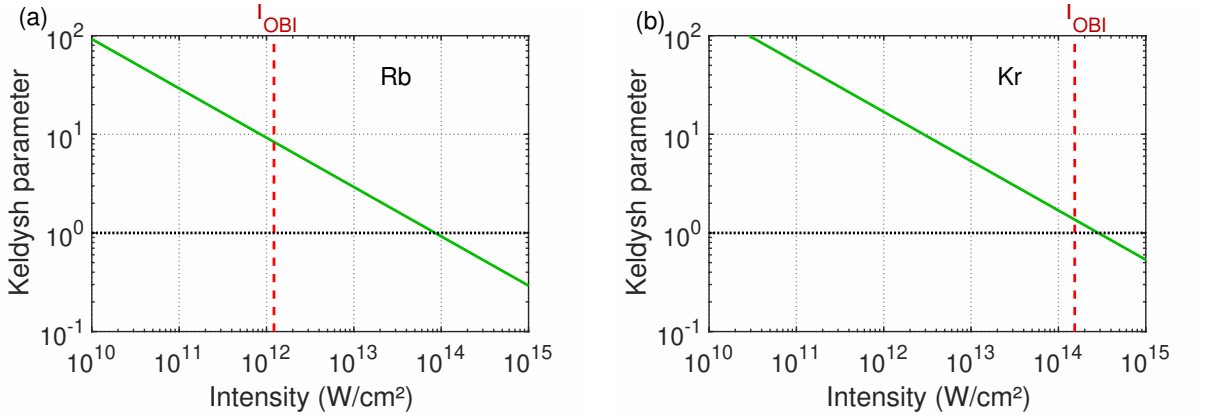

Figure 3.3.: Keldysh parameter γ for Rubidium (a) and Krypton (b) for the femtosecond laser at 511.4 nm. The vertical dashed line represents the critical intensity I_{OBI}. The intersection between the Keldysh parameter and the horizontal line at $\gamma = 1$ marks the onset of tunneling ionization.

can anticipate that tunneling plays a minor role for the ionization probability of Rubidium. This has also been reported for Lithium, which is also an alkali atom [90].

3.1.3. Multiphoton Ionization

For low intensities ($\gamma \gg 1$) a perturbative description can be used for the ionization process (see figure 3.2 (a)). For one photon, the transition rate $\Gamma_{i,f}$ from one eigenstate $|i\rangle$ to another $|f\rangle$ is according to Fermi's Golden rule proportional to the squared matrix element of the dipole operator $\hat{D} = -q \times \vec{r}\vec{\mathcal{E}}(t)$:

$$\Gamma_{i,f} \propto |\langle f|\hat{D}|i\rangle|^2$$

As the transition is driven by the dipole operator $\hat{D}$ one can immediately see that the transition rate is proportional to the squared electrical field $\mathcal{E}^2$. So it is proportional to its intensity I_L. If a second photon is involved the expression above has to be extended with a sum over all intermediate eigenstates $|k\rangle$:

$$\Gamma_{i,f,2} \propto |\sum_k \langle f|\hat{D}|k\rangle\langle k|\hat{D}|i\rangle|^2.$$

For higher order processes more intermediate states have to be introduced. The ab-initio calculation of multiphoton ionization rates of course is rather complex. But from this consideration it is already clear that the multiphoton ionization rate is proportional to the intensity of the laser to the power of the number of photons: $\Gamma_m \propto I_{SH}^m$. The factor between both quantities is called generalized multiphoton ionization cross section σ_m [91]. Hence the expression can be re-written as:

$$\Gamma_m = \sigma_m \times \Phi^m(\vec{r}, t) \tag{3.4}$$

where $\Phi_m = I_{SH}/h\nu_{SH}$ is the photon flux. For Rubidium two-photon ionization cross sections have been measured in the spectral range between 425 nm and 590 nm [50]. For the wavelength of 511.4 nm used in the experiment it is $\sigma_2 = 1.47 \times 10^{-49}\,\mathrm{cm}^4\,\mathrm{s}$. From the multiphoton ionization rate on can infer the ionization probability (see section 3.1.5).

3.1.4. Tunneling Ionization and Barrier Suppression Ionization

For low Keldysh parameters ($\gamma < 1$) ionization can occur by tunneling through the potential barrier (see figure 3.2 (b)). In this case the ionization rate equals the tunneling rate. It can be calculated using a quasi-static approximation by solving the Schrödinger's equation for a static field $\mathcal{E}$ [92]. In the second step this field is replaced by $\mathcal{E} \times \cos(\omega t)$ and integrated over one period. In the calculation only the initial bound state and the final continuum state are relevant. An analytic expression to solve this problem can be found for the Hydrogen atom which was generalized for complex atoms by Ammosov, Delone and Krainov [93]. For an s-state interacting with linearly polarized light the ionization rate is [89]:

$$\Gamma_{ADK} = \sqrt{\frac{3}{8}} \left(\frac{e a_0}{\pi E_h} \frac{n^* \mathcal{E}_{SH}}{Z} \right)^{3/2} \frac{D^2}{Z} \exp\left(-\frac{2E_h}{3 e a_0} \frac{Z^3}{n^{*3} \mathcal{E}_{SH}} \right) \tag{3.5}$$

Here $\mathcal{E}_{SH}$ is the amplitude of the electrical field strength, $n^* = Z\sqrt{E_h/2U_i}$ is the effective principal quantum number and $D = (4E_h/a_0 \times Z^3/(n^* \mathcal{E}_{SH}))^{n^*}$. The Hartree energy E_h and the Bohr radius a_0 appear due to the conversion from atomic units to SI units. The model is valid when the tunneling time is shorter than the oscillation period of the light field. Additionally the model is restricted to situations where the photon energy is lower than the ionization potential ($\hbar\omega_{SH} \ll I_P$) and where the Coulomb field of the atom $\mathcal{E}_{atom}$ still dominates over the AC electric field $\mathcal{E}_{SH} \ll \mathcal{E}_{atom}$.

Close to the critical intensity I_{OBI} when the ionization barrier is suppressed (see figure 3.2 (c)) tunneling may still occur in the temporal wings of the pulse. The ADK model overestimates ionization rates because the tunneling rate was derived using perturbation theory and the atomic energy level is now below the potential barrier. So the perturbative approach fails with an exponentially increasing error which can be compensated with an empirical extension of the ADK formula [94]:

$$\Gamma_{TBI} = \Gamma_{ADK} \times \exp\left(-\alpha \frac{e a_0 E_h^{3/2}}{2\sqrt{2}} \frac{Z^2 \mathcal{E}_{SH}}{U_i^{5/2}} \right) \tag{3.6}$$

For Rubidium the correction factor was found to be $\alpha = 6.0$. ADK and tunneling-barrier-suppression ionization (TBI) are widely used models especially for their simplicity. Of course more complex studies can be found in the literature that solve the Schrödinger equation numerically using a single active electron Ansatz. Among others, Delone and Krainov published a

competing expression for the barrier-suppression ionization rate [89]. In addition ionization rates for alkali metal atoms in strong light fields have been calculated numerically recently [95].

3.1.5. Ionization Probabilities

The ionization probability P can be obtained by solving the differential equation:

$$\frac{dP(t)}{dt} = (1 - P(t)) \times \Gamma_{ion} \tag{3.7}$$

which can be transformed into:

$$P = 1 - \exp\left(\int_{-\infty}^{\infty} \Gamma_{ion} dt'\right) \tag{3.8}$$

and solved by integrating over one pulse. The ionization probability was calculated for the multiphoton model (3.4) as well as for the tunneling models (3.5), (3.6) by inserting the rates Γ_{ion} in equation (3.8). Figure 3.4 shows the probability for an atom to be ionized after one pulse versus the peak intensity of the ionizing beam for a pulse duration $\tau = 220\,\text{fs}$.

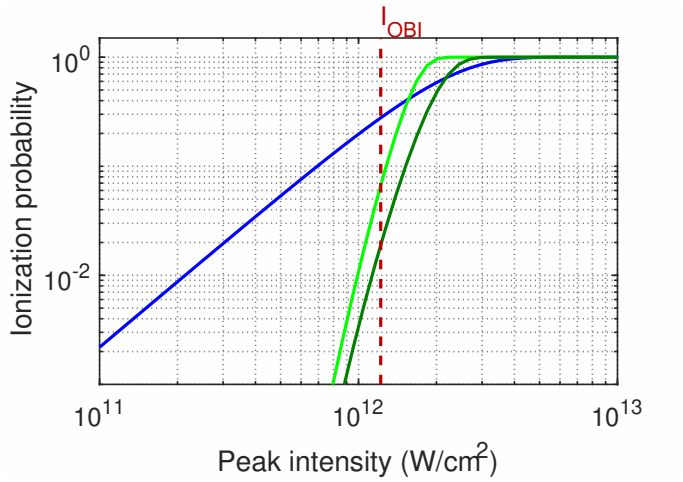

Figure 3.4.: Photoionization probabilities for Rubidium with one pulse. In blue the two-photon probability; in light and dark green the ADK tunneling probability and TBI probability respectively. The curves were calculated for a pulse duration of 220 fs. The dashed line indicates the critical intensity for over-the-barrier ionization (I_{OBI}).

In the low intensity regime, where $\gamma \gg 1$ the MPI probability increases with a slope of 2 as it is proportional to peak intensity squared I_0^2 and saturates at $P = 1$ when the adiabaticity parameter approaches 1.

The tunneling and tunneling-barrier ionization probabilities rise quickly while crossing the critical intensity $I_{OBI} = 1.218 \times 10^{12}\,\text{W cm}^{-2}$. They are always considerably smaller than MPI probability – even at the critical intensity. Therefore MPI should be a good model for

the experiments discussed in this work up to the critical intensity I_{OBI} where the ionization probability is $P = 1$.

The production of higher charge states is not relevant in this work as the photon energy as well as the peak intensity are not high enough. Due to the high ionization potential of double-ionized Rubidium ($U_{i2^+} = 27.290\,\mathrm{eV}$) it is rather unlikely to be formed. A singly charged ion would need to absorb 11 additional photons simultaneously to undergo multiphoton ionization. In addition one can estimate from the adiabaticity parameter γ that tunneling ionization of Rb^+ should occur at intensities as high as $5 \times 10^{14}\,\mathrm{W\,cm^{-2}}$.

3.1.6. Experimental Results

The fraction of atoms that is lost due to the ionization by the laser pulses gives experimental access to the photoionization probability. Special care was taken to create samples that were not optically dense to allow accurate particle number measurements. The absorption images were analyzed directly with 1D and 2D fits (see figure 2.11) in order to determine the atomic losses. The fit function used is a sum of two Gaussians. One describing the shape of the ensemble of atoms; one modeling the dip in the center of the density distribution. In contrast Alexander Grote presented a different analysis scheme for similar measurements in his PhD thesis [96]. There an image of an unimpaired atomic cloud was subtracted from the data before applying a fit routine. The loss fraction is given by the ratio of the volume of the density dip and the total volume of the atomic cloud. Figure 3.5 shows the losses after a single pulse for intensities ranging from $8 \times 10^{11}\,\mathrm{W\,cm^{-2}}$ to $1.2 \times 10^{13}\,\mathrm{W\,cm^{-2}}$ for a cloud of thermal atoms in the optical dipole trap. Two different measurements are presented. On the left the laser pulse was applied in situ and the evaluation was done with 1D fits to the column sum of the absorption images. The right plot features a measurement where the atoms were released from the trap and illuminated with a laser pulse after 3 ms time of flight. Thus the atom density was reduced allowing more accurate measurements of the density variations in the center of the cloud. For the evaluation of this measurement 2D fits were more robust.

The expected loss fraction N_{loss}/N_0 is inferred from the ionization probability P and the atom density ρ:

$$\frac{N_{loss}}{N_0} = \frac{1}{N_0} \int_V \rho(x, y, z) \times (1 - P(x, y, z))$$

Depending on the local peak intensity $I_0(x, y, z)$ at each point in the beam profile the appropriate photoionization model is chosen. Below the critical intensity I_{OBI} the multiphoton model is used, above it the probability is assumed to be $P = 1$. Like the multiphoton ionization probability the loss fraction increases with a constant slope for low intensities. Close to the critical intensity the probability jumps to 1 and the slope of the loss fraction suddenly increases. As the interaction volume is depleted the loss fraction saturates. The remaining slope at high intensities is due to

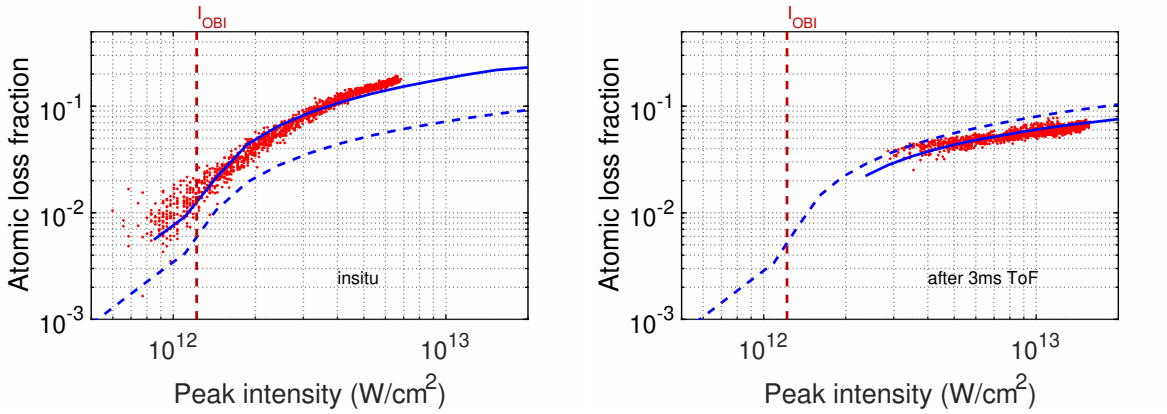

Figure 3.5.: Atomic loss fraction from the optical dipole trap due to photoionization with one pulse. The measured loss fraction for thermal clouds of atoms (dots) is shown as well as the theory curve (dashed line). To compare the theory to the experimental data simulated density distributions were analyzed in the same way as the measured data (solid blue line).

additional ionization in the wings of the beam profile. Indeed, as the wings reach out more and more the total ionization volume increases.

It was noticed that the Gaussian model for the fit did not reproduce the shape of the density distribution accurately enough; especially where the gradient is high. A simulated absorption image for atoms in the dipole trap is shown in the left panel of figure 3.6. On the right hand side of the same figure the column sum of this distribution is shown together with a 1D fit that is also used for the analysis of measured data. The fit deviates from the shape of the column sum at the two maximums and the minimum in the center of the distribution. Applying the analysis routine

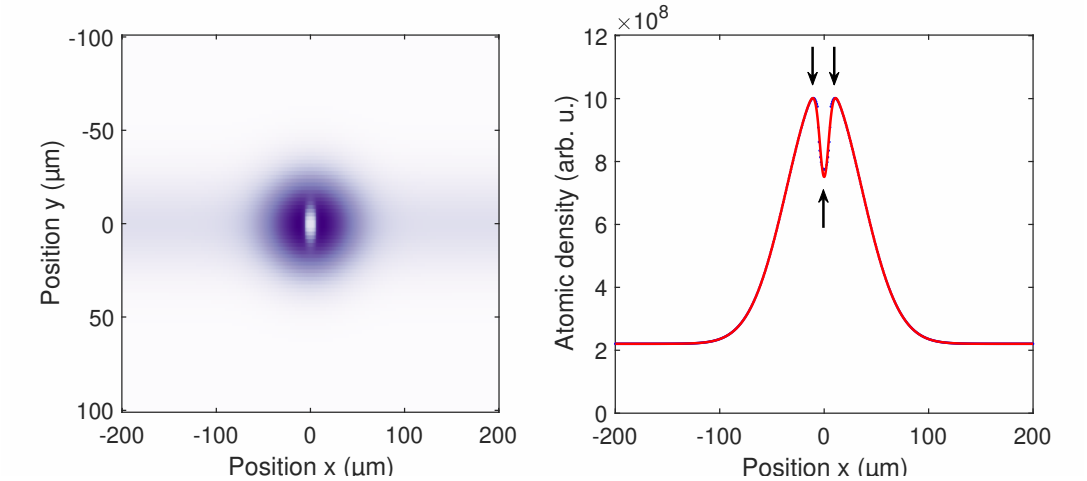

Figure 3.6.: Simulated density distribution for atoms in the optical dipole trap (left panel) and fit to its column sum (right panel). The fit function deviates in the center of the distribution.

to simulated data shifts expected the loss fraction to larger values and so the measurement is in good agreement with the theory.

The theoretical loss fraction is determined by the peak intensity that is experimentally given

by the pulse duration and the beam waist. The best agreement between the measured data and the theory was achieved for a waist of 13 µm and pulse duration of 220 fs.

While the beam waist $w_{SH} = (12.5 \pm 0.8)$ µm was measured with a camera, it was not possible to determine the pulse duration directly (see section 2.2.1). Advanced beam diagnostics such as an autocorrelation setup were not at hand. Though the minimum pulse duration can be estimated by assuming an un-chirped pulse with a Gaussian shape from the time-bandwidth product $\Delta\tau \times \Delta\nu = 0.441$ [97]. For the measured spectral width of 1.7 nm the pulse duration is $\tau = 202$ fs. The beam parameters inferred from the photoionization measurement are consistent with the measured waist and the estimated pulse duration.

In smaller clouds it is possible to measure the loss fraction directly from the atom number. Figure 3.7 shows two of such measurements. An optically confined ensemble of ultracold atoms was illuminated with a pulse train at a repetition rate of 0.5 kHz. The absorption images were taken after variable hold times. Each additional laser pulse gives rise to measurable atom losses. The stepwise decrease of atom number results from complete ionization in the interaction volume with subsequent redistribution of atoms in the trap. The ratio of the first two steps in the plot

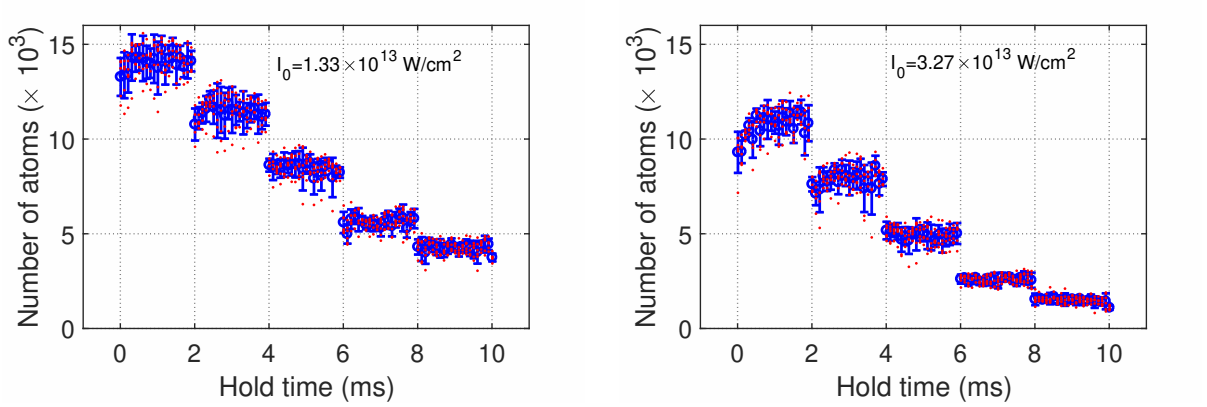

Figure 3.7.: Direct observation of atom losses due to photoionization. A laser pulse with a peak intensity I_0 is applied every 2 ms leading to a stepwise decrease of atom number. Dots representing individual shots are shown together with their averages and statistical errors.

gives a loss fraction of about (23 ± 10) % for an intensity of 1.33×10^{13} W cm^{-1} (left plot) and about (33 ± 12) % for an intensity of 3.27×10^{13} W cm^{-1}. Both numbers are in good agreement with the prediction from the simulation. The ionization probability for those intensities is close to unity as it is already above the over-the-barrier limit (see Figure 3.4).

3.1.7. Summary

Investigations on the photoionization of ultracold atoms in strong laser fields were presented. The loss fraction can be calculated from the atomic density and the ionization probability without free parameters. The atom loss fraction was measured for thermal atoms in the optical dipole

trap and are is well described by our theoretical model. For Bose-condensed clouds it was not possible to measure the loss fraction because the optical densities are too high to obtain accurate density profiles from absorption imaging.

It was also shown that the loss fraction can be measured directly by counting the total number of atoms. However this approach works for small total particle numbers only. In order to extent the measurement to the low intensity regime where only MPI is expected more detection sensitivity is needed. This will be improved by installing detectors for direct measurement of single photoelectrons and ions, e.g. microchannel plates. In the future setup these detectors will be available allowing further investigations.

3.2. Transient Optical Dipole Force

Besides ionizing atoms the ultrashort pulses also imprint momentum on the atomic density distribution. This can be observed in time of flight as it leads to an additional radial velocity component inducing a ring-like density distribution. Figure 3.8 shows the evolution of a BEC in time of flight after the interaction with a single pulse.

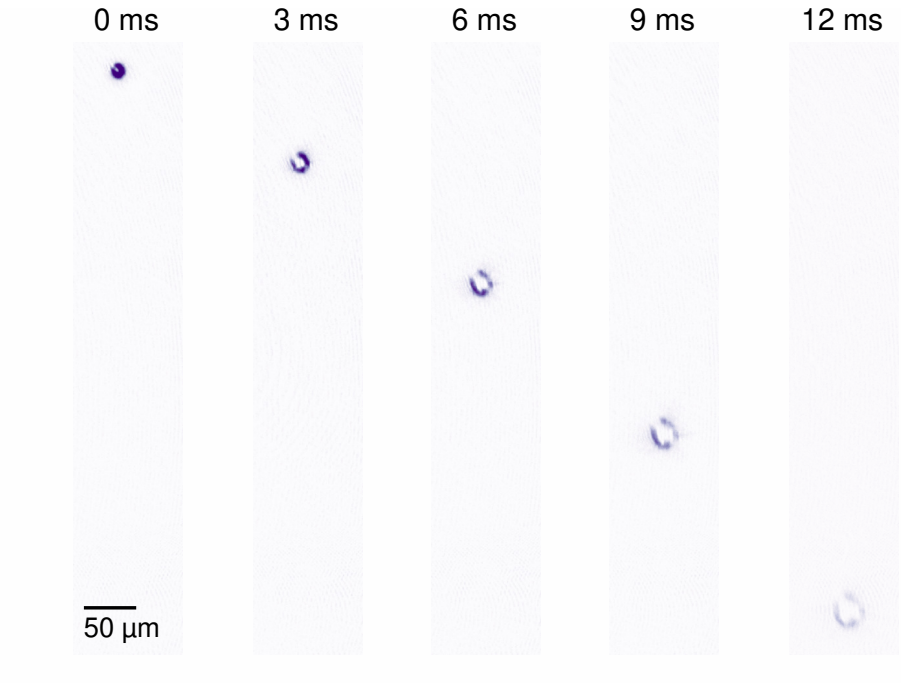

Figure 3.8.: Expansion of a BEC after interaction with a single femtosecond laser pulse at a peak intensity of $I_0 = 9.7 \times 10^{12}\,\mathrm{W\,cm^{-2}}$. To reduce the optical density the cloud was released from the optical dipole trap and expanded for 8 ms before the pulse is applied.

The intensity gradient in the beam profile gives rise to an optical dipole potential $U_{dip}(\vec{r}, t) = C \times I(\vec{r}, t)$ defined in equation (2.4). As the femtosecond laser is far blue-detuned with respect to the D-lines of ^{87}Rb, the interaction is repulsive. The atoms are therefore pushed out of the focal region. Integration of the potential gradient over time yields the momentum imprinted on the atoms:

$$\vec{p}(\vec{r}) = \int_{-\infty}^{\infty} -\nabla U_{dip}(\vec{r}, t)dt \tag{3.9}$$

Assuming a Gaussian beam profile the transferred momentum takes the form:

$$\vec{p} = I_0 \times \vec{r} \times 4\sqrt{2\pi}C\tau/\omega_{SH}^2 \exp(2r^2/w_{SH}^2) \tag{3.10}$$

The magnitude of the momentum is proportional to the peak intensity I_0. Its spatial distribution is determined by the beam waist w_L. This model is valid in the low intensity regime where $\gamma \gg 1$, otherwise the atoms would be ionized in the strong field with high probability. In

addition the dressed atom picture can be used as the 220 fs pulses support over 100 oscillations [98].

3.2.1. Numerical Simulation

The evolution of the density distribution can be evaluated by calculating the displacement for each point in density distribution. It can be derived numerically from the velocity field $v(\vec{r}) = p(\vec{r})/m_{Rb}$. For the simple case of a single pulse the displacement after time t is given by $r' = r + v(r) \times t$. Figure 3.9 illustrates the idea of the simulation. The columns in the discretized density are redistributed according to the acquired momentum. It depends only on the initial position of each column if a single pulse is applied. The model of optical dipole force

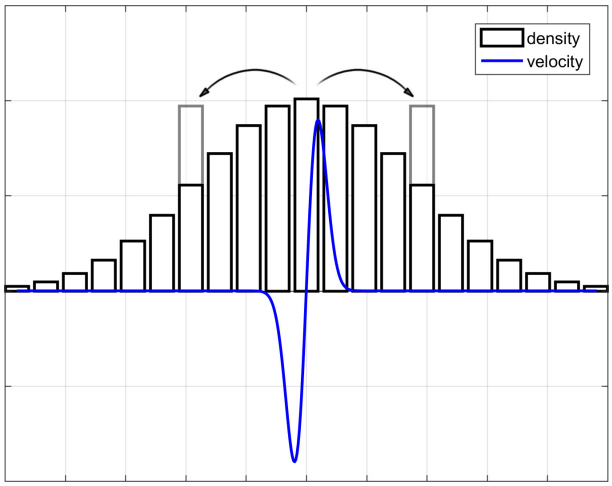

Figure 3.9.: Numerical model. The discretized atom density (black bars) is redistributed according to the displacements calculated from the velocity field (blue solid line).

breaks down for intensities above the critical intensity for over-the-barrier ionization I_{OBI}. The simulation assumes therefore that all atoms that experience an intensity that exceeds the critical one are ionized and do not contribute to the signal.

If the atoms are illuminated with multiple pulses at a repetition rate f_{rep} the simulation becomes more complicated. After each pulse the atoms move for $1/f_{rep} = 10\,\mu s$. The process repeats until the atoms have left the interaction volume or the pulse train ends. Now the final velocity for each point in the density distribution is given by the sum over all kicks. The calculation is done with a Matlab script that iterates over all points of the density and the number of pulses. A 1D description is sufficient because the cloud and the focus are nearly circular symmetric and their centers coincide.

3.2.2. Experimental Results

The experimental investigations on the transient optical dipole force are based on time-of-flight series as depicted in figure 3.8. Bose-condensed atoms are released from the trap and illuminated with the laser. The initial time of flight of 8 ms allows reducing the optical density of the cloud. Then a femtosecond laser pulse is applied and the expansion is studied by varying the delay between femtosecond pulse and absorption imaging.

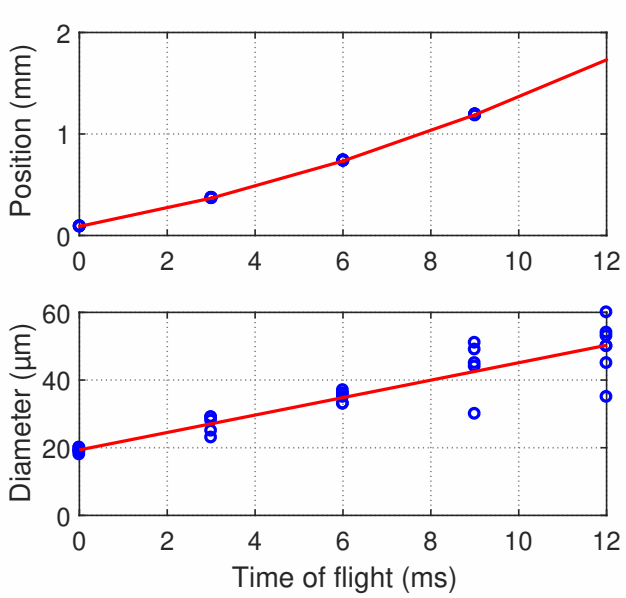

Figure 3.10.: Center of mass position (upper panel) and cloud diameter (lower panel) versus time of flight. The data is extracted from time of flight series as the one in figure 3.8. The solid lines are fits to the data. The center of mass motion is fitted with a second order polynomial as the atoms are accelerated wit g_0. The linear fit in the lower panel gives the expansion speed.

Figure 3.10 shows the position and the radius extracted from these images. In the upper panel the center-of-mass position is shown versus the time of flight. Due to gravity the atom experience constant acceleration $g_0 = 9.81\,\mathrm{m\,s^{-2}}$. In the lower panel of figure 3.10 the diameter of the ring is plotted versus the ToF and the expansion speed is extracted from this data by linear regression. For the analysis of the complete data set a computer program was implemented to determine the radii in each image. The algorithm fails for long time-of-flight as the atom density spreads over a large volume and the signal-to-noise ratio becomes low. The expansion speed has been determined for different laser intensities and the result are depicted in figure 3.11. Additionally the plot features the numerical simulation and a linear fit to the simulated data. The large error originates in the automated determination of radii. The experiment gives a slope of $(6.9 \pm 2.0) \times 10^{-13}$ (mm/s) /(W/cm^2). This value is in good agreement with the simulated slope of 6.7×10^{-13} (mm/s) /(W/cm^2). The ballistic expansion of the BEC after releasing it from the trap adds an offset of $v = (1.9 \pm 0.2)\,\mathrm{mm\,s^{-1}}$ to the measured velocities.

A reference measurement without femtosecond laser pulses confirmed the expansion velocity $v_0 = (1.5 \pm 0.3)\,\mathrm{mm\,s^{-1}}$. The values are compatible with the expansion speed of an ideal BEC [23]

$$v_{ideal} = \sqrt{\hbar\omega_{dt}/m_{Rb}} \times 2\sqrt{2\ln 2} = 1.6\,\mathrm{mm\,s^{-1}}.$$

As the simulation does not account for the ballistic expansion of the BEC the curve was shifted by v_{ideal}.

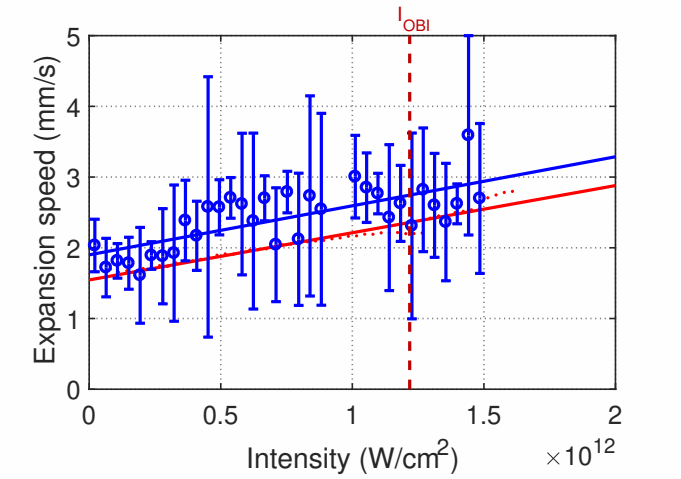

Figure 3.11.: Expansion speed after interaction with a single laser pulse. The linear fit to the measured data (blue) agrees with the result of the simulation (red). The natural expansion speed v_{ideal} was added to the simulation as it was neglected in the model.

In a second series of measurements the average power of the ionizing beam was fixed at $P_{avg} = 14.4\,\mathrm{mW}$ at $f_{rep} = 100\,\mathrm{kHz}$ and the number of pulses was scanned. This corresponds to a peak intensity $I_0 = 2.72 \times 10^{11}\,\mathrm{W\,cm^{-2}}$. Of course it was necessary to keep the dipole trap switched on during the pulse train. Figure 3.12 shows the measured expansion speed. As each of the pulses transfers momentum to the atoms in the interaction region, the expansion speed increases linearly with the pulse number. After about 80 pulses the expansion speed saturates as the focus region is empty before the pulse train ends. The slope of the fit to the linear part in the data is $(0.222 \pm 0.014)\,\mathrm{mm\,s^{-1}}$ per pulse. It is again in agreement with the simulated value of $(0.243 \pm 0.002)\,\mathrm{mm\,s^{-1}}$ per pulse. The simulation shows systematically lower velocities. The mean difference between the simulation and the data is $(1.6 \pm 0.8)\,\mathrm{mm\,s^{-1}}$.

The best agreement between measurement and simulation was achieved with the waist $w = 13\,\mu\mathrm{m}$ and the pulse duration $\tau_{FWHM} = 220\,\mathrm{fs}$. These parameters are consistent with section 3.1.

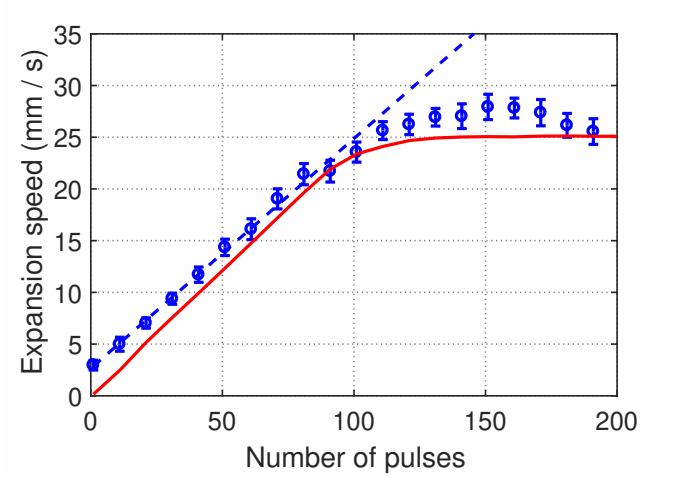

Figure 3.12.: Expansion speed for various pulse numbers at fixed intensity $I_0 = 2.72 \times 10^{11}\,\mathrm{W\,cm^{-2}}$. At low pulse numbers the measured velocity (circles) increases linearly. It saturates for longer pulse trains as the atoms leave the interaction region before the pulse train has ended. The data is compared to the simulation (red line). The dashed line is a linear fit to the first 10 data points.

3.2.3. Summary

The transverse intensity profile of the femtosecond laser pulses imprint momentum on the atoms in radial direction. This effect is expected from the optical dipole force which the laser exerts on the atoms. The momentum transfer is based on a deterministic model opposed to the probabilistic nature of photoionization and all atoms in the focus are affected. Although both mechanism occur in the presence of the femtosecond pulse it takes a few milliseconds for the momentum transfer to become visible since the induced velocity is relatively low. It is comparable to the natural expansion speed of a BEC and is therefore not relevant for the ionization measurements in section 3.1 as the absorption imaging is done directly after the ionization pulse.

The momentum transfer has been calculated by integrating the transient optical potential over the pulse duration (equation (3.10)). The measured expansion speeds are in good agreement with the numerical simulation. The transient optical dipole force exerted mode-locked lasers can be used to trap ultracold gases. So far it has been implemented using picosecond pulses [99, 100]. An optical trap using femtosecond pulses has been suggested and simulated [98].

3.3. Relaxation

As discussed in section 3.1 trains of femtosecond laser pulses interacting with the cold atoms create ions and cause a density reduction in the focus region. The ions are lost from the magnetic trap and a dip becomes clearly visible in the density profile. Figure 3.13 shows a series of images for different delays between the ionizing laser pulses and imaging pulse. It displays the optical density on the left and its column sum on the right. To achieve a good contrast, 12 pulses with a wavelength of $\lambda_{SH} = 511.4\,\text{nm}$ and peak intensity of $5.66 \times 10^{13}\,\text{W cm}^{-2}$ were applied. The pulse repetition rate was set to $f_{rep} = 98.522\,\text{kHz}$.[1]

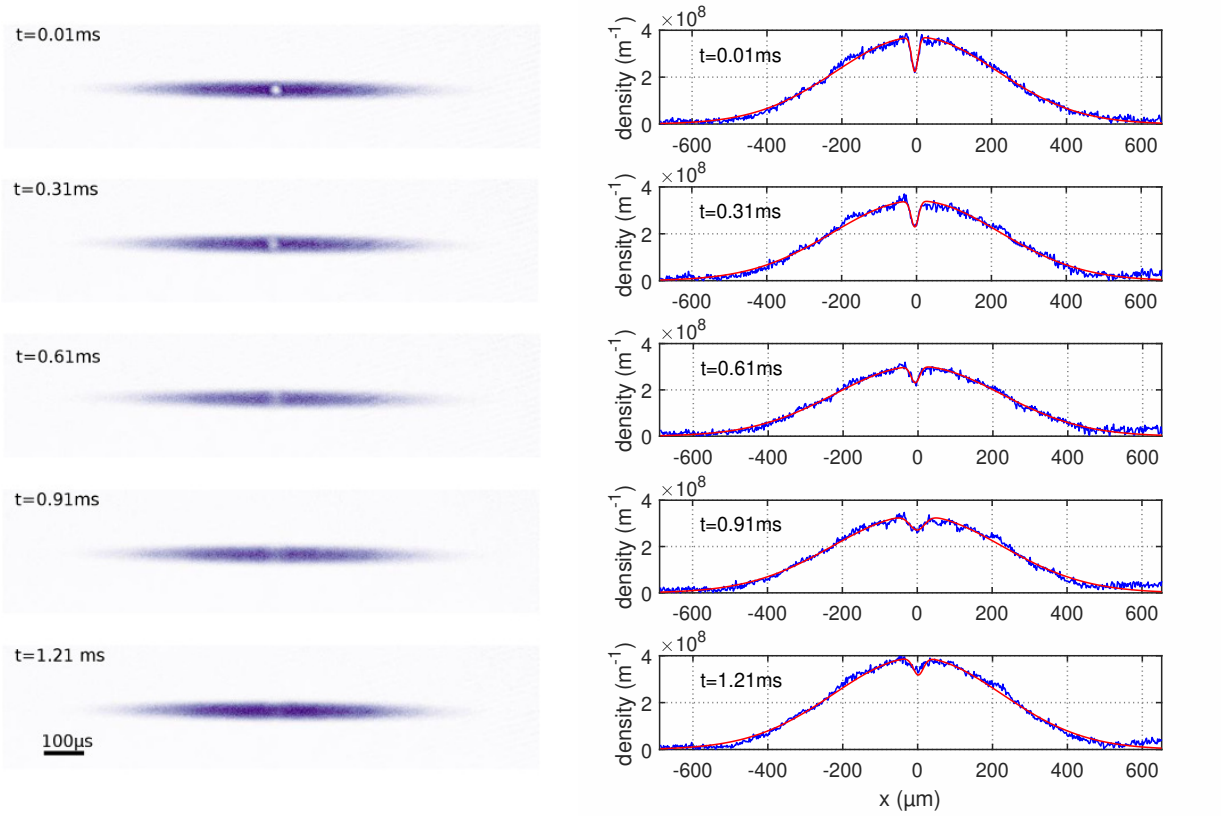

Figure 3.13.: Time evolution of the in-situ density in the after interaction with 12 femtosecond laser pulses. The dip in the density resulting from photoionization vanishes in about 2 ms.

The ensemble of atoms in the trap is out of thermal equilibrium after the ionization. The density dip fills on a millisecond time scale as the atoms are redistributed within the trap. While vanishing the dip becomes broader and shallower. To analyze the evolution quantitatively the width and the amplitude of the void are extracted from the absorption images by performing double Gaussian fits.

[1] The repetition rate was kept well below the crystal resonances of the home-built pulse picker to achieve good extinction ratios after the pulse train. The commercial pulse picker was not installed at the time.

The time evolution of a thermal gas is described by the Boltzmann equation (3.11):

$$\left(\frac{\partial}{\partial t} + \frac{\vec{p}}{m_{Rb}} \times \frac{\partial}{\partial \vec{x}} + \vec{F} \times \frac{\partial}{\partial \vec{p}}\right) f(\vec{x}, \vec{p}, t) = \left(\frac{\partial f}{\partial t}\right)_{coll} \tag{3.11}$$

It describes the evolution of the phase space density f. On the left hand side the second and third term describe the contribution of the kinetic and potential energy respectively. The collision term on the right hand side accounts for atom-atom interactions, assuming an ideal gas it is set to zero.

In the experiment the cloud is confined in the magnetic trap and is therefore very elongated. Because the density dip has the size of the cloud's width the atoms are transported into the void only along the axial direction. Hence a 1D description of the problem is sufficient. The equilibrium phase space density for the case of a 1D harmonic trapping potential $V = m_{Rb}\omega_{mt}^2/2x^2$ can be written as:

$$f = N \times \frac{\omega_{mt}}{2\pi k_B T} \times \exp\left(-\frac{p^2}{2m_{Rb}k_B T}\right) \exp\left(-\frac{m_{Rb}\omega_{mt}^2 x^2}{2k_B T}\right) \tag{3.12}$$

The only free parameter in the expression is the temperature T of the cloud. The angular trap frequency is fixed by the magnetic trap $\omega_{mt} = 2\pi \times 27\,\mathrm{Hz}$; k_B is the Boltzmann constant. The total number of particles is written as N and is only a global scaling of the amplitude of the distribution. The simulations starts from an initial distribution that is created by multiplying the equilibrium state (3.12) with $(1 - A) \times e^{-x^2/(2w_{SH})}$. The initial width of the void is given by the beam waist w_{SH}. With this new phase space density the time evolution governed by the Boltzmann equation (3.11) is carried out numerically. The time integration is implemented in Matlab using the classical Runge-Kutta algorithm (RK4). The quantities in the equation were rescaled to dimensionless units. The variables were replaced by:

$$x \to \frac{1}{\omega_{mt}}\sqrt{\frac{2k_B T}{m_{Rb}}} \times x, \quad p \to \sqrt{2m_{Rb}k_B T} \times p, \quad t \to \frac{1}{\omega_{mt}} \times t \tag{3.13}$$

Figure 3.14 compares the measurement to the results from the numerical simulation. The upper panel shows the evolution of the width of density dip. The lower panel shows its amplitude. After about 2 ms the void has almost vanished and the fits start to become unreliable. The agreement between the simulated and the measured radii is good. However the measured amplitude decreases significantly faster than the expected trend. Additionally the final level is factor 2 lower. The deviation for the amplitude indicates that the model can still be improved. However, as the model has only one free parameter – the temperature T – and as it models the time scale correctly the overall agreement between measurement and simulation is satisfactory. The temperature extracted from the simulation is $\mathrm{T} = 6.8\,\mu\mathrm{K}$. Including the radial motion of

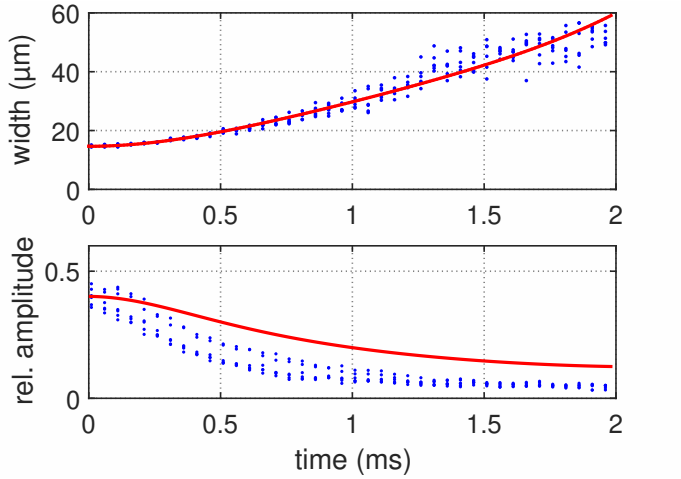

Figure 3.14.: Relaxation of the density dip. The evolution of its radius (upper graph) and its relative depth (lower graph) are shown. Measured data (circles) are compared to the numerical simulation (solid line).

the atoms and the transient optical dipole force would be good candidates for improving the description.

3.4. Atom-Ion Interaction

The phenomena discussed so far addressed the interaction between laser field and atoms as well as the relaxation of the atomic density. This chapter presents datasets indicating that atom-atom or atom-ion interactions have to be considered in the analysis.

Figure 3.15 shows a measurement similar to the relaxation studies discussed in section 3.3 but with atoms in the crossed optical dipole trap. The condensate fraction is 33 % and the peak density is $5 \times 10^{12}\,\mathrm{cm}^{-3}$. An intense laser pulse is applied every 2 ms. The beam was focused down to 8 µm and its peak intensity was clearly above the over-the-barrier ionization threshold. Directly after a pulse the atoms are not visible in the absorption image but they reappear within hundreds of microseconds. This behavior becomes even clearer in the time evolution of the

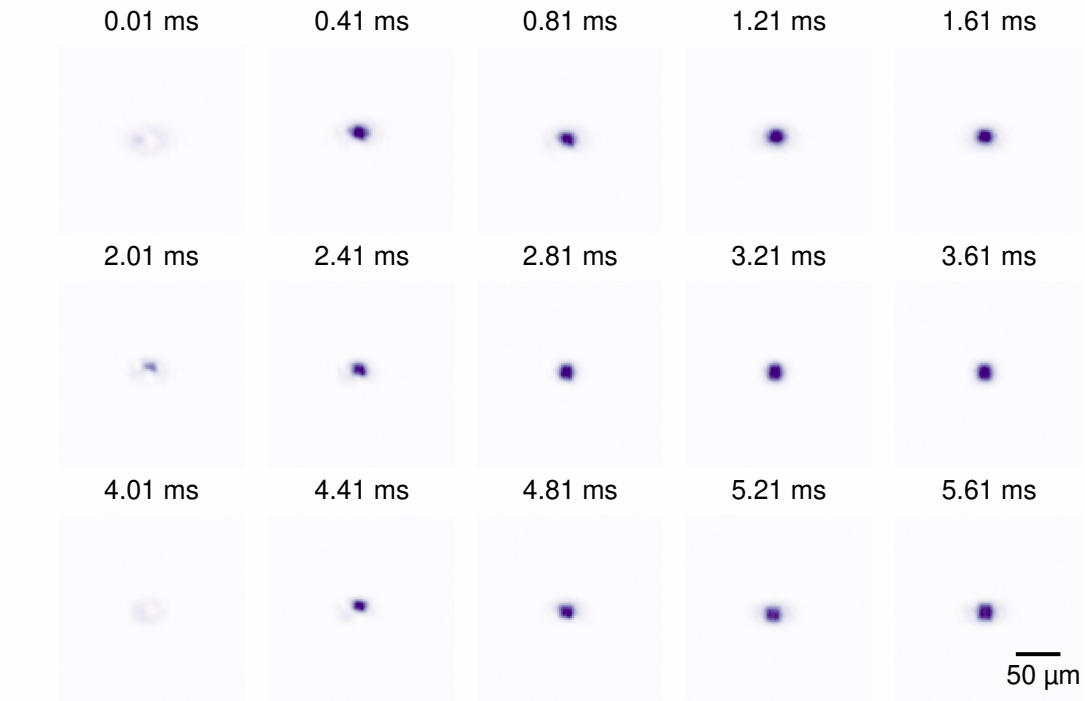

Figure 3.15.: Time evolution of the in-situ density. Atoms in the optical dipole trap are subject to an intense laser pulse every 2 ms. Initially the atoms are not visible but they re-appear on a time scale of 200 µs.

total atom number as plotted in figure 3.16. It recovers nearly completely to its initial value of 2.3×10^4 atoms; even after 10 consecutive pulses. To explain this measurement two questions must be answered: Why does the absorption signal decrease directly after the femtosecond pulse? And what determines the time scale for the atom number recovery? Absorption imaging is sensitive only to atoms in the $4p^6 5s_{1/2}$ state. Consequently the atoms either are not in the ground state or the resonance frequency for the transition to $4p^6 5P_{2/3}$ is shifted. The following sections present probable and exclude mechanisms explaining the observed behavior.

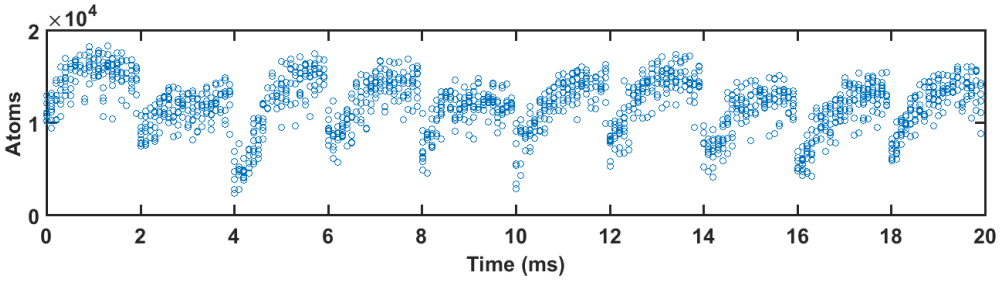

Figure 3.16.: Time evolution of the total number of atoms. After a pulse it drops to zero and recovers nearly to its initial value. Even after 10 pulses the atom loss is very small.

3.4.1. Optical Excitation of Dark States

During the measurement multiple laser beams are present. Besides the second harmonic of the femtosecond laser also residual light at the fundamental wavelength can reach the atoms. The level structure of ^{87}Rb does not provide transitions that can be driven by a single photon either from the second harmonic of the pulsed laser at $\lambda_{SH} = 511.4\,\text{nm}$, its fundamental at $\lambda_F = 1024\,\text{nm}$ or the trapping laser at $\lambda_{dip} = 1064\,\text{nm}$.

Although the $4p^6 4d_{1/2}$ state (see figure 3.1) seems to be close to resonance with a single photon from the second harmonic or with two fundamental photons, it cannot be excited. The second harmonic pulses exhibit a spectral bandwidth of $\Delta\lambda_{SH} = 1.7\,\text{nm}$ and thus the gap between the photon energy and the transition is more than seven bandwidths. This state has a lifetime of 81 ns [101]. Simultaneous absorption of one photon from the trapping beam and one from the second harmonic are detuned by more than four SH bandwidths from resonance with $4p^6 8s_{1/2}$ which has a lifetimes of 161 ns [101]. The excitation of one of those states is not probable due to the energy mismatch. Moreover these excited states would decay much faster than the observed time scale.

Long lifetimes on the order of tens or even hundreds of microseconds were observed for Rydberg states with high principal quantum numbers [102]. In other groups such states are excited through resonant two-color two-photon transitions from ultracold ^{87}Rb. Their lifetime depends significantly on the density of the surrounding atoms [88]. In this work direct optical excitation of Rydberg states is not possible with the available wavelengths but the lifetime of those states would match the observed time scale of 200 µs.

3.4.2. Ion-induced Stark Shift

The electrical field of the ions created by the laser pulse polarizes the surrounding atoms. This leads to a shift of the atomic energy levels, the so-called Stark shift. The electrical field can be strong enough to shift the atoms out of resonance with the imaging light. So they become transparent and are not visible in the absorption images. The strength of the Stark shift depends

on the polarizability of the considered states. For the imaging transition $5S_{1/2} \rightarrow 5P_{3/2}$ the additional energy splitting induced by an electrical field along the z-direction is given by:

$$\Delta W = -\frac{1}{2}\left(\alpha_0 + \frac{3J_z^2 - J(J+1)}{J(2J-1)}\alpha_2\right)\mathcal{E}^2 = -0.087\,\mathrm{Hz/(V/m)^2} \times \mathcal{E}^2 \tag{3.14}$$

The angular momentum quantum number $J = 3/2$ is given by the upper level of the transition. Its projection $J_z = 1/2$ is determined by the ground state because the π-polarized probe light preserves J_z in the transition. The D2 scalar polarizability $\alpha_0 = h{\times}0.1340\,\mathrm{Hz/(V/m)^2}$ and the D2 tensor polarizability $\alpha_2 = h \times -0.0406\,\mathrm{Hz/(V/m)^2}$ have been measured using laser spectroscopy [103].

The Stark shift induced by 500 ions is depicted in figure 3.17 together with the density distributions of atoms and ions. This amount of ions can be easily achieved by multiphoton ionization (see section 3.1). In order to calculate the Stark shift the ions are described as a continuous charge distribution. It is given from the convolution of the intensity profile of the ionizing beam with a waist of $w_L = 8\,\mu\mathrm{m}$ and the initial density of thermal and condensed atoms.

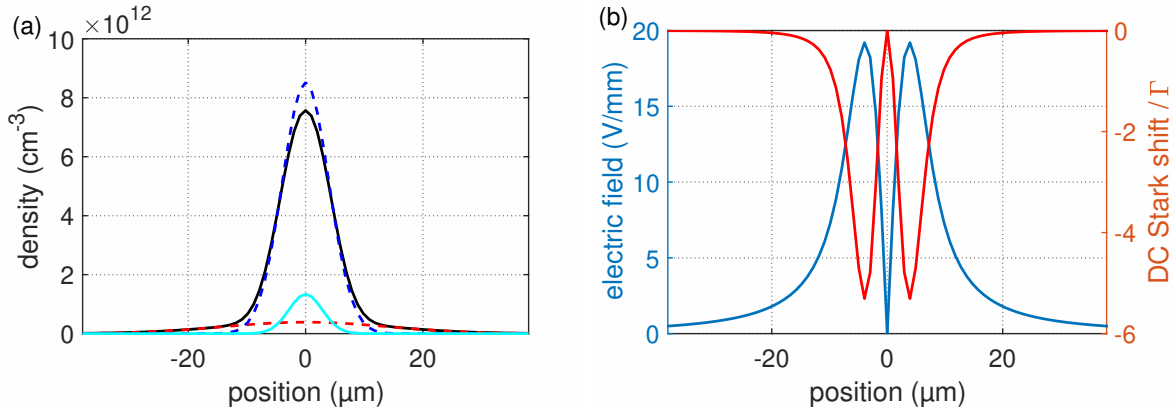

Figure 3.17.: Stark shift induced by 500 ions. (a) Cuts through the total density (solid black) and the ion density (solid cyan). The thermal (red) and the condensed fractions of the total density are depicted as dashed lines. (b) Electrical field (blue) of a spherical charge distribution with the size of the ionization volume and the corresponding Stark shift (red) units of the imaging transition bandwidth $\Gamma = 6\,\mathrm{MHz}$.

The simulated absorption images in figure 3.18 illustrate the effect onto a cloud of 24,500 atoms. In the example shown here only 28 % of the atoms remain visible. When the ions are localized in the center of the cloud and a large number of atoms surround them the Stark effect is pronounced because the shift is strongest at the edge of the charge distribution. On the other hand when the extension of the condensed fraction is smaller than the size of the ion distribution most of the atoms are within the charge distribution and the level shift is much smaller.

The simulation shows that the Stark shift introduced by a small number of ions (≈2 %) is

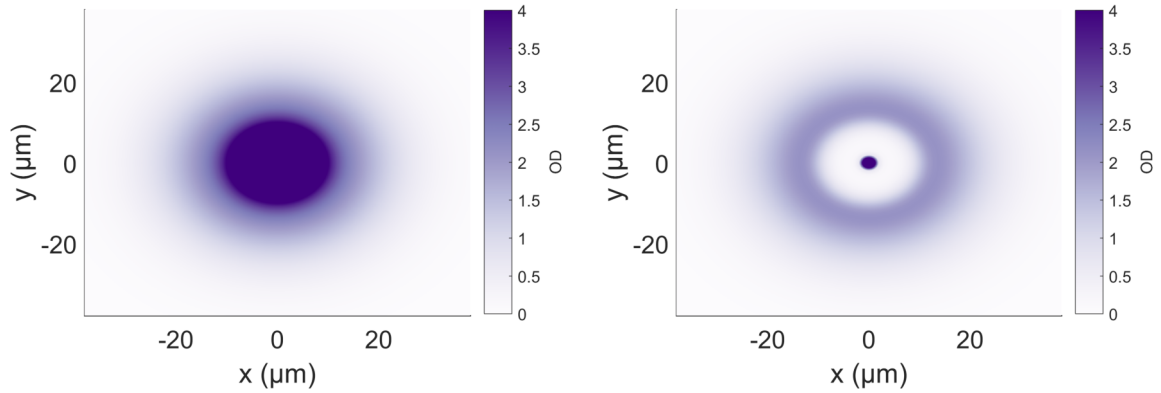

Figure 3.18.: Simulated absorption images. The atom density from figure 3.17 leads to the left absorption image. The image on the right shows the optical density in the presence of 500 ions. Due to the Stark shift about 72 % of the atoms are out of resonance with the imaging light.

strong enough to shift atoms out of resonance for the imaging light. However inside the focal region where the atom density as well as the ion density is the highest the calculation is probably inaccurate. In this region the randomly distributed ions should rather be treated as discrete charges than as a continuous distribution.

Although the assumption of a charged sphere is able to explain the invisibility of large fractions of the atoms it does not explain the observed time scales. Due to Coulomb repulsion, the ions should expand quickly at a speed that can be estimated by solving the differential equation derived from Coulomb's law for two close-by charges:

$$\ddot{r} = \frac{q^2}{4\pi\epsilon_0 m_{Rb}} \times \frac{1}{r^2} \tag{3.15}$$

with the initial condition $r_0 = a_{ws}$ and $\dot{r}_0 = 0$. The Wigner-Seitz radius $a_{ws} = (4/3\pi n_i)^{-1/3}$ evaluates to approximately 400 nm and gives the mean inter-particle distance for a given initial density at $t = 0$. The numerical solution reveals that two ions will have a distance of 15 µm after 200 ns. In comparison the 1/e size of the thermal cloud is 14 µm.

In summary the Stark shift induced by the ions could take the atoms out of resonance with the imaging light but the effect should decay orders of magnitudes faster than what is observed. If the effect of vanishing atoms is caused by ions their Coulomb expansion must be hindered through the interaction with atoms or photoelectrons.

3.4.3. Atom-Ion Scattering

The interaction between atoms and ions is treated in the framework of scattering theory. The collision energies in this experiment are high enough to allow the use of semi-classical expressions for the scattering cross sections. The differential cross section has two maximums one in forward

and on in backward direction. The scattering angle ϑ is usually measured in the center of mass system. Forward scattering ($\vartheta = 0$) then means small deflection by the scattering center and very little momentum is transferred from the fast ion to the atom. Backward scattering ($\vartheta = \pi$) on the other hand is head-on collisions and provide full exchange of momentum. Therefore ions are stopped efficiently at large scattering angles.

The forward direction is associated with elastic scattering while the backward path is identified with charge transfer reactions [104]. The elastic scattering cross section is given by:

$$\sigma_{el} = 4174 \times E_{col}^{-1/3} = 2.78 \times 10^{-10}\,\mathrm{cm}^2 \tag{3.16}$$

Whereas the corresponding backward cross section is given by Langevin's formula:

$$\sigma_L = \pi \times \sqrt{2C_4/E_{col}} = 1.33 \times 10^{-13}\,\mathrm{cm}^2 \tag{3.17}$$

Both expressions are in atomic units and $C_4 = 159.6$ is the polarizability of ^{87}Rb [37]. The collision energy $E_{col} = 4.0\,\mathrm{meV}$ was estimated from the Coulomb potential between two ions at the mean inter-atomic distance $\bar{d} = 370\,\mathrm{nm}$.

At a typical peak density of the condensate of $n = 4 \times 10^{12}\,\mathrm{cm}^{-3}$ and size on the order of $r = 15\,\mu\mathrm{m}$ the probability for an scattering event between an ion and an atom is given by $P_s = \int \sigma n(r) dr = 1.7$. On average every ion leaving the cloud can collide two times. However only backward scattering processes can decelerate the ions which are two orders of magnitude less probable. Overall the estimated scattering rate is too low to hinder the expansion of the ions.

It is also clear that the atom-ion collision energies are way too large to lead to interaction effects on the quantum level such as polarons. In the Fröhlich picture interaction between an impurity and host bosons is quantified with the s-wave (l=0) scattering length [105]. However, the calculation of the quantum mechanical cross section shows that about 200 partial waves (l=0, 1, . . . , 200) contribute to the scattering phase.

3.4.4. Ultracold Plasma

The creation of large numbers of ions and photoelectrons in a laser focus can lead to the formation of plasma. The ensemble of ions provide an attractive potential for photoelectrons after some of the electrons have left the cloud. Ultracold plasmas have been studied in laser-cooled atomic clouds [47]. This many-body interaction may be a mechanism to slow down the expansion of the cloud because the electrons shield the repulsive interaction among ions. The evolution of an ultracold plasma consists of phases which are illustrated in figure 3.19.

Directly after the ionization at t_0 both photoelectrons and ions are located randomly inside

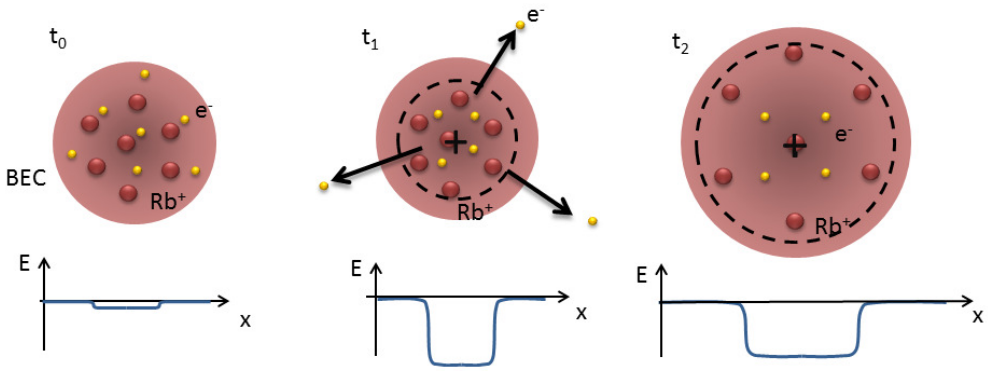

Figure 3.19.: Schematic evolution of an ultracold plasma. After ionization at t_0 photoelectrons leave the cloud until the Coulomb potential of the ions is strong enough to hold them back (t_1). The net positive charge then causes expansion of the cloud. The inset shows the time evolution of the Coulomb potential that captures the electrons

the focal region of the laser. The electrons inherit most of the excess energy and leave the interaction volume quickly. Each electron that escapes leaves an excess positive charge behind. In this way the attractive Coulomb potential for photoelectrons is formed. Depending on their kinetic energy $2\hbar\omega_{SH} - U_i$ a critical number of ions N^* is required to form a plasma state within the ionization volume of radius d [46]:

$$N^* = (2\hbar\omega_L - U_i) \times \frac{4\pi\epsilon_0}{\sqrt{2/\pi}e^2} d \tag{3.18}$$

The elementary charge is e and the vacuum permittivity is ϵ_0. For our experimental parameters a plasma state can only be formed if 10 % of the atoms or more are ionized. Indeed the kinetic energy of the photoelectrons ($E_{kin} = 666\,\text{meV}$) requires a large charge imbalance to capture the first electron in the potential of the ions. The ionized fraction should shift the atoms out of resonance (see figure 3.16).

During the second phase after t_1 the ions will start to re-arrange reducing their disorder. It is significantly slower because of the higher mass of the ions. The time scales for the electron and ion dynamics in the first and second phase is given by the inverse plasma frequencies:

$$\frac{1}{\omega_{e,Rb}} = \sqrt{\frac{ne^2}{m_{e,Rb}\epsilon_0}} \tag{3.19}$$

Here $n = 4 \times 10^{12}\,\text{cm}^{-3}$ denominates the typical atomic density, $m_{e,Rb}$ is the mass of the electron and ion, respectively. Typically the electrons thermalize within a few picoseconds while the ions take a few nanoseconds to equilibrate.

The third phase at t_2 is characterized by an expansion of the whole cloud. Under the condition of weak coupling it is driven by thermal motion. Therefore the expansion time scale is given by

the excess kinetic energy $E_{e,Rb}$ the particles inherit from the ionization process.

$$\tau_{exp} = \sqrt{\frac{3m_{Rb}d^2}{2(E_{Rb} + E_e)}} \tag{3.20}$$

For our experiment a time scale of 11 ns is expected. The size of the plasma d is given by the waist of the ionization beam.

Although it is possible to create ultracold plasma in our experimental setup it is incompatible with the observed time scales. However it has been reported that Rydberg states can be formed from ultracold plasma via three-body recombination where one ion recombines with an electron while a second electron is used conserve energy and momentum [106]. This mechanism could lead to excitation of long-lived Rydberg states.

3.4.5. Summary

The creation of ions can leads to shifting a large fraction of atoms out of resonance with the imaging light. However, the observed time scale is only compatible with the lifetime of highly excited Rydberg states. Direct optical excitation of those states is energetically impossible in the experiment. Ultracold plasmas which can be created by ionizing many atoms in the focal region may lead to the creation of such states. Although plasmas decay on a nanosecond time scale Rydberg states can be formed by three-body recombination. Future investigations are required to identify the relevant mechanism.

3.5. Conclusion

In this chapter different aspects regarding ultracold atomic clouds interacting with femtosecond laser pulses have been presented. Starting with the ionization rate of ^{87}Rb in strong light fields in section 3.1. It can be described using the multiphoton picture until the local intensity is high enough to allow over-the-barrier ionization. Tunneling ionization plays a minor role as the multiphoton ionization probability is always significantly larger for intensities below I_{OBI}.

Furthermore it has been demonstrated in section 3.2 that each laser pulse exerts an transient optical dipole force on the atomic cloud. The repulsive force adds a radial velocity distribution that has been measured using time-of-flight series. Opposed to the statistical nature of ionization the dipole force affects all atoms deterministically. However the strength depends on the polarizability of the electronic state. Hence, ^{87}Rb ions with their rare gas-like electron configuration are way less susceptible to it than ground state atoms.

Section 3.3 in this chapter has discussed the relaxation of the dip in the atom density induced by the laser pulses. In a thermal cloud the dynamics can be described by the Boltzmann equation. The derived 1D model is in very good agreement with the measured data. As it is not possible to detect the shape of the dip accurately for high densities this measurement could not be performed in the optical dipole trap and a comparison between thermal and condensed samples was not accessible. Nevertheless it has been observed that the laser pulses can excite collective modes (center-of-mass oscillations, breathing) in the trap.

The chapter concludes with the discussion of atom-ion interaction effects in section 3.4. Large ion densities in the center of the cloud cause temporary invisibility of atoms while the atom loss is negligible. The time scale of the re-appearance suggests the excitation of Rydberg states that can polarize surrounding atoms. In this way the atomic energy levels are shifted out of resonance with the probe light. The excitation mechanism is not fully clear as the scattering cross sections are small. Three-body recombination in an ultracold plasma can lead to formation of such Rydberg atoms from two electrons and an ion.

CHAPTER 4

Imaging Photoelectrons emerging from a Bose-Einstein Condensate

Studying the coherence transfer to photoelectrons emerging from a degenerate quantum gas is technically challenging and requires a new experimental setup. After compiling the general layout of the experiment, the necessary components have been designed and built in this work. Most of them have been already characterized, so the new setup can be assembled in the near future.

Photoelectrons emerging from a BEC can give new insights to fundamental questions of quantum physics. Can macroscopic coherence of a BEC be transferred to its microscopic constituents? How does the bosonic statistics of the condensed atoms influence the distribution of photoelectrons? Questions related to the emergence and the transfer of coherence in quantum systems and will be addressed in future experiments by detecting two-particle interference patterns of photoelectrons emerging from a ^{87}Rb BEC. The design of the new experimental setup is presented in the course of this chapter. Starting from general aspects, the development of the required components is discussed. Many of these have been built and characterized and are now ready for assembly.

Parts of this chapter concerning the hybrid trap and the optical transport have been presented also in the Master's theses of Harry Krüger [62] and Tobias Kroker [59].

4.1. Designing a Novel Quantum Gas Experiment

The idea of the experiment is to create photoelectrons in two adjacent but distinct locations of a ^{87}Rb BEC using femtosecond laser pulses. After their creation their wave functions will evolve freely and overlap in the detection plane. As the electrons are indistinguishable an interference pattern similar to Young's double slit should be recorded with an imaging detector [2].

The new setup is shown schematically in figure 4.1. The atomic cloud is ionized by two tightly focused femtosecond laser beams with an intensity which allows for creating one electron in each focus. The electrons evolve until they hit the position-sensitive detectors. These detectors are installed vis-à-vis as the angle between the classical electron trajectories will be close to π due to Coulomb interaction.

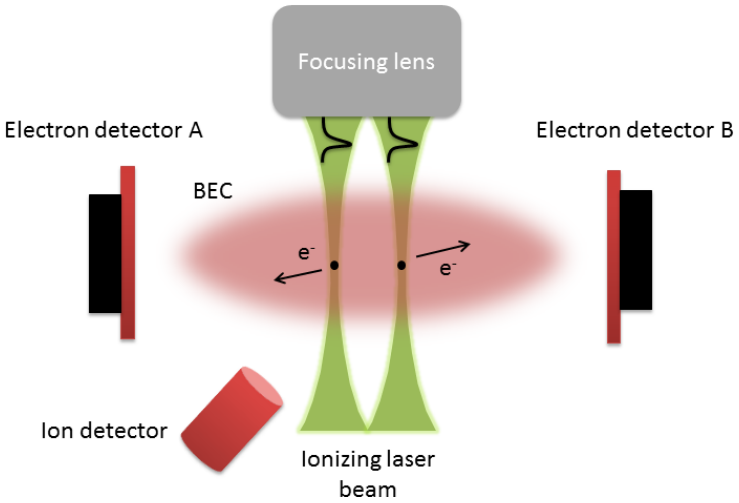

Figure 4.1.: Imaging photoelectrons emerging from a BEC. After ionization in the two laser foci photoelectrons will be detected in coincidence with the corresponding ions. If the electron wave packets emitted from the foci are coherent an interference pattern shall be recorded on the screen of the detectors. Image adapted from [107].

In order to resolve interference fringes of the electron waves the de Broglie wavelength must be as large as possible. Hence the electrons need to be created with the least possible amount of kinetic energy by tuning the ionizing laser close to the ionization threshold. The design of the experiment is based on a interference shown in figure 4.2. It has been calculated for to point sources at a distance $d = 1\,\mu\text{m}$. The kinetic energy $E_{kin} = 50\,\text{meV}$ determines the de Broglie wavelength. The spacing between the fringes on the millimeter scale can be resolved using MCP detectors.

A counting ion detector will be added to the setup in order to validate coincident events on the electron detectors. If two ions are detected coincidently with the two electrons there is a high probability that all fragments were created in the same event. Using coincidence detection invalid events that would destroy the interference pattern can be discarded.

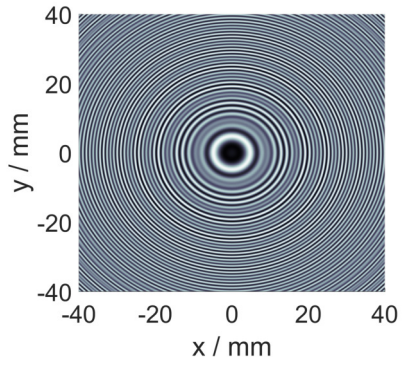

Figure 4.2.: Interference pattern of two spherical waves emitted at 1 µm distance. The de Broglie wavelength for the electrons is $\lambda_{dB} = 4.2\,\text{nm}$.

4.1.1. Experimental Setup

The implementation of such an experiment is technically challenging. Ultracold atomic gases require an excellent base pressure $<1 \times 10^{-11}$ mbar, and optical access for the trapping and ionizing laser beams. The recipient must also provide enough space to host the detectors for charged particles.

As the experiment aims at interference of electron waves it must be extremely well shielded against electric and magnetic stray fields which would imprint uncontrolled phases on the photoelectron wave packets.

Furthermore the experiment will suffer from a low repetition rate since the preparation of a BEC typically requires 20 s to 30 s. To allow for measurements with reasonable statistics a single BEC shall be re-used for multiple ionization experiments. Hence, the detection system must be able to cope with the repetition rate of the ionizing femtosecond laser ($f_{rep} = 100\,\text{kHz}$) while providing high detection efficiency for single particles.

The glass cell that contained the atomic cloud in the measurements presented in chapter 3 does not meet these requirements. So the experimental setup needs a massive extension in order to be suitable for the new experiments. While the 2D MOT setup can be reused, the lower glass cell is replaced by a new vacuum chamber. Figure 4.3 displays the experimental setup featuring the new preparation chamber in the center. Because a magnetic trap is needed for the preparation of ultracold clouds this new chamber must be spatially separated from the interaction region in the science chamber. This implies that a transport mechanism must be implemented in order to transfer the cloud from its origin into the focus region of the ionizing laser. The transport will be realized by optical tweezers.

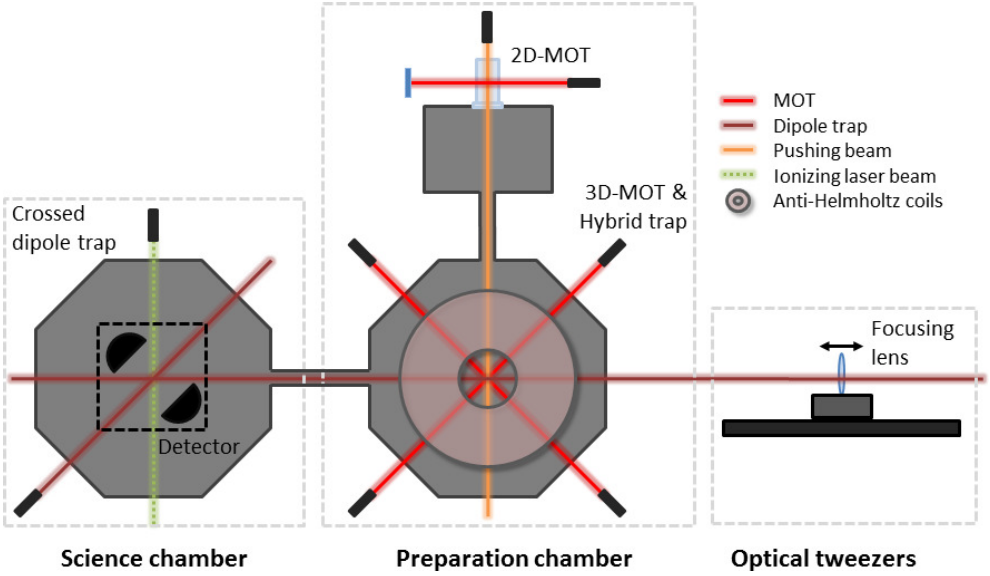

Figure 4.3.: Schematic of the new setup. Starting from the 2D MOT the atomic cloud is pushed down into the new preparation chamber where it is cooled optically in the 3D MOT before forced evaporative cooling is applied in the hybrid trap. Then the optical tweezers are used to transfer the sample into the science chamber where the measurements will be performed.

4.2. Preparation of ultracold atomic samples

From figure 4.3 it becomes already clear that the preparation of ultracold samples itself is a complex task. Multiple trapping and cooling steps involving a number of techniques are required before the sample can be probed with the ionizing beam. Hence this section details the components that were developed for the preparation of ultracold atomic clouds.

Starting from the experimental sequence in section 4.2.1, the vacuum system (section 4.2.2), the hybrid trap (section 4.2.3) as well as the optical transport (section 4.2.4) will be described.

4.2.1. Experimental Sequence

The protocol for preparing ultracold atomic clouds is similar to the one described in section 2.1. The modified experimental cycle is sketched in figure 4.4. After collecting ^{87}Rb atoms from the background vapor in the 2D MOT they are transfered into the preparation chamber (see figure 4.7) where they are cooled in a 3D MOT. The atoms are then loaded into the hybrid trap that consists of a magnetic potential created by a set of anti-Helmholtz coils and the superimposed optical potential of a trapping beam [69]. In this way Majorana losses that would occur at $B = 0$ are suppressed [68, 8]. The atoms are cooled further by means of forced rf-evaporation [15] until they occupy the volume of the trapping beam. The atoms are then transferred into the science chamber by translating the focus of the optical trap [108]. Here a second trapping beam is added to create a crossed optical dipole trap, where the sample is further cooled to degeneracy

[73, 61].

In summary the main difference in comparison to the current cycle is the introduction of the optical transport before the last evaporation step.

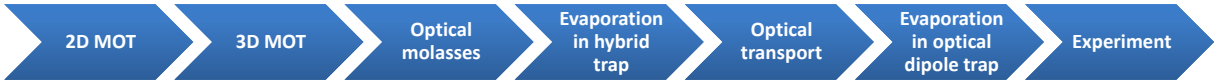

Figure 4.4.: Experimental sequence for preparing ultracold atomic clouds.

4.2.2. Vacuum System

The new science chamber that hosts the electron and ion detectors will be added to the current system. It is connected to the 2D MOT setup by the new octagonal preparation chamber (see section 4.2.3) that replaces 3D MOT glass cell.

The new vacuum system must reach a base pressure $<1 \times 10^{-11}$ mbar in order to achieve several seconds lifetime, essential for the evaporative cooling and the transport of the atomic cloud.

The science chamber[1] features good optical access while keeping the volume and the inner surface low. The system has a total volume of 6.04 L, half of it (2.84 L) is the chamber itself. It is shown in figure 4.5 sitting on top of the 5-way cross that connects it to the vacuum pumps. The science chamber is designed to be separable from the preparation chamber by an all-metal gate valve[2] which allows modifying the detectors while maintaining the vacuum in the preparation chamber. A second valve is placed in front of the turbo molecular pump. This pump is only used to evacuate the science chamber from rough vacuum down to the ultra-high vacuum regime. Then the ion getter pump takes over and the valve is closed.

To minimize stray magnetic fields all components are made from stainless steel with low magnetic susceptibility. Depending on the distributor either 316L(N) or 1.4429ESU alloy was chosen. Non-magnetic, viewports with high optical quality ($<\lambda/4$) and low leak rate ($<1 \times 10^{-10}$ mbar L s^{-1}) are very difficult to get. The windows[3] are bonded to the flange with titanium as it is non-magnetic and has low outgasing. The windows also have suitable anti-reflection coatings: The viewports for the cooling and imaging beams are equipped with a broadband coating at 550 nm to 1100 nm, the trapping beams are transmitted trough laser line windows at 1064 nm and the electron detectors are imaged through viewports which are coated for 425 nm to 760 nm.

The uncoated re-entrant viewport sitting on the top of the chamber is glued (probably with TorrSeal) to the flange in order to achieve the required optical flatness. To prevent outgasing of

[1] Kimball Physics Inc., MCF450-SphCube-E6C8A12
[2] VAT Vakuumventile AG, 48132-CE01
[3] Allectra, 110S-QZ-CF40-NM & 110S-CF63-QZ-NM

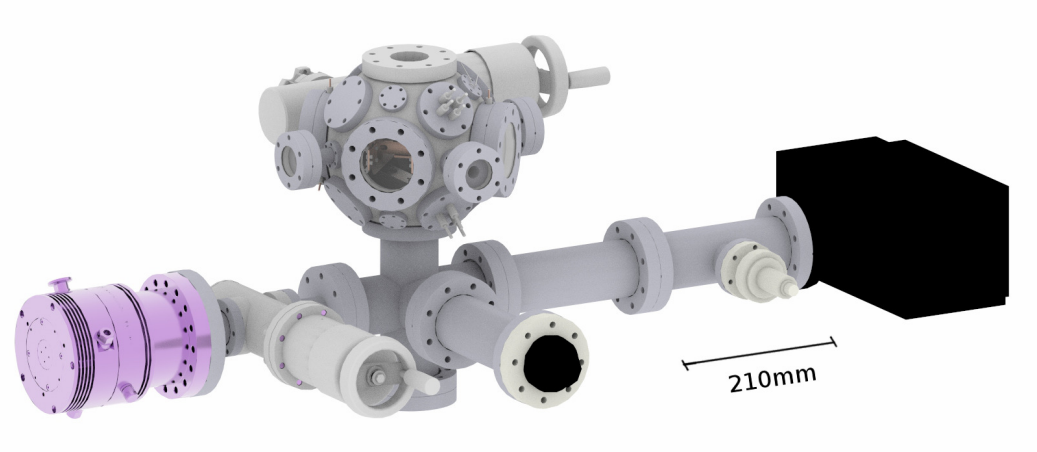

Figure 4.5.: Science chamber and vacuum system. The new spherical chamber sits on top of a tube that connects it to a turbo molecular pump (magenta), an ion-getter pump (black) and a titanium sublimation cartridge right beneath the chamber. The turbo pump can be disconnected after closing the gate valve. A second valve in the background is used for the connection to the preparation chamber.

the adhesive we coated its surface that is exposed to the vacuum side with a micrometer thick aluminum layer.

Two devices of the vacuum system rely on strong magnetic fields. The ion getter pump[4] (IGP) uses strong magnets for efficient ionization of residual gas atoms which are then accelerated in a strong electric field and implanted in the electrodes. Also the cold cathode gauge[5] exhibits a strong magnetic field but it is the only device that can measure pressures down to 1×10^{-11} mbar. To minimize their influence both devices are placed as far as possible from the interaction volume. The long connection tube to the pump reduces its nominal pump speed in the science chamber to effectively $S_i = 26\,\mathrm{L\,s^{-1}}$.

Assuming a total leak rate of $Q_l = 1 \times 10^{-9}\,\mathrm{mbar\,L\,s^{-1}}$ leads to a base pressure of:

$$p_l = Q_l / S_i = 3.8 \times 10^{-11}\,\mathrm{mbar}$$

In the regime of extremely high vacuum not only the leak rate is important but also the desorption of hydrogen from (steel) surfaces plays an important role. With an normalized desorption rate of $q_d = 2.7 \times 10^{-11}\,\mathrm{mbar\,L\,s^{-1}\,m^{-2}}$ the contribution of desorption is [109]:

$$p_d = q_d \times A / S_i = 8.4 \times 10^{-11}\,\mathrm{mbar}$$

as the total inner surface is about $A = 5350\,\mathrm{cm^2}$.

The pump speed of the IGP depends on the pressure and the residual gas composition. Atmo-

[4] Agilent, VacIon Plus 55 StarCell
[5] Pfeiffer Vacuum, IKR070

spheric gases like nitrogen and oxygen are pumped more efficiently than rare gases and hydrogen. So the partial pressure of hydrogen becomes dominant below 1×10^{-10} mbar. Therefore the IGP is supported by an titanium sublimation cartridge that provides effectively additional $300\,\mathrm{L\,s^{-1}}$ of pumping speed. From its filaments titanium which is a getter material can be sublimated and deposited onto the chamber walls. It is installed right beneath the science chamber and allows to reach a base pressure $< 1 \times 10^{-11}$ mbar.

It turned out that vacuum annealing all steel components is crucial for reaching the desired base pressure. In this process all steel parts (flanges and tubes) were heated to about 900 °C to remove hydrogen from the bulk [110, 111]. The science chamber itself was not subject to this treatment as it is made from 316L. This alloy is not strong enough and there was a risk of destroying the knife edges.

Additionally it was found that half of the viewports had significantly higher leak rates than claimed by the distributor. These rates were in the range of $5 \times 10^{-9}\,\mathrm{mbar\,L\,s^{-1}}$ and therefore hard to detect with standard He leak testing. To make sure the test gas does not diffuse into the surrounding atmosphere a plastic cap with a small opening to inject He was mounted on the viewport during the test. Once the defect viewports were identified the leaks could be easily fixed by applying liquid Vacseal into the gap between the flange and the window.

Figure 4.6 shows the successful bake-out procedure with a peak temperature of 120 °C that removed adsorbed water from the surface of the vacuum chamber. In this run all viewports and one of the electron detectors were installed. The system was evacuated with the turbo molecular pump to a regime where the IGP could be turned on for a short time to get rid of material emerging from it after each air contact. Then the IGP was disconnected and the system was completely wrapped with heating tape and some layers of aluminum foil for thermal isolation. Special care was taken to not exceed temperature specification of individual components. After three days at $T = 120\,°\mathrm{C}$ the system was cooled down again and the IGP was reactivated. In the range of 5×10^{-10} mbar the valve to the turbo pump was closed and titanium was sublimated three times for one minute at a current of 47 A. To pump down the system from atmospheric pressure to below 1×10^{-11} mbar takes about 8 days.

4.2.3. Magnetic Trap

For the new preparation chamber a set of Helmholtz coils has been designed. It generates a magnetic field gradient for the 3D MOT and the hybrid trap [62]. The main design target was to find a configuration that allows for a B-field gradient larger than $1.75\,\mathrm{T\,m^{-1}}$ [69]. As several kilowatts of heat is dissipated in such coils water cooling had to be included in the design.

To achieve the required field gradient an arrangement with two concentric sets of Helmholtz coils was chosen (see figure 4.7). One set of large coils surrounding the zero-length adapter flanges that are mounted onto the vacuum chamber. A second set is smaller in diameter and sits

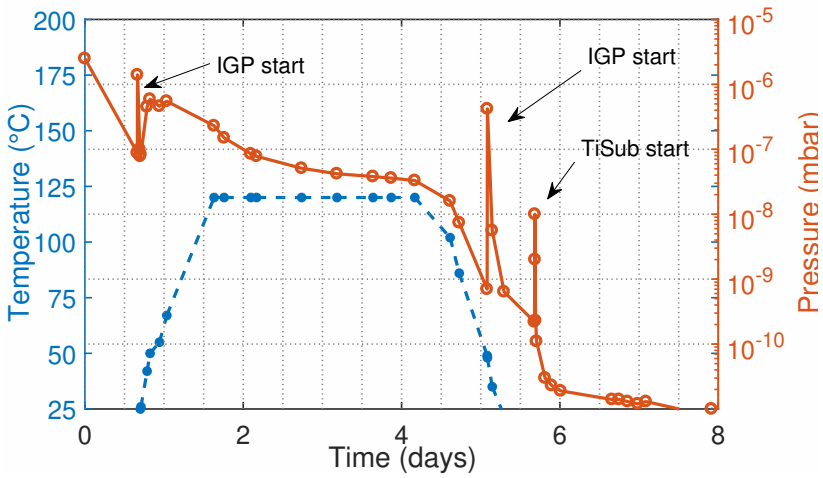

Figure 4.6.: Bake-out of the Science chamber. After initial pumping of the vacuum system the temperature (blue dashed line) is slowly ramped up well above 100 °C. The turbo-molecular pump removes desorbed residual gas – mainly water – from the system. The pressure (red line) drops during the cool-down to the 1×10^{-11} mbar range.

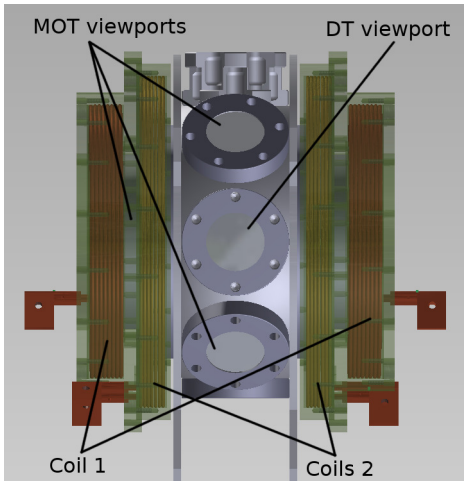

Figure 4.7.: Front view of the preparation chamber. The new magnetic trap coils are inside a glass fiber reinforced housings that are mounted directly onto the chamber. The coils are cooled with water flowing through each compartment of the housing.

on top of the large coils. The housing made from glass fiber-reinforced plastic contains one coil of each set in a separate compartment. During the manufacturing it was noticed that the housing was a bit too tight to accommodate the large coil. But the problem could be solved by reducing the wire diameter and adding another layer to the coil. The updated numbers for the geometry are summarized in table 4.1.

	inner diameter	outer diameter	length	∅ wire	turns	layers
coil 1	131.2	178.8	22.9	2.5	8	8
coil 2	168.4	216.0	18.2	2.0	7	9

Table 4.1.: Mechanical properties of the Helmholtz coils. The diameters and the length are given in millimeters.

The magnetic field of the trap has been characterized at a current of 10 A using a Hall probe

mounted on a motorized xyz-translation stage. The measured B-field along and perpendicular to the symmetry axis of the trap is plotted in figure 4.8. From linear fits the gradients were determined to $(0.1516 \pm 0.0008)\,\mathrm{T/(Am)}$ along the symmetry axis and $(0.079 \pm 0.002)\,\mathrm{T/(Am)}$ perpendicular to it.

The numerical calculation of the field using Biot-Savart's law yields a gradient along the axis $dB/dz = 0.136\,\mathrm{T/(Am)}$ and $dB/dr = 0.0685\,\mathrm{T/(Am)}$. The measured values are 11 % larger than expected from the calculation. The deviation results from the uncertainty of the coil position as the coils were not attached to the preparation chamber during the test but mounted in a separate test setup. Although care was taken to align the coil housings correctly the exact positions of the coils inside their housing remain uncertain.

As the gradient scales linearly with the current one can infer that a current of 115 A is needed to achieve the target gradient of $1.75\,\mathrm{T\,m^{-1}}$. During the MOT phase a field gradient of $0.39\,\mathrm{T\,m^{-1}}$ is used which can be achieved with 26 A.

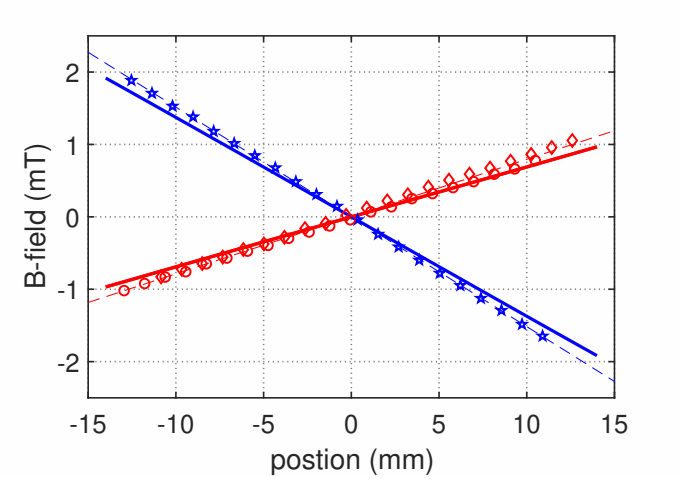

Figure 4.8.: Magnetic field of the coils at 10 A anti-Helmholtz. The measurement was performed along the trap axis (stars) and two perpendicular directions (diamonds, circles). A linear fit (dashed line) to the data gives a gradient which is in good agreement with theory (solid line).

Table 4.2 summarizes the electrical properties of the coils. The resistance was determined from a linear fit to the current-voltage characteristic. The voltage and the power dissipation were calculated from that resistance and the current needed for the target gradient. The inductance was calculated numerically.

The coils must be water cooled since their estimated power dissipation is rather large. Each compartment of the coil housing is equipped with separate water connectors and the cooling water flows directly around the wires. The water system features an interlock that switches off the electrical current in the coils if the water supply fails [112]. Additionally the interlock monitors the temperature of the cooling water and protects the coils from overheating. The water flowing at a rate of $3\,\mathrm{L\,min^{-1}}$ is heated by about 6 °C when the coils operate in the anticipated

	inductance	resistance	voltage	power	axial gradient	radial gradient
coil 1	0.84 mH	0.11 Ω	12.7 V	1.5 kW	-	-
coil 2	1.17 mH	0.21 Ω	24.2 V	2.8 kW	-	-
total	4.02 mH	0.64 Ω	73.6 V	8.5 kW	0.0152 T/(Am)	0.0079 T/(Am)

Table 4.2.: Electrical properties of the Helmholtz coils. The inductance was calculated numerically. All other quantities are based on measurements. Voltage and power are given for a current of 115 A.

duty cycle (10 s on / 25 s off). The heating of the cooling water can be easily handled by the heat exchanger.

For stable operation of the trap all coils are connected in series. The electrical current is provided by two sources[6] that need to be operated in series to reach 115 A. A master/slave operation mode is used to synchronize the control loops of both devices. To switch current in the coils an array of insulated-get bipolar transistors[7] (IGBT) is used. The circuit shown in 4.9 features an H-bride to allow operation in Helmholtz and in anti-Helmholtz configuration. As the switching of large currents induces high voltage peaks due to self-inductance of the coils the IGBTs are protected by varistors[8].

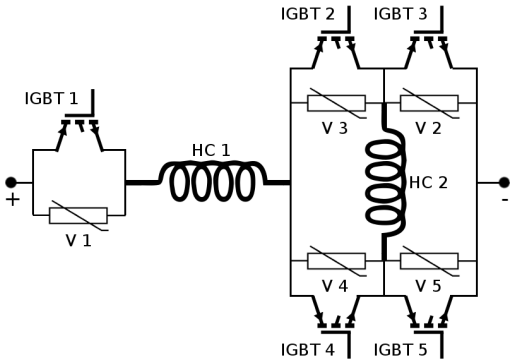

Figure 4.9.: Switching circuit for the magnetic trap. The varistors parallel to the IGBTs protect them from overvoltage caused by self inductance.

4.2.4. Optical Transport

Ultracold atoms can be transferred over large distances by moving the trap which confines them [113]. For the planned experiment a transport is required in order to move the atoms from the preparation chamber to a volume that is free of stray electric and magnetic fields. The focusing lens of the optical dipole trap is mounted on a translation stage acting as optical

[6]Delta Elektronika, Delta Power Supply SM 45-140
[7]IGBT: Mitsubishi Electric, CM200DX-24S. Gate drive unit: Ishaya Electronics Corporation, VLA536-01R
[8]Epcos AG, 4B40K320

tweezers [108, 114]. The setup for the transport is sketched in figure 4.10. It features a fiber collimator with a suitable focusing lens L_3, an air-bearing translation stage[9] and a feedback loop for stabilizing the beam pointing with a piezo-actuated mirror.

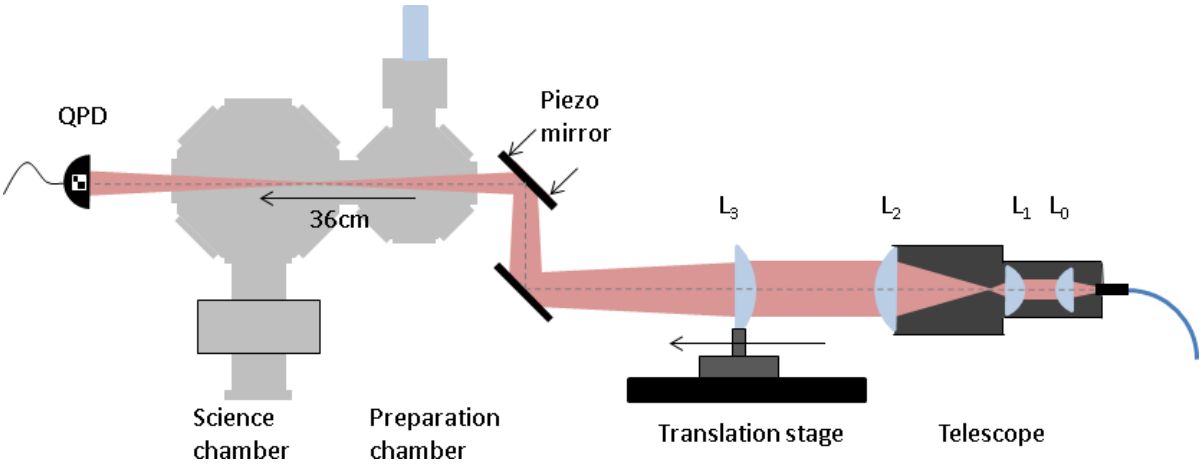

Figure 4.10.: Optical transport from the preparation to the science chamber. The trapping beam coming from an optical fiber is enlarged and collimated in the telescope. The atoms inside the optical dipole trap are moved across 36 cm by translating focusing lens L_3 with an air bearing stage. The beam pointing is actively stabilized with a piezo mirror by the feedback from a quadrant photodiode (QPD).

The distance that needs to be covered by the transport is 36 cm. The focal length of the last lens L_3 is $f_3 = 750\,\text{mm}$ due to geometrical constraints. The telescope consisting of L_1 and L_2 widens the beam that comes from the collimation lens L_0 in order to get a diffraction-limited focus after the last lens L_3. Assuming a Gaussian beam one can calculate the required beam diameter w_3 on the last lens as the waist of the trap shall be $w_0 = 40\,\mu\text{m}$.

$$w_3 = w_0\sqrt{1+\left(\frac{f_3}{z_R}\right)^2} = 6.4\,\text{mm}$$

At the laser wavelength of $\lambda_{dip} = 1064\,\text{nm}$ the Rayleigh range evaluates to $z_R = \pi\omega_0^2/\lambda_{dip} = 4.7\,\text{mm}$. The ratio of the beam diameters after the collimation lens L_0 and in front of the focusing lens determine the magnification $M = 15$ of the telescope. It follows that the focal lengths of L_2 and L_1 are 300 mm and 20 mm respectively [115].

The trapping frequencies can be calculated by approximating the optical potential harmonically (see equation (2.5)). At the maximum power of 3 W this expression yields $f_{rad} = 1.1\,\text{kHz}$ for the radial frequency and $f_{ax} = 6.3\,\text{Hz}$ in axial direction and a trap depth of about 170 µK.

A major difficulty of this transport method are mechanical vibrations that can lead to parametric heating of the atomic cloud and thus to significant atom losses [116]. The use of an

[9] Dover Motion, AG-400. Control unit: Aerotech, Soloist ML-10-40-IO

air-bearing translation stage decouples the slide mechanically from the underlying structure. The stability and accuracy of our translation stage has been verified together with Maik Schröder in his Bachelor's work [117]. Furthermore the minimum time of travel was determined to be 0.8 s.

Heating effects occur not only due to mechanical vibrations but also due to the acceleration and deceleration in the transport itself. By choosing a good velocity profile this effect can be reduced significantly. In general there are two approaches: *Adiabatic transport* tries to minimize heating by increasing the transport time to much longer value than the oscillation period of the trap. As the axial trap frequency is very low because of the large focal length of L_3 adiabatic transport is not feasible in our setup. *Optimal transport* on the other hand is significantly faster. It matches the transport time to the inverse trap frequency [118]. For a triangular velocity profile the transport time should be equal to even multiples of the inverse trap to avoid oscillations after the transport. With the parameters of the new optical trap the lowest transport time would be $T_j = 2j/f_{ax} = 0.32\,\mathrm{s}$. The measured minimum travel time of the linear stage imposes at least $j = 3$ rendering a transport time of $T_3 = 0.95\,\mathrm{s}$ feasible.

4.2.5. Summary

The concept for a novel experiment combining ultracold atoms and ultrafast lasers has been developed. A new vacuum system has been designed and built that hosts the detectors for charged particles. After identifying leaks in the viewports the required base pressure ($<1 \times 10^{-11}$ mbar) has been reached.

In addition the preparation chamber with a new magnetic trap was designed and built, including the IGBT-based switching electronics. The trap is able to provide the required field gradient of $1.75\,\mathrm{T\,m^{-1}}$ at 115 A.

Finally for the optical transport a linear translation stage was setup and characterized. It features low vibrational noise and achieves good position accuracy. Additionally a new fiber telescope has been developed that as allows focusing the trapping beam at $\lambda_{dip} = 1064\,\mathrm{nm}$ down to $w_{dip} = 40\,\mu\mathrm{m}$. The setup is completed by the implementation of a beam stabilization system.

4.3. Femstosecond Laser

The femtosecond laser system used for ionizing atoms was already presented in section 2.2.1. Some additional remarks are made here regarding its future use.

First of all the photoionization process transfers kinetic energy to the electrons. This should be minimized in order to achieve a large de Broglie wavelength and facilitate the observation of interference patterns. Therefor the photon energy of the ionizing laser beam must be tuned close to the ionization threshold. Secondly the photoelectrons shall be created in two close-by but distinct spots. Section 4.3.2 presents the optical setup that creates two adjacent, diffraction limited foci. The section concludes with an assessment of laser intensities and an brief description of our beam stabilization systems.

4.3.1. Kinetic Energy of Photoelectrons

The excess energy of the photoelectrons can be minimized by tuning the wavelength to the two-photon ionization threshold at 593.63 nm. Light of this wavelength can be generated in the optical parametric amplifier with an output power of almost 100 mW. The spectral bandwidth of the laser pulses is about 1.7 nm and defines the energy spread of the photoelectrons ΔE.

For a Fourier-transform-limited pulse with a Gaussian profile and a duration $\tau = 280\,\text{fs}$ the energy spread of the photoelectrons can be estimated using the time-bandwidth product $\tau \times \Delta f = 0.441$ [97]:

$$\Delta E = \frac{0.441}{\tau} \times \frac{h}{e} = 12\,\text{meV}$$

Here h and e are the Planck's constant and the elementary charge respectively. This spread is taken into account in the interference pattern in figure 4.2.

4.3.2. Creating diffraction-limited, adjacent Laser Foci

The ionizing laser beam is focused with a planar apochromatic objective lens[10] which is compensated for a 3.5 mm thick window. The objective lens has a working distance W.D. = 13.89 mm and its numerical aperture NA = 0.5 gives rise to a nominal resolving power of 600 nm.

Together with Jasper Frohn the resolution of the objective was measured with a Siemens star of 40 µm diameter [119]. From the ratio of the total radius to the radius where the spokes are not resolvable anymore a resolving power of 430 nm was determined. The specification refers probably to real microscopy applications were the samples are much thicker and have weaker contrast than the sample we used. Note that it is critical to use a window of correct thickness. If the window is only 15 % thinner than the nominal value i.e. 3 mm the resolving power goes down by a factor 1.5. Additionally the size of a single diode laser focus was measured by imaging it

[10] Mitutoyo, G Plan Apo 50x

with a microscope. The minimum waist obtained was 590 nm. This result is 30 % larger than expected due to non-optimal beam quality (size, divergence, profile) of the test laser.

To obtain two spots in the focal plane the collimated laser beam is divided on a split mirror before entering the objective lens. In this way a small angle is introduced to both partial beams leading to an offset of the focus position from the optical axis. Figure 4.11 illustrates the setup. The two spots are observed with the same microscope that was used for measuring the single

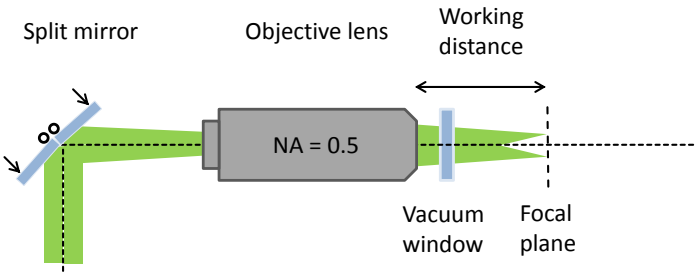

Figure 4.11.: Schematic representation of the double focus setup. A split mirror introduces a slight angle before the beam enters the focusing objective lens. Hence two foci are created off the optical axis. Objective lens is corrected for a window of 3.5 mm thickness.

focus. By adjusting the angle of the incident beams with respect to the optical axis the distance between both spots can be controlled precisely. As the beams profile is D-shaped after the split mirror the foci are elliptical. At large separation a the size of the beam profile is as small as 590 nm x 980 nm. For small separations on the order of one micrometer the light fields of both partial beams interferes and smaller spots are achievable. Figure 4.12 shows the best result in the test setup with 530 nm foci.

The foci achievable with this setup is suited for the planned experiment. The region from where the photoelectrons are emitted will be even smaller than the measured focus size as a two-photon process is used to ionize the atoms.

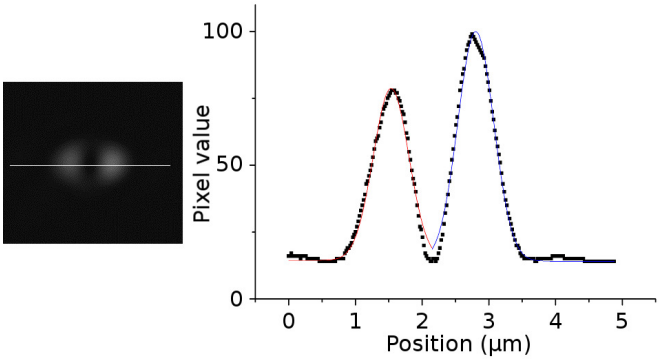

Figure 4.12.: Two adjacent foci with a size of 530 nm and a peak-to-peak separation of 1.3 µm. At this distance interference between both light field leads to smaller foci.

4.3.3. Peak Intensity & Damage Threshold

High peak intensities that occur in ultrashort laser pulses may lead to transient changes of the refractive index when passing through mediums and induce non-linear effects. These alter the temporal or spatial shape of the pulse and can even damage the optical medium.

The maximum output power of the OPA at 593.6 nm wavelength is about 100 mW. Assuming a pulse duration of 220 fs (FWHM) the peak intensity in the focus $I_0 = 8.99 \times 10^{14}\,\mathrm{W\,cm^{-2}}$ which is deep in the strong field ionization regime. The multiphoton description breaks down at the critical intensity $I_{OBI} = 1.218 \times 10^{12}\,\mathrm{W\,cm^{-2}}$ (see equation (3.1)).

Whether non-linear effects occur in the vacuum window can be estimated by calculating the phase that is accumulated in the passage through the glass using the so-called B-integral [120]:

$$B = \frac{2\pi}{\lambda} \int n_2 \times I(z) dz \tag{4.1}$$

The integration over the non-linear refractive index $n_2 = 3.25 \times 10^{-16}\,\mathrm{cm^2\,W^{-1}}$ times the peak intensity $I(z)$ is done from the inner surface of the viewport to its air side [121]. Non-linear effects such as self-focusing and filamentation are only expected for $B > 1$. In the situation under discussion the focus may be close to the window when the objective lens is pulled up. For a distance from the inner surface to the focus of 2 mm. With a total window thickness of 3.5 mm the B-integral evaluates to $B = 3.8 \times 10^{-3}$. So the laser pulses can pass the vacuum window without experiencing non-linear effects.

Furthermore damage of the window due to strong laser field will not occur as the peak intensity on the inner window surface $I_{max} = 5.76 \times 10^{8}\,\mathrm{W\,cm^{-2}}$ does not exceed the damage threshold of fused silica of $I_{dam} = 1.3 \times 10^{13}\,\mathrm{W\,cm^{-2}}$ [122].

Overall the desired peak intensity in the focus to do multiphoton ionization experiments is easily reached without running into danger of damaging the vacuum window or altering the pulse shape.

4.3.4. Beam Stabilization

In order to guarantee good reproducibility in the experiments the position jitter between the trapping beam and the ionizing beam must be minimized. Therefore both beams are actively stabilized by two systems that were setup together with Mario Neundorf in his Bachelor's work [115].

For the dipole trap a quadrant photodiode measures the beam position and feeds its signal into an analog PI loop which controls a piezo mirror (see figure 4.10). This system reduces shot-to-shot pointing fluctuations < 1 µm. Its relatively small regulation bandwidth of 20 Hz at 10 dB attenuation is sufficient as it is intended to compensate slow drifts due to temperature

changes in the laboratory.

The femtosecond laser will be located in the laboratory next door so it can be shared between different applications. Fluctuations of beam position and angle that are introduced on the long beam path are controlled with a commercially available beam stabilization system[11]. As the femtosecond laser operates in burst mode providing pulses only when a new atomic cloud is in the interaction region (every 20 s to 30 s) a collinear pilot laser is used to produce a continuous feedback signal for the stabilization system. The stabilized beam position fluctuates less than 1 µm for a beam path of more than 10 m. The commercial system features a bandwidth of 200 Hz at 10 dB attenuation.

The size of the atomic cloud is determined by the waist of the dipole trap $w = 40\,\mu\text{m}$. Hence the fluctuations are well compensated by both stabilization systems.

4.3.5. Summary

Femtosecond pulses for photoionization experiments with ultracold ^{87}Rb can be created with the optical parametric amplifier. At a wavelength close to the two-photon ionization threshold 593.63 nm it offers sufficient output power. The energy spread of the photoelectrons imposed by the laser bandwidth ($\Delta E = 12\,\text{meV}$) is small enough to maintain the fringes.

A focusing unit was developed that allows the creation of adjacent foci which are close to the diffraction limit (530 nm). An assessment of maximum peak intensity revealed that non-linear effects in the vacuum window that would alter the pulse should not occur. At the same time the peak intensity in the focus can reach deep into the strong field ionization regime.

Furthermore, a commercial beam stabilization was implemented for the femtosecond beam. It improved pointing fluctuations below 1 µm for a beam path of more than 10 m. Together with the stabilization of the trapping beam with a similar performance highly reproducibly measurements can be expected as the pointing fluctuations are much smaller than the size of the atomic cloud ($w = 40\,\mu\text{m}$).

[11] TEM Messtechnick, Alinga 4D

4.4. Detection of Charged Particles

To observe the ionization fragments detectors for electron and ions are installed in the science chamber. The position-sensitive electron detectors record the angular distribution of photoelectrons while the counting ion detector validates coincident events.

The ionization volume is located in the center of a gold plated copper cell that shields electrical stray fields. To avoid stray B-fields a diffusion barrier between the copper cell and its gold coating was omitted. The gold layer with a thickness of about 1 µm was applied electrolytically. Two electron detectors are located at both ends of the cell. The ion detector is located beneath the cell. Figure 4.13 displays a cut through the equipped science chamber. The openings in the cell left and right of its center are used to shine in the trapping beams. From the top a re-entrant viewport reaches into the science chamber in order to bring the focusing objective for the ionizing laser as close as possible to the center of the cell. The flange at the bottom of the chamber is left for connecting the pumps.

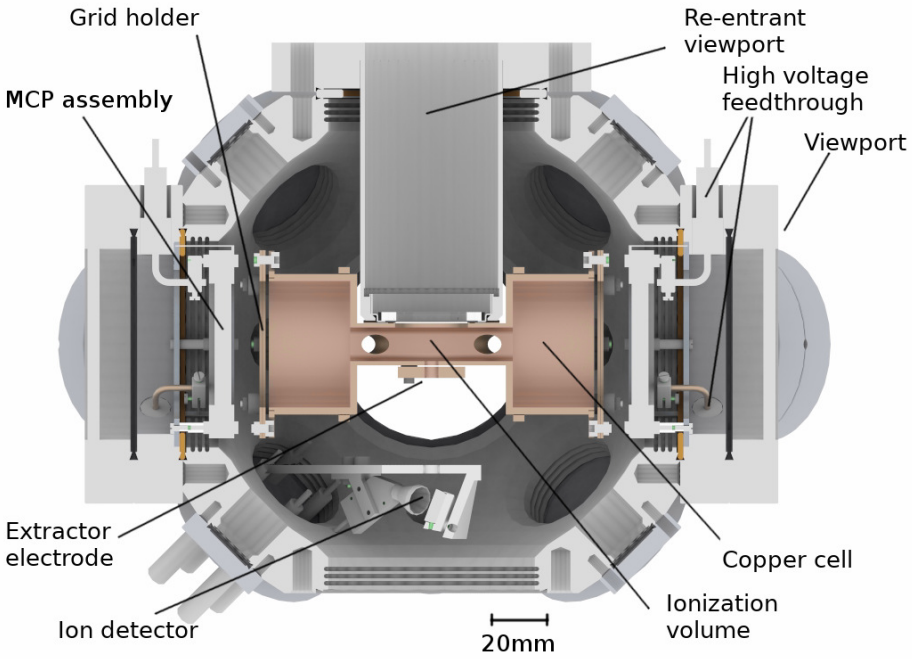

Figure 4.13.: Cut through the new science chamber. Inside sits the shielding copper cell with the extraction electrodes. The MCP detectors are located left and right in front of viewports. The focusing objective for the ionizing beam will be inserted into the re-entrant viewport.

After describing the properties of the position sensitive electron detectors a concept for a high efficiency ion detector is presented. In addition a system for compensating magnetic fields is discussed that is required because the photoelectrons are very sensitive to stray fields.

4.4.1. Electron Detection

Photoelectrons are detected with commercially available microchannel plate assemblies (MCP). Each assembly uses two plates in Chevron configuration. A grid in front of the detector is used to accelerate the electrons towards the MCP with a voltage pulse of −300 V. The additional kinetic energy ensures high detection efficiency of the MCP of $\eta_m = 0.8$ [123]. The total detection efficiency $\eta = T \times \eta_m \approx 0.7$ is determined by the MCP efficiency and the transmission probability T of the grid which is given by the open area ratio of the grid. High quality grids manufactured electrolytically offer about $T = 90\,\%$ of open area. Incident electrons are amplified by a factor of 4×10^6 while passing the channel plate [124]. The avalanche of secondary electrons exiting the plate is accelerated towards a phosphor screen where they cause a flash of light which is imaged with a high speed camera. The conversion of the electron avalanche into photons on the phosphor screen and the detection efficiency of the camera are high enough to detect all events that are initially amplified by the MCP. The detector configuration is illustrated in figure 4.14.

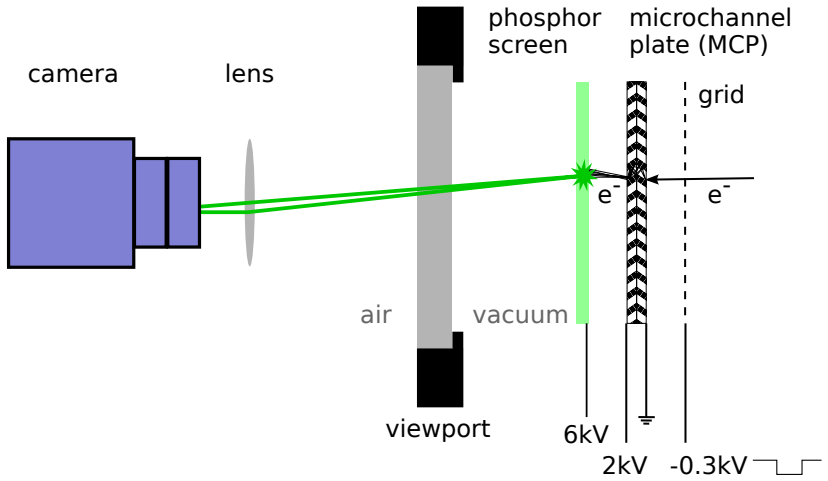

Figure 4.14.: Position-sensitive electron detector. Incoming electrons are accelerated by a voltage pulse onto the microchannel plate. The emerging electron avalanche causes a flash on the phosphor screen which is recorded by a high-speed CCD camera.

The amplification in the MCP and the subsequent acceleration onto the screen is facilitated by high voltages which are provided by a single source via the voltage divider that is illustrated in figure 4.15. The values of the two resistors are on the order of 100 MΩ to minimize power dissipation in the divider. Because these values are comparable to the MCP resistances each detector needs a custom voltage divider.

The luminescent material in the phosphor screen called P46 ($Y_3Al_5O_{12}$:Ce) has a broad photon emission spectrum that is centered around 530 nm. After electron impact the intensity decreases within typically 300 ns from 90 % to 10 %.

The events on the screen are recorded with a high speed camera[12]. It features a CMOS chip

[12] Vision Research, Phantom Miro 310; objective lens: Nikon, AF-S NIKKOR 50 mm 1:1,4G

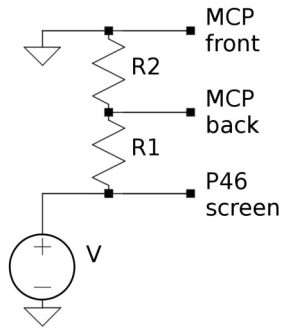

Detector	2	1
R1	139.5 MΩ	112.8 MΩ
R2	139.5 MΩ	185.4 MΩ
MCP	2x62 MΩ	2x41 MΩ
V	5.6 kV	-

Figure 4.15.: Voltage dividers for the electron detectors. R1 and R2 are adjusted to the resistance of the MCP stack.

with 1280x800 pixels and takes up to 3260 frames per seconds in full resolution. For high frame rates the resolution decreases as the camera only uses the central region of the chip. At 120 kHz frame rate the camera is able to record 128x128 pixels. Given the screen diameter of 45 mm the spatial resolution of the complete electron detection system is 350 µm. The position and brightness of recorded events are automatically extracted from the images with a LabView program. It reads all images from the camera memory, performs the blob detection and stores the recognized events in a table [125].

One of the detectors (number 2) was set up in a separate vacuum apparatus in order to optimize the voltages and to characterize the detection system[125]. The electrons for the commissioning were emitted from a heated filament. When plotting the histogram of the brightness distribution a characteristic shape emerges. An exponential decay at low intensity results from background events. The thermal electrons from the filament give rise to a Gaussian distribution. The center of this distribution depends on the kinetic energy of the incident electrons and the MCP gain voltage. The aim of the optimization is to shift the Gaussian to higher brightness in order to clearly distinguish between background events and signal.

Figure 4.16 shows the measured histogram for optimized voltages. The electrons are accelerated with 300 V onto the MCP. The gain voltage is set to 1.6 kV and the potential difference between the back of the MCP and the phosphor screen is 3.7 kV.

From the data two characteristic quantities can be extracted to characterize the detector: The pulse height resolution PHR = σ_F/c = 87 % and the peak-valley ratio PVR = v_{min}/v_{max} = 40 %. Here σ_F is the full width at half maximum, c = 2339 is the peak position on the x-axis and v denominates the number of events at the peak ($x = c$) and in the local minimum on the left. In order to distinguish between background events and signal the PHR should be small and the PVR should be large. The PHR for Chevron and Z-stack configurations is said to be typically 120 % or 80 % respectively [126].

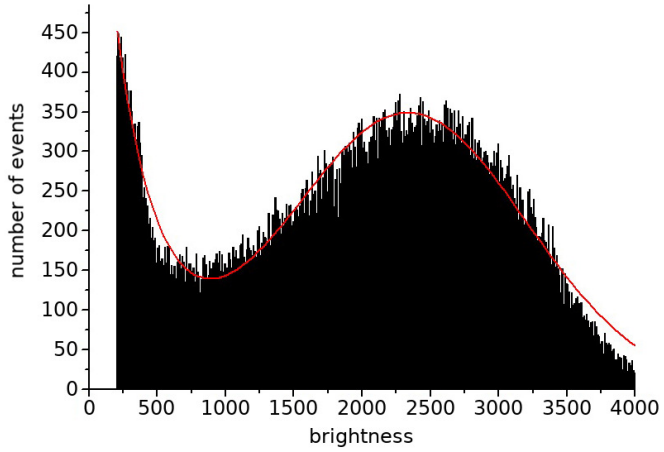

Figure 4.16.: Histogram of detected electrons at 300 eV kinetic energy. MCP Gain voltage 1.6 kV. The brightness is measured in counts on the camera summed over patches of 5x5 pixels. The electron signal is clearly separated for the exponentially decaying background.

4.4.2. Ion Detector

The ion detector must be able of detecting individual ions and distinguishing between one, two or three coincident ions. Additionally it must be as fast as the repetition rate of the ionizing laser. In this way it will be possible to re-use a prepared sample of ultracold atoms for multiple ionization experiments.

At the heart of an typical detector with single particle sensitivity is an electron amplifying device like a MCP or channel electron multiplier (CEM). If spatial resolution or a large active area is not required a CEM is chosen as it has higher gain and features a narrower pulse height distribution. In any case the incoming ions must be converted to secondary electrons before the signal can be amplified. For the direct detection with a CEM efficiencies of up to 92 % have been reported [127]. Here special care was taken to optimize the incident angle of the ions hitting the cone surface of the detector. For direct ion detection with channel plates the reported efficiencies are significantly lower around 60 % [128, 129]. A conversion dynode in front of the amplifier will increase the efficiency when the secondary electron yield is larger than one [130]. The yield strongly depends on the material, the angle of incidence and the kinetic energy of the ions [131]. The best conversion is achieved for small angles between 10° to 20° and high incident energies of more than 5 kV. The material with the highest yield is cesium iodide (CsI). Although there is no reliable absolute measurement of the energy-dependent yield for Rubidium ions a value of 20 electrons per ion can be expected. The stability of CsI layers under ambient conditions is good enough for easy fabrication and handling [132]. Alternatively stainless steel as a converter material has also proven to be suitable for unity detection efficiency with Rb ions at kinetic energies of 5 keV [133]. Figure 4.17 shows a sketch of the planned ion detector for the experiment. The dynode is inclined by about 15° against the direction of the incident ion beam.

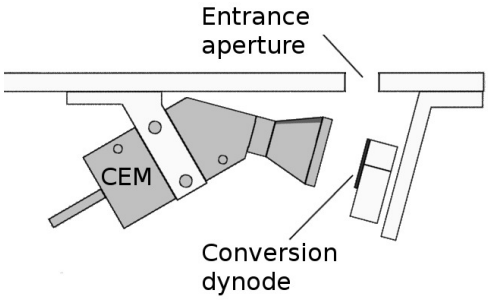

Figure 4.17.: Ion detector design. Ions entering through the aperture hit the conversion dynode. The secondary electrons created thereby are amplified in the CEM. The analog signal at its exit is analyzed in order to determine the number of ions.

The entry cone of the CEM sits vis-à-vis facing the converter.

For manufacturing custom CsI dynodes an apparatus for physical vapor deposition has been setup during the Bachelor's project of Tara Lampe [134]. She was able to realize the first CsI layers on steel and aluminum substrates. The conversion efficiency was determined for electrons since a reliable and calibrated ion gun was not available. The measured conversion efficiency of 16 secondary electrons per incident electron is compatible with the literature [135]. Exposing the layer to ambient atmosphere or heat as it will be necessary during installation and vacuum bake-out did not effect the efficiency.

4.4.3. Coincident detection of Electrons and Ions

Imaging photoelectrons and the coincident detection of the corresponding ions is technically challenging. The electrons are created inside a copper cell that shields stray electric fields emerging from the high voltage supply of the detectors. Due to their low mass the electrons move quickly towards the detectors where they pass the grid and are accelerated by a voltage pulse onto the MCP in order to optimize their detection probability. Once the electrons have hit the detector the heavy ions are extracted from the cell with an electrode at its bottom. The ions remain near their point of origin during electron detection because of their mass. After extraction the ions are accelerated in the field of the conversion dynode to achieve decent detection probability.

Figure 4.18 shows an overlay of the trajectory simulation and the mechanical design. The electron detectors ar visible in front of the large exits of the shielding copper cell. The ion detector sits beneath the cell.

The simulation assures that the electrons ($E_{kin} = 50\,\mathrm{meV}$) are well shielded against stray electric fields and that all ions arrive at the conversion dynode with the optimal velocity and angle. The simulation gives an incident angle of 17°. During the design phase mechanical modeling with SolidEdge and trajectory simulations with SIMION were alternated in an iterative

process to refine the geometry.

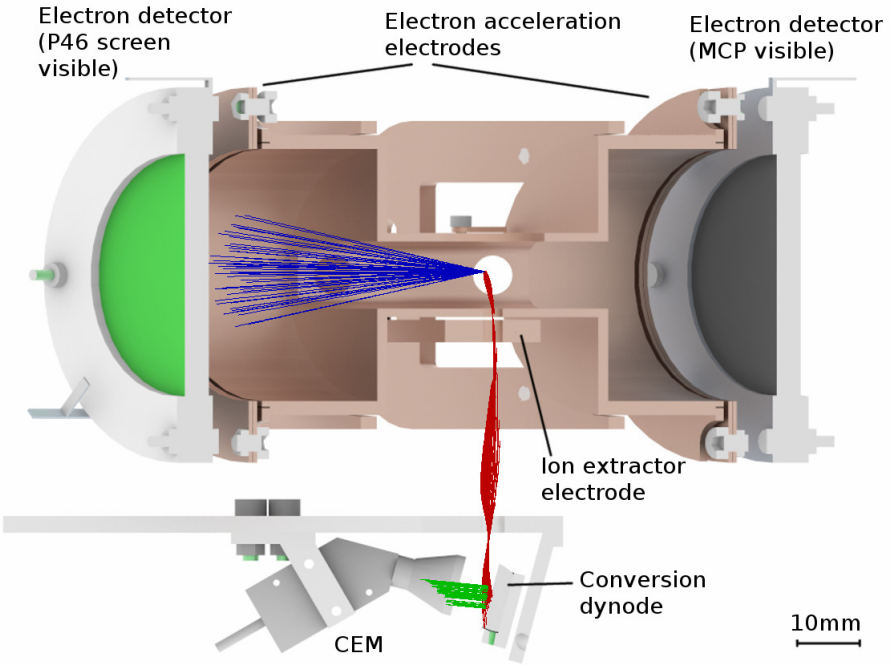

Figure 4.18.: Simulation of electron and ion trajectories. The SIMION result is superimposed on the CAD model of the shielding copper cell. Photoelectrons (blue) move straight towards the MCP detector. The ions (red) are extracted from the cell and accelerated onto the conversion dynode, where they are converted to secondary ions (green).

Figure 4.19 illustrates the sequence of voltage pulses that are used for the detection. After 0.5 µs the electrons arrive at the grid and a 0.2 µs voltage pulse of −300 V accelerates them towards the MCP. Then the extractor voltage is applied until the ions arrived at the dynode. In the simulation the ion extraction voltage was set to 100 V. Thus the ions take about 20 µs to the detector. The time-of-flight can easily be reduced by applying stronger extraction pulses because most of the time is lost during the initial acceleration inside the cell. By increasing the extraction voltage to about 300 V and simultaneously adjusting the timings the ions reach the detector before the next laser pulse arrives in the ionization volume (f_{rep} = 100 kHz).

The high voltage for the detectors is continuously present to allow for stable operation. The electron trajectories are not influenced by these electric fields.

4.4.4. Active B-Field Compensation

Electrical fields are well shielded by the copper cell but also stray magnetic fields disturb the electron trajectories via the Lorentz force. Apart from the static geomagnetic field B_{earth} = 50 µT there are AC components in the laboratory. The strongest contribution to the AC field is at the frequency of the mains and its multiples with a with a magnitude of 1 µT [136].

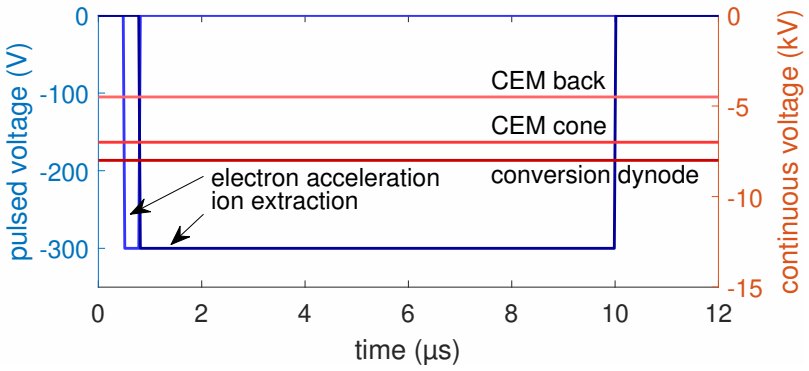

Figure 4.19.: Voltage timings. After the ionization at t=0 the electrons move field free inside the shielding cell. When passing the acceleration grids a voltage pulse is applied to increase the MCP efficiency. Then the ions are extracted from the cell. The high voltage of the detectors are not switched.

Passive B-field shielding with soft-magnetic materials (e.g. MuMetal) is very difficult as a lot of optical access is needed for the experiment. Additionally these materials are not resilient against strong fields which may occur when switching the magnetic trap. Therefore an active compensation system has been implemented that balances the magnetic field using a set of coils. Similar systems have been implemented successfully in other groups [137–139].

The maximum residual magnetic field that can be tolerated is estimated from the displacement it may add to the electrons in the detection plane. The maximum displacement $d_{dis} = 175\,\mu\text{m}$ shall be half the spatial resolution of the detector. Equating the Lorentz force $F_L = q(B \times v_e)$ to the centripetal force $F_p = m_e v_e^2 / r$ and replacing the radius of the trajectory $r = \sqrt{l^2 + (r-d)^2}$ with $l = 60\,\text{mm}$ being the distance between ionization volume and the detector yields $B_{max} = 0.07\,\mu\text{T}$. The electron velocity $v_e = \sqrt{2E_{kin}/m_e}$ was calculated for $E_{kin} = 50\,\text{meV}$ kinetic energy. In total the system shall be able to compensate for twice the geomagnetic field B_{earth} with an accuracy of B_{max}. For the AC compensation the system needs to balance transient fields with a bandwidth of 1 kHz.

Three pairs of Helmholtz coils are required to compensate the magnetic field. One pair for each spatial dimension. Their size is defined by the demanded field homogeneity and geometrical constraints in the laboratory. The cage of compensation coils was designed together with Tobias Kroker [59]. Its mechanical and electrical parameters are listed in table 4.3. The field of these coils was calculated by numerically solving Biot-Savart's law and is displayed in figure 4.20.

For an active compensation not only coils but also current sources[13] and a set of sensors and feedback loops are required. The field is measured with one magneto-resistive sensor[14] per axis. It features high accuracy (4 nT), high bandwidth (1 MHz) and good dynamic range (±200 µT). Furthermore it is robust against strong fields that may be induced while switching the magnetic

[13] HighFinesse, BCS 5A/10V
[14] Honeywell, HMC1001

axis	size (cm)	distance (cm)	turns	layers	R (Ω)	I (A)	L (mH)
x	210 x 140	83.5	10	2	1.56	5.84	3.0
y	150 x 130	74.0	10	2	1.25	4.30	2.2
z	220 x 170	100	10	2	1.74	4.01	3.5

Table 4.3.: Dimensions and electrical ratings for the cage of compensation coils. The specified current would compensate for a B-field of 100 µT.

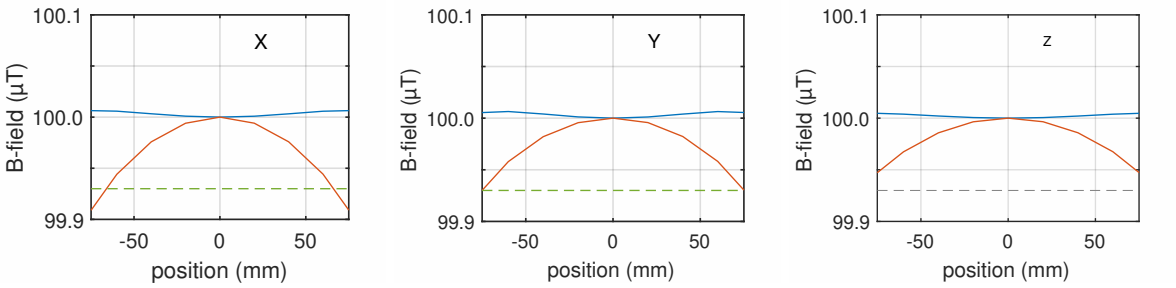

Figure 4.20.: Calculated B-field of the compensation coils on longitudinal (blue) and transveral (red) for the three axis. The dashed line indicating the limit of $B_{max} = 0.07\,\mu T$ illustrates good field homogeneity.

trap. An on-chip reset circuit increases the reproducibility of measurements. The sensor chip is mounted on a custom-built printed circuit board which can be easily installed close to the atoms as it has a small footprint. This sensor board is connected to a controller that provides an instrumentation amplifier and a serial interface to the PC. It can be used to trigger the reset function of the sensor and to adjust the signal offset. A single controller can handle up to three sensors. The amplified signal is fed into a proportional-integral controller that generates the feedback for the current sources.

In a test setup with smaller coils the compensation system showed a B-field attenuation of 30 dB at 50 Hz for a single axis [136]. The absolute residual field strength was below 35 nT. It was shown that the design of the active compensation system meets the requirements.

4.4.5. Summary

A coincident detection system for photoelectrons and ions has been developed. It consists of two position sensitive electron detectors with a spatial resolution of 350 µm and an counting ion detector.

One of the imaging electron detector has been commissioned by optimizing the operation voltages and determining the pulse height distribution. Similar measurement with the second detector are pending. Furthermore a LabVIEW program has been developed that can read out the camera and automatically analyze the position of events in a series of images.

For the ion detection a compact and highly efficient device is under active development. An

apparatus to manufacture custom CsI conversion dynodes has been setup. The dynodes are key to achieve high efficiency. The produced CsI layers have shown good secondary electron emission and are robust enough for handling.

A concept for the mechanical design has been derived from the simulation of trajectories. It shows that the ions can be extracted from the cell and guided into the detector within less than 10 µs. Their angle of incidence on the dynode (17°) is optimal. The absolute detection efficiencies of all three detectors shall be calibrated with photoelectron-photoion coincidence measurements [127].

Stray electric fields are shielded from the ionization volume by a copper cell. In addition a system for compensating stray magnetic field has been developed. The signal from magneto-resistive sensors is used to produce a feedback for the precision current sources which drive large compensation coils.

4.5. Conclusion

The novel experiment presented in this chapter allows the investigation of photoelectrons emerging from a BEC and their coherence properties. Although the new experiment is not yet operational a number of components have been built and characterized in this work.

First of all a new vacuum system was setup that will host two position-sensitive electron detectors and a device for counting ions. Several viewports providing good optical access exhibited small leaks that had to be located and fixed before it has been possible to achieve the required base pressure $p < 1 \times 10^{-11}$ mbar. Despite its porous structure the phosphor screen in the electron detectors have proven to be compatible with the extreme vacuum conditions.

For the preparation of ultracold atomic clouds a new magnetic trap was built. It achieves a field gradient of $1.75\,\mathrm{T\,m^{-1}}$ at 115 A. Together with the new fiber telescope for the trapping beam that allows for a waist $w_{dip} = 40\,\mu\mathrm{m}$ it creates a hybrid trap. An optical transport to the science chamber will be implemented by mounting the focusing lens on the air-bearing translation stage which exhibits excellent accuracy and low vibrations.

For the femtosecond laser an optical setup was developed allowing for the creation of two adjacent, diffraction-limited foci in the science chamber. The foci with a minimum size of 530 nm are almost diffraction limited and will locally ionize the BEC. The reproducibility of the experiment will be improved by active beam stabilization systems for the optical dipole trap as well as for the ionizing laser with a beam path of more than 10 m. Both systems reduce the pointing fluctuations below 1 µm.

The ionization fragments are detected using a coincidence detection scheme. It consists of two position-sensitive electron detectors with a spatial resolution of 350 µm and a counting ion detector. One of the electron detectors has been commissioned and measurements with electrons from a heated filament have shown that these events can be separated from the background based on their intensity. The estimated detection efficiency is $\eta = 0.7$. Additionally, a software program was developed for reading out the camera that images the phosphor screen of the electron detector. It extracts the position of events from the images using blob analysis. For efficient detection of ions the planned detector consists of a conversion dynode and a channel electron multiplier. A mechanical design has been derived from the simulation of ion trajectories. Furthermore an apparatus has been set up to produce custom conversion dynodes by coating a substrate with CsI. The layers exhibit a secondary electron emission yield of 16.

As electric and magnetic fields influence the trajectories of charged particles, the designed setup includes passive and active compensation against stray fields. Electric fields are shielded from the ionization volume with a copper cell. The trajectory simulation showed that the high voltages present in the detectors do not alter the electron motion. Magnetic fields have to be compensated actively with a set of Helmholtz coils. The compensation system is able to balance DC and AC fields of 100 mT with a bandwidth of 1 kHz.

APPENDIX A

Vacuum

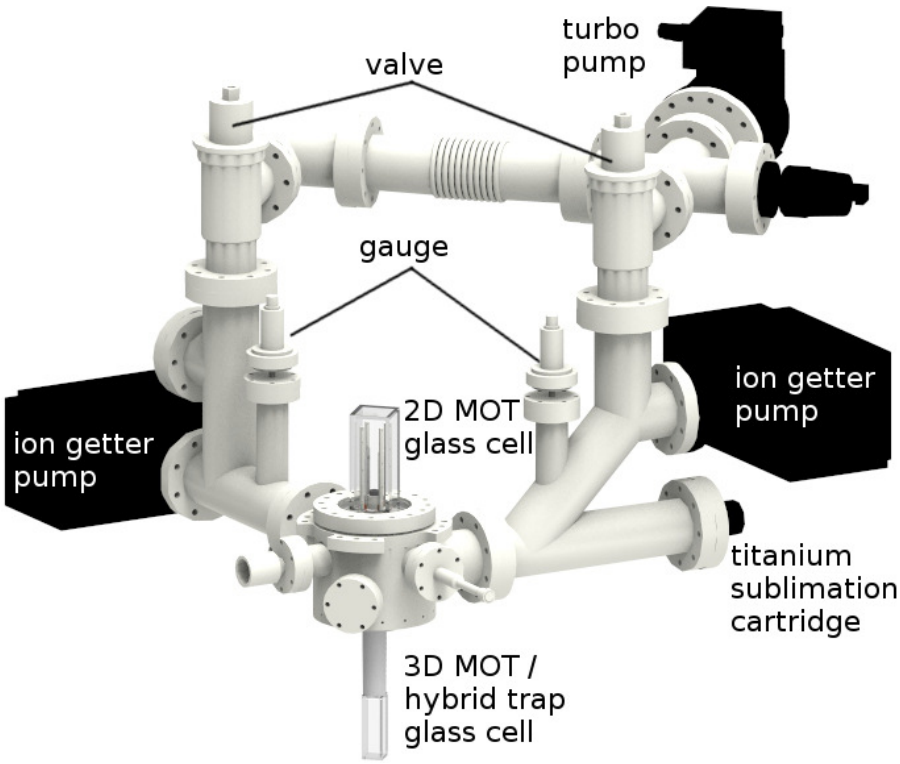

Figure A.1.: Vacuum system used for the photoionization experiments in chapter 3. The 2D and 3D MOT glass cells are connected to a differential pumping stage. The vacuum is maintained by the ion getter pumps and the TiSub. The valves to the turbo-molecular are closed as it is only used for initially evacuating the system.

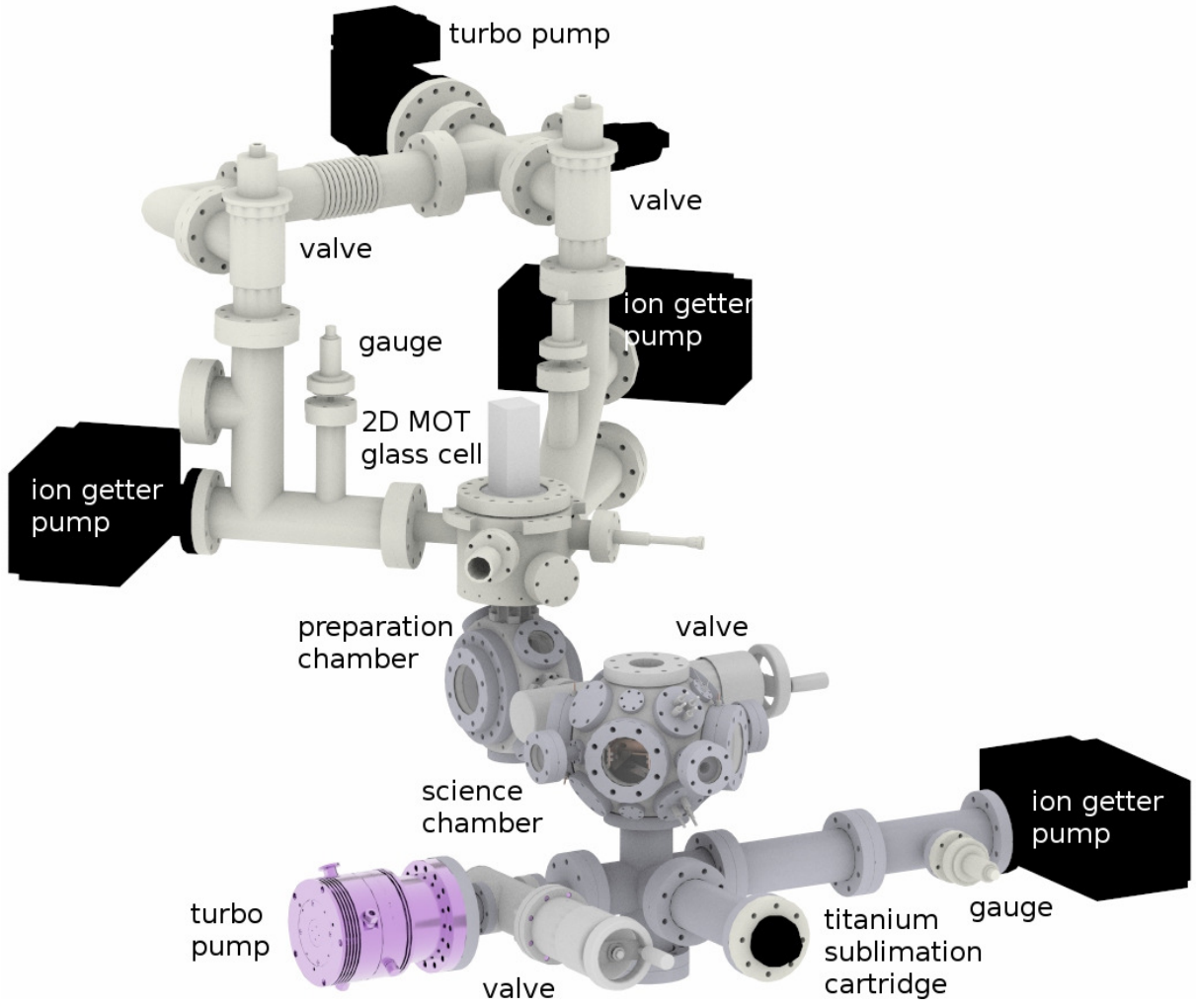

Figure A.2.: Future vacuum system including the science chamber. The lower glass cell (see figure A.1) is replaced by the new preparation chamber that provides the connection to the science chamber. The science chamber can be separated from the preparation part by an all-metal gate valve and is pumped by a dedicated ion getter pump that is supported by a TiSub cartridge.

APPENDIX B

Focusing Femtosecond Pulses

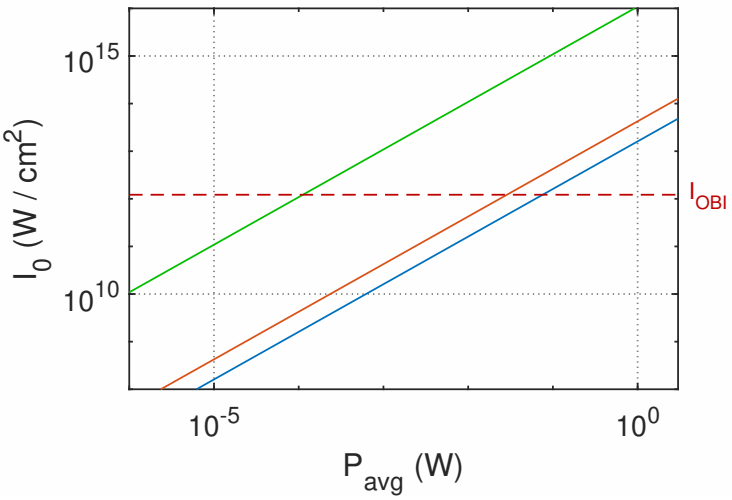

Figure B.1.: Peak intensities of femtosecond laser pulses. The calculation has been performed for various focus sizes: 0.5 µm (green) will be used in the future experiment, 8 µm (red) is the smallest focus in the current work and 13 µm (blue) has been used in the photoionization and dipole force studies. The pulse duration was assumed to be 220 fs as this is consistent with the experiment.

Acknowledgments

Successful scientific work strongly relies on the interaction and collaboration with many people who provide experience, know-how and inspiration. So I would like to take the opportunity to express appreciation to all the people I encountered in the lively scientific environment of Hamburg during my time as a PhD student. Without their support this thesis would not have been the same.

First, I want to thank my supervisors Prof. Markus Drescher and Prof. Klaus Sengstock for the opportunity to start a novel experiment combining two very fascinating fields of research, ultrafast optical physics and ultracold atoms. Their confidence and support was indispensable to finish this work. Both were always open for intensive discussions on scientific as well as technical issues and I could approach them at any time with my questions. Markus Drescher shared a lot of expertise on ultrafast lasers, detection of charged particles as well as electronics, while Klaus Sengstock provided his know-how on the quantum gas side of the experiment, including ultrahigh vacuum technology, laser cooling and imaging.

The collaborative culture in both research groups facilitated the work enormously. So, I thank all the colleagues for always giving valuable advice and for lending equipment straightforwardly.

Early on Dr. Juliette Simonet became the leading post-doc of the project. With her positive and encouraging style she guided not only my work but a whole team of students. Despite many other obligations she was available for discussions on a nearly daily basis. Thus she provided vital feedback for the daily routine.

Dr. Philipp Wessels who joined the team shortly after to set up of the pulsed laser became an appreciated colleague who shared his perspective and know-how on many occasions. He never got tired of answering anybody's questions and requests. When we started the photoionization experiments Dr. Alexander Grote and Dr. Jasper Krauser provided their valuable experiences in operating quantum gas experiments.

For inspiring discussions on the possibility of hybrid atom-ion systems and ultracold plasma I would like to thank Prof. Peter Schmelcher and Prof. Thomas Pohl as well as Dr. Johannes Schurer.

During the time of my PhD we had quite a number of highly motivated Bachelor and Master students. It was always fun working with them in the lab. Their curios questions made me reconsider my perceptions of physics one or the other time.

Besides my own experimental work I had the opportunity to assist the Light & Schools lab that was back then lead by Dortje Schirok and Dr. Thomas Garl. Communicating modern physics to pupils of various ages complemented the scientific work perfectly. Dortje's motivation to explore new ways of teaching physics and to overcome gender biases was totally contagious.

Additionally, I was able to take part in the organization of the CUI winter schools as well as a PhD workshop on ultracold atom-ion hybrid systems. It was a pleasure to do these events, especially with such dedicated colleagues as Neele Friesen and Dr. Johannes Schurer.

For the technical and administrative issues I would like to acknowledge the excellent infrastructure at the research campus Bahrenfeld in Hamburg. The local mechanical workshop lead by Stephan Fleig manufactured many custom parts for our setups. Especially, the copper cell posed several challenges that were handled exceptionally by Christian Reimer. During the setup of the new XHV vacuum system I was kindly supported by the DESY MVS vacuum team lead by Dr. Lutz Lilje.

Without the generous funding by the excellence cluster "Hamburg Centre for Ultrafast Imaging" (CUI) of the Deutsche Forschungsgemeinschaft (DFG) it would not have been possible to launch this ambitious experimental journey.

Last but not least, I have to express my gratitude to my family and all of my friends with whom I enjoyed the time off campus.

List of Figures

List of Tables

Bibliography

[1] C. Davisson and L. H. Germer: *The Scattering of Electrons by a Single Crystal of Nickel*, volume 119, Springer Nature (1927).

[2] C. Jönsson: "Elektroneninterferenzen an mehreren künstlich hergestellten Feinspalten", Zeitschrift für Physik **161**, 454–474 (1961).

[3] R. Bach, D. Pope, S.-H. Liou and H. Batelaan: "Controlled double-slit electron diffraction", New Journal of Physics **15**, 033018 (2013).

[4] Bose: "Plancks Gesetz und Lichtquantenhypothese", Zeitschrift für Physik **26**, 178–181 (1924).

[5] A. Einstein: *Quantentheorie des einatomigen idealen Gases*, Akademie der Wissenshaften, in Kommission bei W. de Gruyter (2006).

[6] M. H. Anderson, J. R. Ensher, M. R. Matthews, C. E. Wieman and E. A. Cornell: "Observation of Bose-Einstein Condensation in a Dilute Atomic Vapor", Science **269**, 198–201 (1995).

[7] C. C. Bradley, C. A. Sackett, J. J. Tollett and R. G. Hulet: "Evidence of Bose-Einstein Condensation in an Atomic Gas with Attractive Interactions", Physical Review Letters **75**, 1687–1690 (1995).

[8] K. B. Davis, M. O. Mewes, M. R. Andrews, N. J. van Druten, D. S. Durfee, D. M. Kurn and W. Ketterle: "Bose-Einstein Condensation in a Gas of Sodium Atoms", Physical Review Letters **75**, 3969–3973 (1995).

[9] T. Hänsch and A. Schawlow: "Cooling of gases by laser radiation", Optics Communications **13**, 68–69 (1975).

[10] D. Wineland and H. Dehmelt: "Proposed $10^{14}\Delta\nu < \nu$ laser fluorescence spectroscopy on Tl^+ mono-ion oscillator", in "Bulletin of the American Physical Society", volume 20, pages 637–637 (1975).

[11] A. L. Migdall, J. V. Prodan, W. D. Phillips, T. H. Bergeman and H. J. Metcalf: "First Observation of Magnetically Trapped Neutral Atoms", Physical Review Letters **54**, 2596–2599 (1985).

[12] S. Chu, L. Hollberg, J. E. Bjorkholm, A. Cable and A. Ashkin: "Three-dimensional viscous confinement and cooling of atoms by resonance radiation pressure", Physical Review Letters **55**, 48–51 (1985).

[13] J. Dalibard and C. Cohen-Tannoudji: "Laser cooling below the Doppler limit by polarization gradients: simple theoretical models", Journal of the Optical Society of America B **6**, 2023 (1989).

[14] D. E. Pritchard: "Cooling Neutral Atoms in a Magnetic Trap for Precision Spectroscopy", Physical Review Letters **51**, 1336–1339 (1983).

[15] H. F. Hess: "Evaporative cooling of magnetically trapped and compressed spin-polarized hydrogen", Physical Review B **34**, 3476–3479 (1986).

[16] W. Petrich, M. H. Anderson, J. R. Ensher and E. A. Cornell: "Stable, Tightly Confining Magnetic Trap for Evaporative Cooling of Neutral Atoms", Physical Review Letters **74**, 3352–3355 (1995).

[17] O. J. Luiten, M. W. Reynolds and J. T. M. Walraven: "Kinetic theory of the evaporative cooling of a trapped gas", Physical Review A **53**, 381–389 (1996).

[18] M. R. Andrews, C. G. Townsend, H.-J. Miesner, D. S. Durfee, D. M. Kurn and W. Ketterle: "Observation of Interference Between Two Bose Condensates", Science **275**, 637–641 (1997).

[19] M. R. Andrews, D. M. Kurn, H.-J. Miesner, D. S. Durfee, C. G. Townsend, S. Inouye and W. Ketterle: "Propagation of Sound in a Bose-Einstein Condensate", Physical Review Letters **79**, 553–556 (1997).

[20] D. M. Stamper-Kurn, H.-J. Miesner, S. Inouye, M. R. Andrews and W. Ketterle: "Collisionless and Hydrodynamic Excitations of a Bose-Einstein Condensate", Physical Review Letters **81**, 500–503 (1998).

[21] I. Carusotto, S. X. Hu, L. A. Collins and A. Smerzi: "Bogoliubov-Čerenkov Radiation in a Bose-Einstein Condensate Flowing against an Obstacle", Physical Review Letters **97** (2006).

[22] R. Meppelink, S. B. Koller and P. van der Straten: "Sound propagation in a Bose-Einstein condensate at finite temperatures", Physical Review A **80** (2009).

[23] W. Ketterle, D. S. Durfee and D. M. Stamper-Kurn: "Making, probing and understanding Bose-Einstein condensates", Proceedings of the 1998 Enrico Fermi summer school on Bose-Einstein condensation in Varenna, Italy (1999).

[24] I. Bloch, J. Dalibard and W. Zwerger: "Many-body physics with ultracold gases", Reviews of Modern Physics **80**, 885–964 (2008).

[25] C. Raman, M. Köhl, R. Onofrio, D. S. Durfee, C. E. Kuklewicz, Z. Hadzibabic and W. Ketterle: "Evidence for a Critical Velocity in a Bose-Einstein Condensed Gas", Physical Review Letters **83**, 2502–2505 (1999).

[26] R. Onofrio, C. Raman, J. M. Vogels, J. R. Abo-Shaeer, A. P. Chikkatur and W. Ketterle: "Observation of Superfluid Flow in a Bose-Einstein Condensed Gas", Physical Review Letters **85**, 2228–2231 (2000).

[27] D. E. Miller, J. K. Chin, C. A. Stan, Y. Liu, W. Setiawan, C. Sanner and W. Ketterle: "Critical Velocity for Superfluid Flow across the BEC-BCS Crossover", Physical Review Letters **99** (2007).

[28] R. Desbuquois, L. Chomaz, T. Yefsah, J. Léonard, J. Beugnon, C. Weitenberg and J. Dalibard: "Superfluid behaviour of a two-dimensional Bose gas", Nature Physics **8**, 645–648 (2012).

[29] W. Weimer, K. Morgener, V. P. Singh, J. Siegl, K. Hueck, N. Luick, L. Mathey and H. Moritz: "Critical Velocity in the BEC-BCS Crossover", Physical Review Letters **114** (2015).

[30] V. P. Singh, W. Weimer, K. Morgener, J. Siegl, K. Hueck, N. Luick, H. Moritz and L. Mathey: "Probing superfluidity of Bose-Einstein condensates via laser stirring", Physical Review A **93** (2016).

[31] A. P. Chikkatur, A. Görlitz, D. M. Stamper-Kurn, S. Inouye, S. Gupta and W. Ketterle: "Suppression and Enhancement of Impurity Scattering in a Bose-Einstein Condensate", Physical Review Letters **85**, 483–486 (2000).

[32] R. Heidemann, U. Raitzsch, V. Bendkowsky, B. Butscher, R. Löw and T. Pfau: "Rydberg Excitation of Bose-Einstein Condensates", Physical Review Letters **100** (2008).

[33] M. Viteau, M. Bason, J. Radogostowicz, N. Malossi, O. Morsch, D. Ciampini and E. Arimondo: "Rydberg excitation of a Bose–Einstein condensate", Laser Physics **23**, 015502 (2012).

[34] V. Bendkowsky, B. Butscher, J. Nipper, J. P. Shaffer, R. Löw and T. Pfau: "Observation of ultralong-range Rydberg molecules", Nature **458**, 1005–1008 (2009).

[35] J. Wang, J. N. Byrd, I. Simbotin and R. Côté: "Tuning Ultracold Chemical Reactions via Rydberg-Dressed Interactions", Physical Review Letters **113** (2014).

[36] R. Mukherjee, C. Ates, W. Li and S. Wüster: "Phase-Imprinting of Bose-Einstein Condensates with Rydberg Impurities", Physical Review Letters **115** (2015).

[37] R. Côté: "Ultracold Hybrid Atom–Ion Systems", in "Advances In Atomic, Molecular, and Optical Physics", pages 67–126, Elsevier BV (2016).

[38] J. M. Schurer, P. Schmelcher and A. Negretti: "Ground-state properties of ultracold trapped bosons with an immersed ionic impurity", Physical Review A **90** (2014).

[39] F. H. Hall, P. Eberle, G. Hegi, M. Raoult, M. Aymar, O. Dulieu and S. Willitsch: "Ion-neutral chemistry at ultralow energies: dynamics of reactive collisions between laser-cooled Ca^+ ions and Rb atoms in an ion-atom hybrid trap", Molecular Physics **111**, 2020–2032 (2013).

[40] L. Ratschbacher, C. Zipkes, C. Sias and M. Köhl: "Controlling chemical reactions of a single particle", Nature Physics **8**, 649–652 (2012).

[41] S. Schmid, A. Härter and J. H. Denschlag: "Dynamics of a Cold Trapped Ion in a Bose-Einstein Condensate", Physical Review Letters **105** (2010).

[42] M. Krych, W. Skomorowski, F. Pawłowski, R. Moszynski and Z. Idziaszek: "Sympathetic cooling of the Ba^+ ion by collisions with ultracold Rb atoms: Theoretical prospects", Physical Review A **83** (2011).

[43] C. Zipkes, L. Ratschbacher, S. Palzer, C. Sias and M. Köhl: "Hybrid quantum systems of atoms and ions", Journal of Physics: Conference Series **264**, 012019 (2011).

[44] A. Härter and J. H. Denschlag: "Cold atom–ion experiments in hybrid traps", Contemporary Physics **55**, 33–45 (2014).

[45] T. Huber, A. Lambrecht, J. Schmidt, L. Karpa and T. Schaetz: "A far-off-resonance optical trap for a Ba^+ ion", Nature Communications **5**, 5587 (2014).

[46] T. C. Killian, S. Kulin, S. D. Bergeson, L. A. Orozco, C. Orzel and S. L. Rolston: "Creation of an Ultracold Neutral Plasma", Physical Review Letters **83**, 4776–4779 (1999).

[47] T. Killian, T. Pattard, T. Pohl and J. Rost: "Ultracold neutral plasmas", Physics Reports **449**, 77–130 (2007).

[48] T. P. Dinneen, C. D. Wallace, K.-Y. N. Tan and P. L. Gould: "Use of trapped atoms to measure absolute photoionization cross sections", Optics Letters **17**, 1706 (1992).

[49] D. Ciampini, M. Anderlini, J. H. Müller, F. Fuso, O. Morsch, J. W. Thomsen and E. Arimondo: "Photoionization of ultracold and Bose-Einstein-condensed Rb atoms", Physical Review A **66**, 043409 (2002).

[50] T. Takekoshi, G. M. Brooke, B. M. Patterson and R. J. Knize: "Absolute Rb one-color two-photon ionization cross-section measurement near a quantum interference", Phys. Rev. A **69**, 053411 (2004).

[51] M. Protopapas, C. H. Keitel and P. L. Knight: "Atomic physics with super-high intensity lasers", Reports on Progress in Physics **60**, 389–486 (1997).

[52] M. Wollenhaupt, A. Assion, D. Liese, C. Sarpe-Tudoran, T. Baumert, S. Zamith, M. A. Bouchene, B. Girard, A. Flettner, U. Weichmann and G. Gerber: "Interferences of Ultrashort Free Electron Wave Packets", Physical Review Letters **89** (2002).

[53] B. Misra and E. C. G. Sudarshan: "The Zeno's paradox in quantum theory", Journal of Mathematical Physics **18**, 756–763 (1977).

[54] W. M. Itano, D. J. Heinzen, J. J. Bollinger and D. J. Wineland: "Quantum Zeno effect", Physical Review A **41**, 2295–2300 (1990).

[55] G. Barontini, R. Labouvie, F. Stubenrauch, A. Vogler, V. Guarrera and H. Ott: "Controlling the Dynamics of an Open Many-Body Quantum System with Localized Dissipation", Physical Review Letters **110** (2013).

[56] R. Labouvie, B. Santra, S. Heun and H. Ott: "Bistability in a Driven-Dissipative Superfluid", Physical Review Letters **116** (2016).

[57] A. Grote: "Aufbau eines Ultrahochvakuumsystems und einer 2D-3D-Fallenkombination eines Quantengasmessplatzes für Forschung und Lehre (in German)", Master's thesis (2011).

[58] E. M. Fricke: "Aufbau eines Bose-Fermi-Quantengassystems für Forschung und Lehre (in German)", Master's thesis (2010).

[59] T. Kroker: "Photoionisation ultrakalter ^{87}Rb-Atome in starken Laserfeldern", Master's thesis (2016).

[60] M. Pfau: "Aufbau einer Dipolfalle zur Untersuchung von Solitonen in einem Rubidium Bose-Einstein Kondenstat (in German)", Diplomarbeit (2013).

[61] H. Blazy: "Optimizing a Quantum Gas Machine for Ionization of a Bose-Einstein Condensate with ultrashort Laser Pulses (in German)", Master's thesis (2014).

[62] H. Krüger: "Aufbau und Charakterisierung einer Hybridfalle für ultrakalte Quantengase (in German)", Master's thesis (2015).

[63] C. J. Foot: *Atomic Physics*, chapter 9 – Laser Cooling and Trapping, pages 178 – 217, Oxford University Press (2005).

[64] D. A. Steck: "Rubidium 87 D-Line Data", (rev 2.1.5), available online, accessed [13 January 2015] (2015).

[65] C. J. Foot: *Atomic Physics*, chapter 7 – Interaction of Atoms with Radiation, pages 123 – 150, Oxford University Press (2005).

[66] K. Dieckmann, R. J. C. Spreeuw, M. Weidemüller and J. T. M. Walraven: "Two-dimensional magneto-optical trap as a source of slow atoms", Physical Review A **58**, 3891–3895 (1998).

[67] H. J. Metcalf and P. van der Straten: *Laser Cooling and Trapping*, Springer New York (1999).

[68] E. Majorana: "Atomi orientati in campo magnetico variabile", Il Nuovo Cimento **9**, 43–50 (1932).

[69] Y.-J. Lin, A. R. Perry, R. L. Compton, I. B. Spielman and J. V. Porto: "Rapid production of ^{87}Rb Bose-Einstein condensates in a combined magnetic and optical potential", Physical Review A **79** (2009).

[70] P. Christoph: "Aufbau einer Magnetfalle und ihrer Treibersteuerung zur Erzeugung ultrakalter ^{87}Rb / ^{40}K-Quantengasmischungen (in German)", Bachelor's thesis (2010).

[71] J. Dalibard and C. Cohen-Tannoudji: "Dressed-atom approach to atomic motion in laser light: the dipole force revisited", Journal of the Optical Society of America B **2**, 1707–1720 (1985).

[72] R. Grimm, M. Weidemüller and Y. B. Ovchinnikov: "Optical Dipole Traps for Neutral Atoms", in "Advances In Atomic, Molecular, and Optical Physics", pages 95–170, Elsevier BV (2000).

[73] M. D. Barrett, J. A. Sauer and M. S. Chapman: "All-Optical Formation of an Atomic Bose-Einstein Condensate", Physical Review Letters **87** (2001).

[74] A. Barg: "Aufbau einer Vakuum-Apparatur für Quantengasexperimente (in German)", Bachelor's thesis (2011).

[75] A. Kriszat: "Control system for a quantum gas experiment (in German)", Bachelor's thesis (2011).

[76] PCO AG: "Datasheet pco.pixelfly usb", available online, accessed: [2015, January 13].

[77] G. Reinaudi, T. Lahaye, Z. Wang and D. Guéry-Odelin: "Strong saturation absorption imaging of dense clouds of ultracold atoms", Optics Letters **32**, 3143 (2007).

[78] W. J. Kwon, J. yoon Choi and Y. il Shin: "Calibration of saturation absorption imaging of ultracold atom clouds", Journal of the Korean Physical Society **61**, 1970–1974 (2012).

[79] C. Rullière (editor): *Femtosecond Laser Pulses*, Springer-Verlag GmbH (2004).

[80] Light Conversion: "Pharos Service Report", (2015).

[81] D. Strickland and G. Mourou: "Compression of amplified chirped optical pulses", Optics Communications **56**, 219–221 (1985).

[82] A. Brodeur and S. L. Chin: "Ultrafast white-light continuum generation and self-focusing in transparent condensed media", Journal of the Optical Society of America B **16**, 637 (1999).

[83] D. Göries, B. Dicke, P. Roedig, N. Stübe, J. Meyer, A. Galler, W. Gawelda, A. Britz, P. Geßler, H. S. Namin, A. Beckmann, M. Schlie, M. Warmer, M. Naumova, C. Bressler, M. Rübhausen, E. Weckert and A. Meents: "Time-resolved pump and probe x-ray absorption fine structure spectroscopy at beamline P11 at PETRA III", Review of Scientific Instruments **87**, 053116 (2016).

[84] P. Wessels, J. Ewald, M. Wieland, T. Nisius, A. Vogel, J. Viefhaus, G. Meier, T. Wilhein and M. Drescher: "Time-resolved imaging of domain pattern destruction and recovery via nonequilibrium magnetization states", Physical Review B **90** (2014).

[85] P. Wessels, A. Vogel, J.-N. Tödt, M. Wieland, G. Meier and M. Drescher: "Direct observation of isolated Damon-Eshbach and backward volume spin-wave packets in ferromagnetic microstripes", Scientific Reports **6**, 22117 (2016).

[86] A. Kramida, Yu. Ralchenko, J. Reader and and NIST ASD Team: "NIST Atomic Spectra Database (ver. 5.3)", available online. accessed: 2016, September 8. National Institute of Standards and Technology, Gaithersburg, MD. (2015).

[87] M. Viteau, J. Radogostowicz, A. Chotia, M. G. Bason, N. Malossi, F. Fuso, D. Ciampini, O. Morsch, I. I. Ryabtsev and E. Arimondo: "Ion detection in the photoionization of a Rb Bose–Einstein condensate", Journal of Physics B: Atomic, Molecular and Optical Physics **43**, 155301 (2010).

[88] J. B. Balewski, A. T. Krupp, A. Gaj, D. Peter, H. P. Büchler, R. Löw, S. Hofferberth and T. Pfau: "Coupling a single electron to a Bose–Einstein condensate", Nature **502**, 664–667 (2013).

[89] N. B. Delone and V. P. Krainov: "Tunneling and barrier-suppression ionization of atoms and ions in a laser radiation field", Physics-Uspekhi **41**, 469 (1998).

[90] M. Schuricke, G. Zhu, J. Steinmann, K. Simeonidis, I. Ivanov, A. Kheifets, A. N. Grum-Grzhimailo, K. Bartschat, A. Dorn and J. Ullrich: "Strong-field ionization of lithium", Phys. Rev. A **83**, 023413 (2011).

[91] C. J. G. J. Uiterwaal, D. Xenakis, D. Charalambidis, P. Maragakis, H. Schröder and P. Lambropoulos: "Generalized multiphoton-ionization cross sections of the rare gases for 500-fs, 248.6-nm pulses", Phys. Rev. A **57**, 392–400 (1998).

[92] A. Scrinzi, M. Geissler and T. Brabec: "Ionization Above the Coulomb Barrier", Physical Review Letters **83**, 706–709 (1999).

[93] M. V. Ammosov, N. B. Delone and V. P. Krainov: "Tunnel ionization of complex atoms and of atomic ions in an alternating electromagnetic field", JETP **64**, 1191–1194 (1986).

[94] X. M. Tong and C. D. Lin: "Empirical formula for static field ionization rates of atoms and molecules by lasers in the barrier-suppression regime", J. Phys. B: At. Mol. Opt. Phys. **38**, 2593–2600 (2005).

[95] M. Z. Milošević and N. S. Simonović: "Calculations of rates for strong-field ionization of alkali-metal atoms in the quasistatic regime", Physical Review A **91** (2015).

[96] A. Grote: "Ultracold ^{87}Rb: from quantum metrology to two-photon ionization", phdthesis (2016).

[97] M. Wollenhaupt: *Springer Handbook of Lasers and Optics*, chapter 12 - Short and Ultrashort Laserpulses, pages 1047–1094, Springer Nature (2012).

[98] D. N. Yanyshev, V. I. Balykin, Y. V. Vladimirova and V. N. Zadkov: "Dynamics of atoms in a femtosecond optical dipole trap", Physical Review A **87** (2013).

[99] A. Goepfert, I. Bloch, D. Haubrich, F. Lison, R. Schütze, R. Wynands and D. Meschede: "Stimulated focusing and deflection of an atomic beam using picosecond laser pulses", Physical Review A **56**, R3354–R3357 (1997).

[100] M. Shiddiq, E. M. Ahmed, M. D. Havey and C. I. Sukenik: "Investigation of loading of pulsed and continuous-wave optical dipole force traps", Physical Review A **77** (2008).

[101] M. S. Safronova and U. I. Safronova: "Critically evaluated theoretical energies, lifetimes, hyperfine constants, and multipole polarizabilities in ^{87}Rb", Physical Review A **83** (2011).

[102] D. B. Branden, T. Juhasz, T. Mahlokozera, C. Vesa, R. O. Wilson, M. Zheng, A. Kortyna and D. A. Tate: "Radiative lifetime measurements of rubidium Rydberg states", Journal of Physics B: Atomic, Molecular and Optical Physics **43**, 015002 (2009).

[103] C. Krenn, W. Scherf, O. Khait, M. Musso and L. Windholz: "Stark effect investigations of resonance lines of neutral potassium, rubidium, europium and gallium", Zeitschrift für Physik D Atoms, Molecules and Clusters **41**, 229–233 (1997).

[104] R. Côté and A. Dalgarno: "Ultracold atom-ion collisions", Physical Review A **62**, 012709 (2000).

[105] F. Grusdt, Y. E. Shchadilova, A. N. Rubtsov and E. Demler: "Renormalization group approach to the Fröhlich polaron model: application to impurity-BEC problem", Scientific Reports **5**, 12124 (2015).

[106] T. C. Killian, M. J. Lim, S. Kulin, R. Dumke, S. D. Bergeson and S. L. Rolston: "Formation of Rydberg Atoms in an Expanding Ultracold Neutral Plasma", Physical Review Letters **86**, 3759–3762 (2001).

[107] H. Krüger: "Aufbau und Charakterisierung einer Hybridfalle für ultrakalte Quantengase", (2015), master Kolliquium.

[108] T. L. Gustavson, A. P. Chikkatur, A. E. Leanhardt, A. Görlitz, S. Gupta, D. E. Pritchard and W. Ketterle: "Transport of Bose-Einstein Condensates with Optical Tweezers", Physical Review Letters **88**, 020401 (2001).

[109] Pfeiffer Vacuum GmbH: *Vacuum Technoloy*, volume 2 - Know How Book, Pfeiffer Vacuum GmbH (2013).

[110] R. Calder and G. Lewin: "Reduction of stainless-steel outgassing in ultra-high vacuum", British Journal of Applied Physics **18**, 1459–1472 (1967).

[111] J.-P. Bacher, C. Benvenuti, P. Chiggiato, M.-P. Reinert, S. Sgobba and A.-M. Brass: "Thermal desorption study of selected austenitic stainless steels", Journal of Vacuum Science & Technology A: Vacuum, Surfaces, and Films **21**, 167–174 (2003).

[112] R. Eichberger: "Aufbau einer wassergekühlten Magnetfalle zur Erzeugung ultrakalter ^{40}K / ^{87}Rb Quantengasmischungen und ihres elektronischen Interlocksystems (in German)", Bachelor's thesis (2010).

[113] M. Greiner, I. Bloch, T. W. Hänsch and T. Esslinger: "Magnetic transport of trapped cold atoms over a large distance", Physical Review A **63**, 031401 (2001).

[114] J. Léonard, M. Lee, A. Morales, T. M. Karg, T. Esslinger and T. Donner: "Optical transport and manipulation of an ultracold atomic cloud using focus-tunable lenses", New Journal of Physics **16**, 093028 (2014).

[115] M. Neundorf: "Setup and characterization of a 2D beam pointing stabilization", Bachelor's thesis (2016).

[116] A. P. Chikkatur: "Colliding and Moving Bose-Einstein Condensates: Studies of superfluidity and optical tweezers for condensate transport", phdthesis (2002).

[117] M. Schröder: "Design and setup of an optical tweezer for ultracold atoms (in German)", Bachelor's thesis (2015).

[118] A. Couvert, T. Kawalec, G. Reinaudi and D. Guéry-Odelin: "Optimal transport of ultracold atoms in the non-adiabatic regime", EPL (Europhysics Letters) **83**, 13001 (2008).

[119] J. Frohn: "Optical setup for generation of a sub-micron doublefocus in German)", Bachelor's thesis (2014).

[120] R. Paschotta: *Encyclopedia of Laser Physics and Technology*, Wiley VCH Verlag GmbH (2008).

[121] A. J. Taylor, T. S. Clement and G. Rodriguez: "Determination of n_2 by direct measurement of the optical phase", Opt. Lett. **21**, 1812–1814 (1996).

[122] B. Chimier, O. Utéza, N. Sanner, M. Sentis, T. Itina, P. Lassonde, F. Légaré, F. Vidal and J. C. Kieffer: "Damage and ablation thresholds of fused-silica in femtosecond regime", Physical Review B **84** (2011).

[123] G. Fraser: "The electron detection efficiency of microchannel plates", Nuclear Instruments and Methods in Physics Research **206**, 445–449 (1983).

[124] GIDS GmbH German Imaging Detector Systems: *Datasheet - Detector: MCP-45-2-40-P46-N* (2014).

[125] S. Pehmöller: "Setup and test of an imaging electron detector for ionization experiments in a laser double-focus (in German)", Bachelor's thesis (2015).

[126] Hammamatsu Photonics K.K.: "Technical Information – MCP Assembly", available online, accessed: [2017, January 03] (2006).

[127] F. Henkel, M. Krug, J. Hofmann, W. Rosenfeld, M. Weber and H. Weinfurter: "Highly Efficient State-Selective Submicrosecond Photoionization Detection of Single Atoms", Physical Review Letters **105** (2010).

[128] J. Oberheide, P. Wilhelms and M. Zimmer: "New results on the absolute ion detection efficiencies of a microchannel plate", Measurement Science and Technology **8**, 351 (1997).

[129] B. Brehm, J. Grosser, T. Ruscheinski and M. Zimmer: "Absolute detection efficiencies of a microchannel plate detector for ions", Measurement Science and Technology **6**, 953–958 (1995).

[130] K. Rinn, A. Müller, H. Eichenauer and E. Salzborn: "Development of single-particle detectors for keV ions", Review of Scientific Instruments **53**, 829–837 (1982).

[131] G. Fraser: "The ion detection efficiency of microchannel plates (MCPs)", International Journal of Mass Spectrometry **215**, 13–30 (2002).

[132] R. L. Verma: "Potential and limitations of caesium iodide as a dynode material for use in electron multipliers", Journal of Physics D: Applied Physics **11**, 63 (1978).

[133] T. Koizumi and Y. Chihara: "Absolute detection efficiencies of an ion-counting system with a channel-electron multiplier", Journal of Physics: Conference Series **163**, 012114 (2009).

[134] T. Lampe: "Fabrication and characterization of high efficiency ion to electron conversion dynodes (in German)", Bachelor's thesis (2016).

[135] R. L. Verma: "Secondary electron emission of caesium iodide", Journal of Physics D: Applied Physics **6**, 2137 (1973).

[136] T. Anlauf: "Active magnetic field compensation for photoionisation studies on an ultracold quantum gas (in German)", Bachelor's thesis (2016).

[137] M. Skakala, V. Zrubec and J. Manka: "Active compensation for ambient magnetic noise in the unshielded environment", Meas. Sci. Technol. 4 **4**, 468–472 (1993).

[138] C. J. Dedman, R. G. Dall, L. J. Byron and A. G. Truscott: "Active cancellation of stray magnetic fields in a Bose-Einstein condensation experiment", Review of Scientific Instruments **78**, 024703 (2007).

[139] C. Hamner, C. Qu, Y. Zhang, J. Chang, M. Gong, C. Zhang and P. Engels: "Dicke-type phase transition in a spin-orbit-coupled Bose–Einstein condensate", Nature Communications **5** (2014).

Bernhard Ruff

Local ionization of quantum gases allows addressing fundamental questions in quantum physics. In the intense field of ultrashort light pulses an ultracold atomic cloud can be ionized granting access to the physics of open quantum systems and hybrid atom-ion systems. Analyzing the ionization fragments allows investigating the transfer of coherence from a macroscopic quantum mechanical state to its microscopic constituents.

This book covers experiments on photoioniation, transient optical potentials as well as the formation of ultracold plasmas. Furthermore, a new experimental setup has been designed paving the way to novel and detailed studies of the photoionization process in Bose-Einstein condensates.